A Random Walk through Star and Planet Formation

by

Holly Lynn Maness

A dissertation submitted in partial satisfaction of the
requirements for the degree of
Doctor of Philosophy

in

Astrophysics

in the

Graduate Division
of the
University of California, Berkeley

Committee in charge:
Geoffrey Marcy, Chair
Paul Kalas
Eugene Chiang
Richard Saykally

Fall 2010

A Random Walk through Star and Planet Formation

Abstract

A Random Walk through Star and Planet Formation

by

Holly Lynn Maness
Doctor of Philosophy in Astrophysics

University of California, Berkeley

Geoffrey Marcy, Chair

This thesis explores selected questions in several active areas of research in star and planet formation. Chapter 2 constrains the star formation history and initial mass function of the old stellar population in the Galactic Center nuclear star cluster. Preliminary results suggest an initial mass function for this region that differs significantly from the standard mass function observed in other parts of the Galaxy. Chapter 3 derives stellar and planetary properties for an extraordinary planetary system that surrounds an unusually low-mass star and includes the closest, smallest, and least massive planet known to date. The data presented in this chapter were valuable in enabling a follow-up transit detection of this planet that placed strong constraints on its internal structure and composition. Chapters 4 and 5 analyze observations of extrasolar debris disks in an effort to infer global characteristics of the underlying planetary systems, including the location and properties of planetesimals and planets. Specifically, Chapter 4 presents multi-wavelength imaging observations of a debris disk that potentially point to the existence of an unseen exoplanet. In contrast, Chapter 5 considers substructure in a different debris disk that is unlikely to be gravitational in origin. The results suggest that debris disk interactions with the interstellar medium may create asymmetries that mimic the presence of an exoplanet at short, scattered-light wavelengths.

I dedicate this dissertation to Alexander Truesdell Shreve, my confidant and best friend throughout these transformative years.

Contents

List of Figures

List of Tables

Acknowledgments

The last six years have comprised an extraordinary era of discovery for me − not only about the Universe, but also about my place in it. My recent epiphanies could not have been possible without the love and support of my immediate family: Alexander Shreve, Katy Maness, Lanny Maness, Melinda Maness, Chad Maness, and Opal Maness, and my close friends: Bob Cadmus, Janet Casperson, James Graham, Emily Landes, Etsuko Mieda, Megan Reiter, Kristen Shapiro, Linda Strubbe, and Terry Yen.

I also wish to extend a warm thanks to my qualifying exam and dissertation committee members: Eugene Chiang, James R. Graham, Paul Kalas, Geoff Marcy, Richard Plambeck, and Richard Saykally, who served as invaluable guides for me over the last several years. I am also sincerely grateful to past collaborators and co-authors on the works published herein: R. Abuter, T. Alexander, G. B. Basri, R. P. Butler, E. I. Chiang, G. Duchene, F. Eisenhauer, M. P. Fitzgerald, E. B. Ford, R. Genzel, S. Gillessen, J. R. Graham, P. H. Hauschildt, D. C. Hines, P. Kalas, G. W. Marcy, F. Martins, S. A. Metchev, T. Ott, R. Paladini, T. Paumard, K. M. G. Peek, M. Salaris, K. Scherer, G. Schneider, C. Sheehy, A. T. Shreve, S. Trippe, and S. S. Vogt., as well as others who helped formulate many of the ideas presented in these chapters: J. Anderson, D. Fischer, R. Foley, C. Heiles, D. Kirkpatrick, M. Perrin, V. Platais, S. Redfield, and A. Sternberg.

Finally, I would be remiss to forget the funding sources and computational / instrument resources that made this work possible. Sources of funding include the Alexander von Humboldt Foundation, the Carnegie Institution of Washington, the Center for Adaptive Optics (managed by the University of California at Santa Cruz under cooperative agreement No. AST 9876783), the Graduate Opportunity Program at the University of California at Berkeley, the Michelson Fellowship Program, the Miller Institute for Basic Research, the Minerva Research Initiative (grant 8563), the NASA (grants NAG5-75005, NAG5-12182, and GO-10847 from the Space Telescope Science Institute, which is operated by Association of Universities for Research in Astronomy Incorporated, under NASA contract NAS5-26555), the National Science Foundation (Graduate Research Fellowship Program; grants AST-0205999, AST-0307493, AST-0909188, and AST-9988087), and the New Faculty grant by Sir H. Djangoly (CBE of London, UK), and the University of California Lab Research Program 09-LR-01-118057-GRAJ. Computational and instrument resources include the IAC-STAR Synthetic CMD computation code (suported and maintained by the computer division of the Instituto de Astrofisica de Canarias), the CARMA consurtium (supported through

the states of CA, IL, and MD, the Gordon and Betty Moore Foundation, the Eileen and Kenneth Norris Foundation, the Caltech Associates, and the National Science Foundation), the Keck telescope, and the Simbad database (operated at CDS, Strasbourg, France).

Chapter 1

Introduction

Research in star formation bridges over eight orders of magnitude in scale, from the study of the formation of individual planetary systems (scales of tens of astronomical units), to the study of global star formation in individual galaxies and its role in galaxy evolution (scales of tens of kiloparsecs). Galactic-scale questions include how giant molecular clouds form and evolve, how the galaxy-wide star formation rate is set, how star formation in clustered environments differs from that in distributed environments, and what determines the initial mass function. Questions focused on smaller scales probe how individual systems inherit properties from the medium from which they are formed and how those properties evolve with time, how stellar feedback influences the surrounding interstellar medium, and what determines the dynamical evolution of disks and their associated planet formation.

This thesis explores selected questions in star and planet formation. The following sections briefly put each chapter in the broader context of the more general questions defined above.

1.1 The Stellar Initial Mass Function

The stellar initial mass function (IMF) quantifies the rate of stellar creation as a function of mass. Its functional form is an essential prediction of any comprehensive theory of star formation (McKee & Ostriker 2007). Understanding the evolution of the IMF across time is also of fundamental importance to the field of galaxy evolution (Wilkins et al. 2008). Unfortunately, current theoretical models disagree on the functional form of the IMF and its dependence on environment (Hoversten & Glazebrook 2008; Elmegreen et al. 2008).

Milky Way observations of the disk, bulge, and halo are consistent with a universal IMF (Kroupa 2002; Zoccali et al. 2000; Paust et al. 2009). However, there is increasing evidence for localized environmental dependencies. Low-density star-forming regions in Taurus and Serpens, for example, exhibit systematic variations compared to the average Galactic IMF (Béjar et al. 2001; Oliveira 2008). The initial mass function of the dense, young stellar population in the Galactic Center also suggests a non-standard initial mass function (Paumard

et al. 2006). Extragalactic environments may additionally point to an environmental dependence (Béjar et al. 2001; Oliveira 2008; Meurer et al. 2009; Wilkins et al. 2008), though these observations are less convincing, as the stellar populations in these systems are unresolved.

Further resolved observations in extreme environments are needed to better constrain the extent to which the initial mass function can be considered universal and the circumstances in which deviations occur. Chapter 2 provides an example of such follow-up observations, by modeling the IMF of the old stellar population of the Galactic Center to test for variations similar to those observed for the young population. Preliminary findings suggest a similar variation may indeed be present.

1.2 Star Formation of Individual Protostellar Systems

1.2.1 Low and High Mass Star Formation

The mass distribution of Galactic cloud cores is similar in shape to the stellar IMF, suggesting the initial mass function is set quite early in the star formation process, and is thus unimportant in understanding the evolution of individual systems (Lada et al. 2008). Following the formation of individual systems according to the stellar IMF, the study of star formation is traditionally divided into two regimes: a low-mass regime ($M_* \lesssim 8M_\odot$) and a high-mass regime ($M_* \gtrsim 8M_\odot$) (Shu et al. 1987; McKee & Ostriker 2007). Low mass star formation begins with the quasistatic contraction of a dense core. Ambipolar diffusion removes magnetic support until the core becomes gravitationally unstable, allowing free-fall isothermal collapse. Matter far from the rotation axis of the envelope has too much angular momentum to fall onto the protostar and settles into a circumstellar disk, which drives the protostellar luminosity through subsequent accretion. Bipolar outflows develop perpendicular to the disk. The formation mass reservoir is gradually depleted through feedback and accretion, and a newly formed pre-main-sequence star emerges with a surrounding circumstellar disk.

High-mass star formation is less ordered than low-mass star formation, as the short Kelvin-Helmholtz time for massive stars means that nuclear burning ensues early in the formation process. This leads to significant feedback in the form of radiation pressure and photoionization before accretion from the protostellar envelope ceases; disks and jets are thus less distinct than for low mass stars. Observational studies of high-mass star formation are plagued by these rapid evolutionary timescales and the fact that because massive stars are rare, their formation sites are farther away than corresponding sites for low-mass star formation. Massive stars also tend to be born in regions of high dust obscuration and in highly dense clusters, imposing wavelength restrictions and complications in interpretation due to confusion. For these reasons, low-mass star formation is much better studied and understood than high-mass star formation. Because low mass stars live longer than their high mass counterparts and because disks surrounding low mass stars are much easier to identify and characterize, low mass star formation is also the focus of investigations in planet

formation (the subject of Chapters 3-5).

1.2.2 Observations of Low Mass Star Formation

The various stages of low mass star formation discussed in §1.2.1 are probed observationally according to four spectral energy distribution (SED) classifications, which roughly correspond to an evolutionary progression (Andre et al. 2000). A characteristic SED for each class is shown in Figure 1.1, taken from Lada (1999). Class 0 objects are completely embedded such that they are usually not detected in the optical and near-infrared. These sources have envelope masses greater than the protostellar mass; the majority of stellar mass is thought to be acquired at this stage. Class I objects may be detected in the near-infrared but are still embedded, with positive slopes in the infrared and significant (sub)millimeter luminosities. These objects generally have disks, in addition to envelopes. Class II objects are pre-main-sequence stars with negative infrared slopes and substantial disks. Class III objects show a significant deficit of near-infrared emission and show little, if any, sign of accretion.

Areas of active research at early stages include how protostars lose magnetic flux and angular momentum from their parent medium, how stars accrete at early stages and how this relates to observed protostellar luminosities, and what physical properties govern fragmentation in molecular cores (McKee & Ostriker 2007). Questions at late stages typically relate to the dynamical evolution of disks, jets, and outflows. Open questions include the role of initial conditions on the mass distribution of disks, the angular momentum transport mechanisms driving observed disk accretion rates, the formation of outflows and winds and their effect on the surrounding environment, and the processes governing disk dispersal.

1.3 Planet Formation Theory

A subfield of low mass star formation considers the way in which planets form and subsequently evolve in circumstellar disks, though current theories of planet formation are far less certain than those for low mass star formation in general (Armitage 2007). The current planet formation narrative proceeds as follows. First, dust is thought to grow in protoplanetary disks to centimeter sizes through direct collisions. The mode of growth beyond this size is unclear, as gas in the disk is thought to produce a strong headwind for centimeter-to-meter size bodies, leading them to rapidly spiral into the star on timescales of ~ 100 yr; gravitational fragmentation of a dense subdisk, for example, may be one way to overcome this problem (Chiang & Youdin 2010). Growth beyond kilometer size planetesimals is enabled through direct collisions, enhanced by gravitational focusing. A few bodies grow rapidly during a period of runaway growth until they become sufficiently massive to stir up surrounding planetesimals. Growth then proceeds at a slower rate until each large body reaches its isolation mass, dictated by the accreting body's initial mass and the surface density of planetesimals within its radius of gravitational influence (Goldreich et al. 2004a,b).

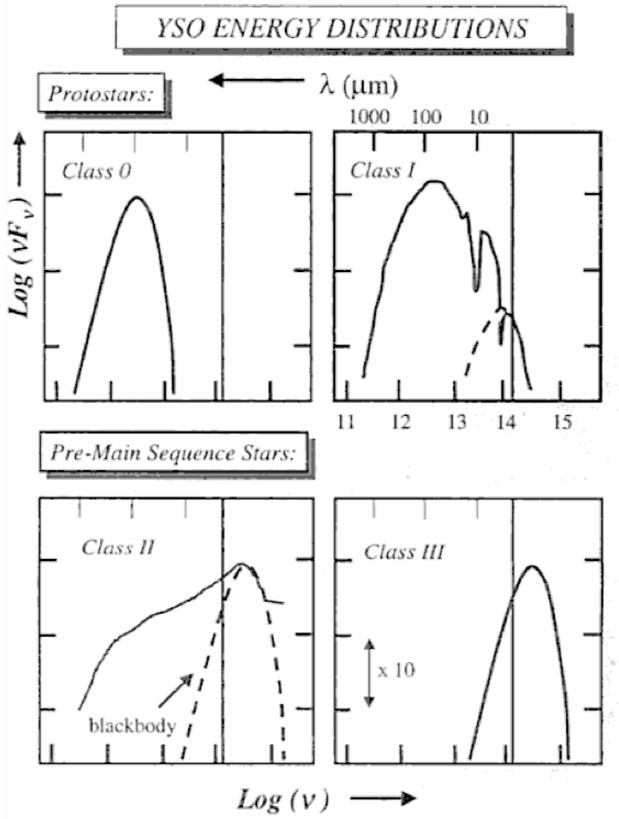

Figure 1.1 The empirical classification scheme for young stellar object spectral energy distributions, taken from Lada (1999). The vertical line at 2.2 μm is shown for reference in all panels. Embedded Class 0 sources are detected in cold dust emission at long, infrared-to-millimeter wavelengths. In addition to emission at long wavelengths, light coming directly from the nascent star can be observed in Class I and Class II sources. The luminosity of evolved Class III sources is significantly dominated by the stellar photosphere; the SED no longer shows a strong excess due to significant envelope or disk material.

The core accretion model for giant planet formation allows further growth when the core becomes massive enough to gravitationally maintain an envelope of gas in hydrostatic equilibrium. Under this scenario, the core then continues to accrete planetesimals until it reaches a critical mass, at which point the gas envelope contracts, and rapid gas accretion ensues (Pollack et al. 1996). The alternative model for giant planet formation, gravitational instability, posits that giant planets form when a cold or massive disk becomes gravitationally unstable, enabling fragmentation (Boss 1997). Planetary systems can evolve significantly after planet formation is largely complete, due to interaction between newly-formed planets and their parent gas disk (Goldreich & Tremaine 1980), interaction between planets and left-over planetesimals (Levison et al. 2007), and planet-planet scattering (Lin & Ida 1997).

1.4 Constraining Theories of Planet Formation and Evolution

Observational constraints on the problem of planet formation have become significantly more prevalent over the last fifteen years, through the characterization of the Kuiper Belt, high resolution imaging of protoplanetary and debris disks, and the discovery of many extrasolar planetary systems. Of these breakthroughs, the characterization of exoplanetary systems through radial velocity surveys is perhaps the most significant. The increased occurrence of detected radial velocity planets around high-metallicity stars, for instance, provides preliminary evidence for the core accretion model of giant planet formation, as a high metallicity enables an increased surface density of planetesimals, allowing faster core growth and a greater chance of reaching runaway gas accretion prior to disk clearing (Fischer & Valenti 2005). The large number of giant planets with sub-AU semi-major axes, as discovered with radial velocity surveys, has also significantly advanced theories of planetary migration. The eccentricity distribution of exoplanets and the discovery of exoplanets in mutual resonances have further provided valuable constraints for planetary system evolution (Marcy et al. 2005). Finally, radial velocity surveys have significantly enabled planet transit discoveries, which allow exoplanetary radius measurements and thus compositional constraints. Chapter 3 presents radial velocity data for such a planetary system that led to the transit detection of the closest, smallest, and least massive transiting planet at the time of discovery (Gillon et al. 2007a,b). The inferred radius and mass from these follow-up observations indicated a water-ice composition with a hydrogen and helium envelope, suggestive of significant inward migration. The migration could potentially be related to an outer planet, in further qualitative agreement with the available radial velocity data.

While the radial velocity technique has proven invaluable for advancing our understanding of planetary systems, this technique has several important limitations. First, reliable detection via this technique requires multi-epoch data over at least one orbital period; thus, current surveys are so far only able to detect planets out to ~ 5 AU. In contrast, the limited number of outer exoplanet detections provided by microlensing and direct imaging campaigns have suggested that planet formation on much larger scales of $\sim 10 - 100$ AU may

be prevalent (Beaulieu et al. 2006; Kalas et al. 2008; Marois et al. 2008). Observations of exoplanets on these outer scales are particularly important for testing the gravitational instability model of giant planet formation, as outer disks may be sufficiently cold for this mechanism to operate. Second, stellar activity at ages $\lesssim$ 100 Myr has historically biased radial velocity surveys to older stellar ages, whereas models of terrestrial planet formation and radioactive data for the Earth suggest terrestrial planet assembly is ongoing throughout the first $\sim$ 100 Myr (Raymond et al. 2005; Wadhwa et al. 2007). Finally, radial velocity surveys provide only a snapshot of any given planetary system in time, and efforts to deduce evolutionary histories from this data are complicated by the large range of possible initial conditions and uncertainties in the relevant physics (Ford et al. 2001).

A possible away around some of these difficulties is to attempt to indirectly infer the presence of exoplanets through their influence on an associated debris disk, a tenuous dust disk continuously replenished through collisions of larger planetesimals. Massive exoplanets may imprint their presence on the observed dust through their gravitational interaction with the dust or the parent bodies. Moreover, different grain sizes, traced by observations at different wavelengths, are expected to be differently affected; thus, multiwavelength resolved imaging of debris disks may be a promising path for inferring the presence of massive exoplanets in outer planetary systems (Wyatt 2006). An example of a debris disk system with potential multiwavelength structure pointing to such an exoplanet is provided in Chapter 4. Unfortunately, this technique is so far of limited utility, as uncertainties in models of grain dynamics make disk structures difficult to interpret at present. An example of a debris disk system that shows significant substructure that is unlikely to be gravitational in origin is presented in Chapter 5. The disk / ISM models presented in this chapter suggest that such interactions can possibly produce substructure that might mimic a disk / exoplanet interaction at short, scattered-light wavelengths.

Still, debris disk morphologies are a promising tool for advancing the current understanding of planetary system evolution, as they can in principle be used in conjunction with direct exoplanet detections to reconstruct the evolutionary history of solar systems. Indeed, the relationship between Neptune and resonant Kuiper Belt objects, which trace structures analogous to those seen in extrasolar debris disks, constrain the migration rate of Neptune and the evolution of the early Kuiper Belt (Malhotra 1995). A demonstration of this concept is provided by the debris disk surrounding Fomalhaut and its corresponding exoplanet (Kalas et al. 2008). For example, the shape of the dust belt together with the exoplanet detection suggest that the detected exoplanet likely formed in situ (at $\sim$ 100 AU) and gradually eroded the inner edge of the outer planetesimal belt. The planet is also thought to have stirred boulders within the belt that are continuously grinding into dust, some of which we are observing today (Chiang et al. 2009). These models for Fomalhaut place tight constraints on the mass of the imaged exoplanet and make predictions for the planet orbital elements that can be tested with future observations.

More generally, direct exoplanet detections together with debris disk morphologies may prove useful within the next several years for constraining evolutionary histories for a large number of systems. The upcoming Gemini Planet Imager, for example, is designed to si-

multaneously image both exoplanets and debris disks. The Atacama Large Millimeter Array (ALMA) is also likely to image debris disk morphologies on scales comparable to those for known radial-velocity planets. ALMA will further directly detect exoplanets astrometrically (Hales et al. 2010), enabling additional opportunities to probe disk / exoplanet interactions and reconstruct planetary system histories.

Chapter 2

Evidence for a Long-Standing Top-Heavy IMF in the Central Parsec of the Galaxy

Abstract

We classify 329 late-type giants within 1 parsec of Sgr A*, using the adaptive optics integral field spectrometer SINFONI on the VLT. These observations represent the deepest spectroscopic data set so far obtained for the Galactic Center, reaching a 50% completeness threshold at the approximate magnitude of the helium-burning red clump ($K_S \sim 15.5$ mag.). Combining our spectroscopic results with NaCo H and K_S photometry, we construct an observed Hertzsprung-Russell diagram, which we quantitatively compare to theoretical distributions of various star formation histories of the inner Galaxy, using a χ^2 analysis. Our best-fit model corresponds to continuous star formation over the last 12 Gyr with a top-heavy initial mass function (IMF). The similarity of this IMF to the IMF observed for the most recent epoch of star formation is intriguing and perhaps suggests a connection between recent star formation and the stars formed throughout the history of the Galactic Center.

2.1 Introduction

A growing body of evidence suggests that the stellar population of the Galactic nucleus is distinct from that of the bulge. Surface brightness measurements from the NIR to the FIR show that in contrast to the bulge, the central few hundred parsecs of the Galaxy are dominated by a flat, disk-like distribution of stars, gas, and dust (Kent 1992; Launhardt et al. 2002). This difference is also reflected in the kinematics: OH/IR stars in the central hundred parsecs show higher rotational velocities than expected for an inner single-component, bulge population (Lindqvist et al. 1992).

Evidence for ongoing star formation also distinguishes the nucleus from the bulge. The Galactic bulge is composed primarily of an old starburst-like population formed early, some 7–10 Gyr ago (Zoccali et al. 2003; van Loon et al. 2003; Zoccali et al. 2006; Ballero et al. 2007). In contrast, the Galactic nucleus harbors substantial young and intermediate-age stellar populations. Intermediate-age populations have been most commonly inferred from broad-band photometry (Rieke 1987; Narayanan et al. 1996; Davidge et al. 1997; Philipp et al. 1999; Alexander & Sternberg 1999; Figer et al. 2004). Star formation tracers have also been used to study intermediate-age populations, including young supergiants and luminous AGBs, which trace 10 Myr - 1 Gyr populations (Sellgren et al. 1987; Blum et al. 1996b,a), and OH/IR stars, which trace 1-3 Gyr populations (Wood et al. 1998; Sjouwerman et al. 1999). The young stellar populations in the Galactic nucleus have been the subject of much recent work. These populations are predominantly concentrated in three young, massive clusters: the Arches and Quintuplet clusters (Figer et al. 1999, 2002; Stolte et al. 2005, and references therein), approximately 30-50 pc in projected distance from the Galactic Center, and the Central Cluster, located within the central parsec (Krabbe et al. 1991, 1995; Paumard et al. 2006, and references therein).

Star formation in the nucleus is thought to be ultimately linked to the inward transport of gas induced by the Galactic bar (Morris & Serabyn 1996; Kormendy & Kennicutt 2004). However, precisely how gas is funneled from the outer galaxy to the nucleus and how this process affects the resultant star formation, remains poorly known. At present, there is a concentration of molecular gas 2-8 pc from the Galctic Center termed the circumnuclear disk (Guesten et al. 1987; Jackson et al. 1993; Serabyn et al. 1994). If such a structure routinely fuels star formation in the central parsec, the stars formed in this region may represent an entirely distinct population from the Arches and Quintpulet clusters or the intermediate age populations found throughout the $\sim$200 pc nucleus. Dynamical effects due to the supermassive black hole (Genzel et al. 2003, Ghez et al. 2005, and references therein) and the large stellar and remnant density in the central parsec may also lead to population differences between the Central Cluster and that in the larger nucleus, either prior to star formation or afterwards.

A number of investigators have attempted to address the nature of the Central Cluster and its relationship to the larger 100-300 pc nucleus. Most recently, Paumard et al. (2006) investigated the properties of the young stellar population in the central parsec, spectroscopically identifying nearly 100 OB and Wolf-Rayet stars. They find that the majority of the young stars reside in two, inclined and counter-rotating disks, suggesting in situ star formation in dense gas accretion disks. Studies of the older stellar population in the central parsec have been primarily limited to broadband photometry. They have suggested that the fraction of low mass stars in the population increases with distance from the center, perhaps due to dynamical mass segregation (Philipp et al. 1999; Genzel et al. 2003; Schödel et al. 2007).

A detailed analysis, however, of the late-type giant population requires spectroscopy, owing to the large scatter in extinction near the Galactic Center and the intrinsic variations in giant star colors. Blum et al. (2003) pioneered work in this area, using spectroscopic

and photometric observations of the most luminous giants and supergiants (50% complete at K_S ∼10 mag.) to construct an H-R diagram for stars in the inner 5 pc. They report that the GC star formation rate in the central few parsecs is largely similar to that of the bulge. Specifically, they find that the majority of stars formed more than 5 Gyr ago, though they also find evidence that significant star formation also occurred during the past 100 Myr. However, their conclusions are limited by their bright magnitude limit, which samples only short-lived evolutionary stages, for which theoretical models are uncertain.

In this paper, we build on the work of Blum et al. (2003) in an effort to better characterize the late-type giant population within the central parsec. We report deep photometric and spectroscopic observations of 329 late-type giants in the GC, complete to 50% at K_S ∼15.5 mag. Our observations for the first time include the helium-burning red clump, as well as the red giant branch and asymptotic giant branch. This improved magnitude limit allows for the most robust picture of the Galactic Center star formation history to date, as these stars are much better understood than the supergiants and luminous AGB stars studied by Blum et al. (2003). In §2, we present our observations and the techniques used to construct the Hertzsprung-Russell (H-R) diagram. Section 3 discusses the resulting H-R diagram and implications for the GC star-formation history. We discuss our results in §4 and conclude with §5.

2.2 Observations and Data Reduction

2.2.1 Spectroscopic Observations and T_{eff} Determination

We observed eight Galactc Center fields between March and September 2006 using the integral field spectrometer SPIFFI (Eisenhauer et al. 2003a,b) in conjunction with the MACAO adaptive optics module (Bonnet et al. 2003) mounted on the SINFONI ESO VLT facility. We observed these fields for the dual purpose of identifiying main sequence B stars outside the central parsec (Martins et al. 2007b, in prep) and gathering spectroscopic observations for a large number of late-type giants. We chose fields with a radial distance from Sgr A* of less than 20 arcsec, selecting regions outside the minispiral to avoid nebular contamination in Brackett γ, and choosing fields north of Sgr A* to minimize separation from the AO guide star. We also avoided regions with extremely bright stars ($K \lesssim 9$). As stars this bright are relatively rare, the selection bias in avoiding these stars is negligible. If the fields had instead been chosen at random, we expect no more than a few $K \lesssim 9$ stars would be selected.

We observed each selected SINFONI field in 50 × 100 mas pixel mode, resulting in 0.2 arcsec resolution and a $4.2'' \times 4.2''$ field of view. We simultaneously observed all fields in H and K band, leading to a spectral resolution of R ≈ 1500. Figure 2.1 displays the location of the observed fields. The total exposure time for all fields was 4200 s, except for the fields at (17″, 17″), (5″, 11″), and (-8″, 8″), which had total exposure times of 6600 s, 7200 s, and 2400 s, respectively. The fields span a range in projected distance from Sgr A* of 4 arcsec

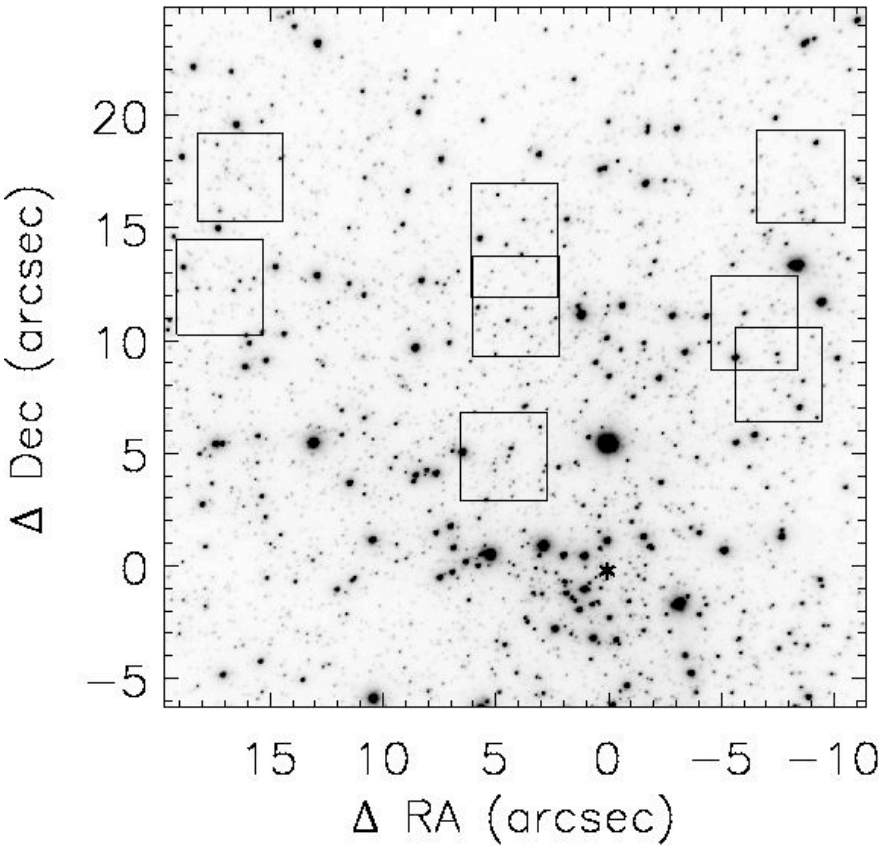

Figure 2.1 NaCo K_S band mosaic used to derive photometry. The eight regions for which we have SINFONI spectra are overplotted in black. The position of Sgr A* is shown with an *.

to 26 arcsec. A histogram of the observed stellar positions is shown in Figure 2.2.

We reduced the raw data using a standard procedure to perform flat-fielding, sky subtraction, and wavelength calibration (Schreiber et al. 2004). Following extraction, we removed the stellar continua by dividing by a second degree polynomial fitted to the line-free regions of the stellar spectra. The normalized spectra allow us to directly compare the VLT spectra to the normalized catalog spectra in Wallace & Hinkle (1997) and Kleinmann & Hall (1986). A typical resultant GC K band spectrum following normalization is shown in Figure 2.3. Three template spectra from the Wallace & Hinkle (1997) spectral library are also shown for comparison.

To classify the stars in our sample, we used the ^{12}CO 2.2935 μm, $\nu = 2-0$ rovibrational band head, the strongest feature in our spectra and a well-known $T_{\rm eff}$indicator, for a given luminosity class (Kleinmann & Hall 1986). We use only this feature, as it is largely free of nebular and telluric lines, making it more reliable than other $H-$ and $K-$band signatures in our spectra. We note that in contrast to the work of Blum et al. (1996b, 2003), we do not need the H+K band H_2O feature to reliably predict effective temperatures, as our sample

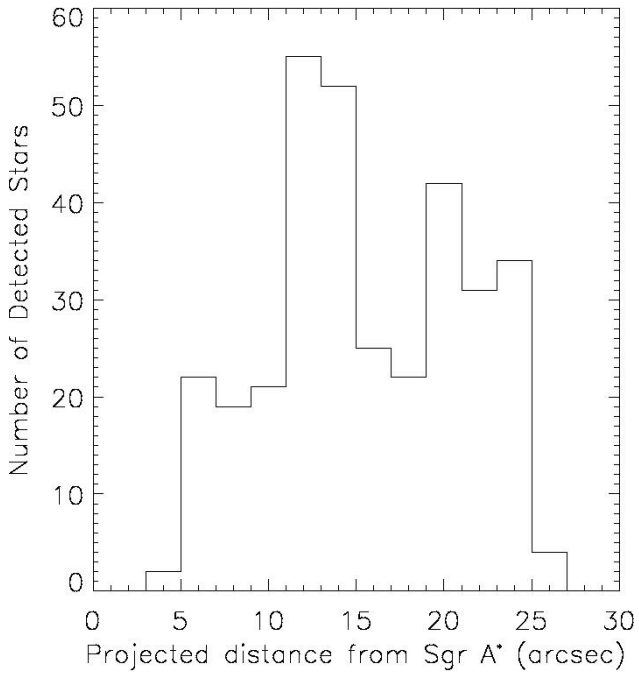

Figure 2.2 Histogram of stellar positions, corresponding to the stars detected in the spectroscopic fields marked in Figure 2.1.

consists only of giants with K_S >10.3 (see §2.2). Due to their rarity, stars sufficiently bright to be supergiant or long period variable candidates are not contained in our sample.

To define a T_{eff}- ^{12}CO index relation, we computed the CO index defined by Blum et al. (1996b). Although not as well-known as other CO indices (e.g. equivalent width, photometric indices of Frogel et al. (1978)), Blum et al. (1996b) showed that this index correlates well with other CO indices. Furthermore, it has the advantage of being insensitive to small variations in the nearby continuum because it does not require a fit to the continuum. The index is defined as CO % = $[(1 - F_{band}/ F_{cont}) \times 100)]$, where both bands are 0.015 μm wide and the continuum and CO band centers are defined as 2.284 μm and 2.302 μm, respectively. We note that although we adopt the same definition for the CO index as Blum et al. (1996b), our spectra are normalized while theirs are not, and thus, our computed indices are not directly comparable to theirs. We calculated uncertainties in the computed indices, assuming the noise is dominated by photon statistics of the source and background and that the uncertainty in the band is approximately equal to that of the nearby continuum.

Following Blum et al. (2003), we used CO strength to estimate effective temperatures for the cool giants in our GC sample. To define a CO index versus T_{eff}relation, we used a set of archival comparison star spectra taken from Wallace & Hinkle (1997) and Kleinmann & Hall (1986) with well-determined effective temperatures given in the literature. In an effort to avoid systematic errors in our derived index$-T_{eff}$relation, we used a large number of references, assuming temperatures derived from a wide variety of methods. A summary

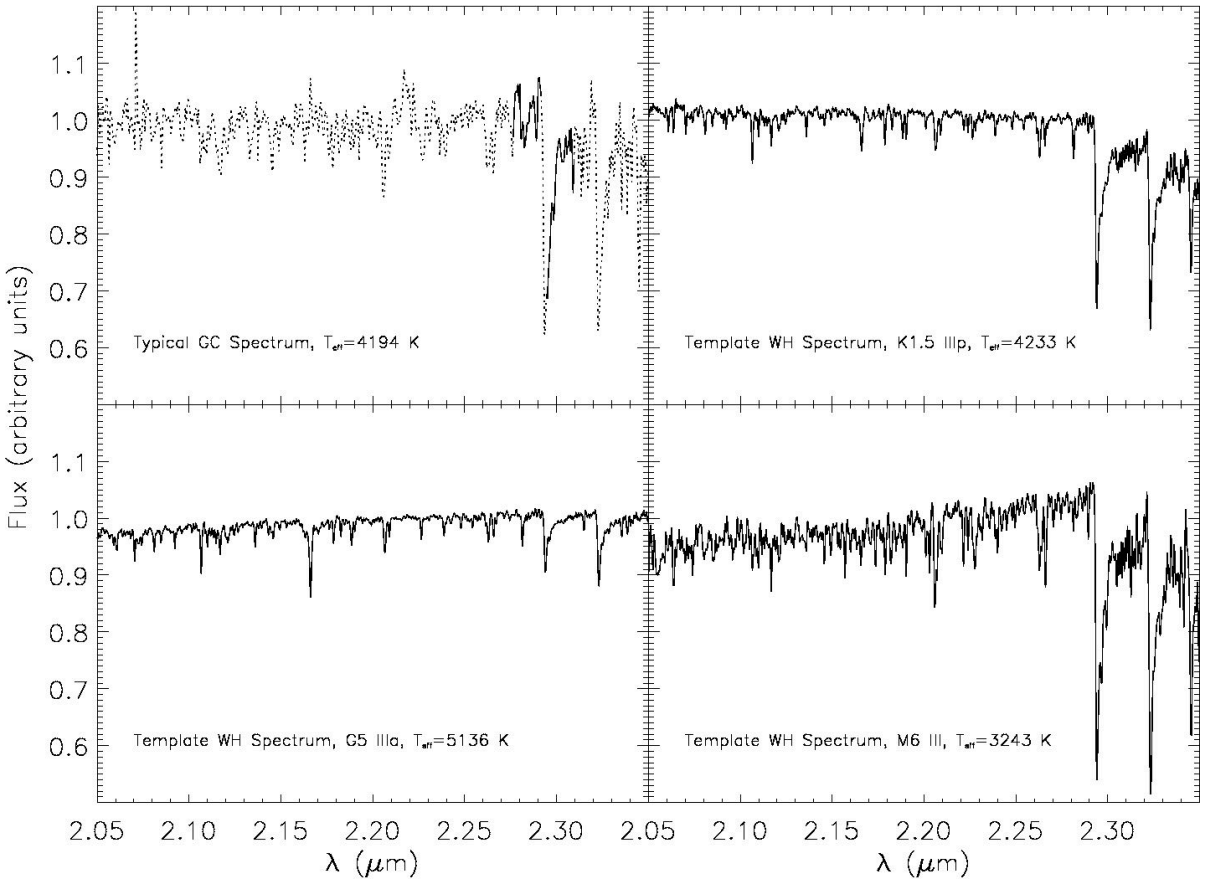

Figure 2.3 A typical stellar spectrum from the Galactic Center fields. The position of the ^{12}CO 2.2935 μm ν=2-0 rovibrational bandhead and nearby continuum used to calculate the CO-index is shown as a solid line. Three template spectra from the Wallace & Hinkle (1997) spectral library are also shown for comparison.

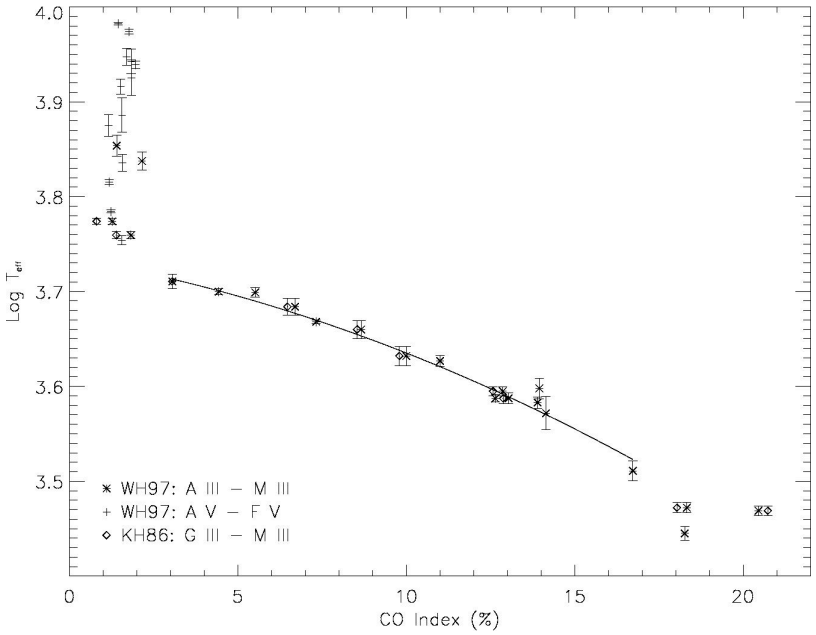

Figure 2.4 The 2.3 μm CO index (see text for definition) as a function of temperature for the comparison stars taken from the Wallace & Hinkle (1997) and Kleinmann & Hall (1986) catalogs. The solid line is a least-squares fit to both data sets for stars with $17 > \mathrm{CO} \geq 3$.

of the comparison star data is given in Table 2.1, and the resulting relationship between CO index and $T_{eff}$is shown in Figure 2.4. The Wallace & Hinkle (1997) and Kleinmann & Hall (1986) relationships are in very good agreement with each other (for stars in common, ΔCO $< 0.5\%$), suggesting that the CO index is largely independent of resolution or observing system. The relation is tightest for CO $\lesssim 17$. As no stars in our GC sample have computed indicies exceding this value, we did not include comparison stars with CO > 17 in our fit. The resulting index-T_{eff}relation using both empirical data sets is: $\log T_{eff} = 3.7351 - 0.0060 \times \mathrm{CO} - 0.00040 \times \mathrm{CO}^2$, for all stars with measured indices $17 > \mathrm{CO} \geq 3$. The errors in the derived coefficients are 0.0092, 0.0022, and 1.2×10^{-4}, respectively.

In order to separate cool giants from warmer giants and main sequence stars, warm stars with CO < 3 are removed from the sample. Of the 355 detected stars in our spectroscopy, 329 were categorized as CO-absorbers, and we assigned effective temperatures to these stars using the above index$-T_{eff}$relation. Prior to temperature calculation, we cross-correlated all CO-absorbing stars with a CO-template in order to remove radial velocities. Errors in temperatures were estimated based on the noise in each spectrum and the intrinsic dispersion in our index$-T_{eff}$relation ($\sigma = 0.0050$). As noted by Ramirez et al. (1997), errors determined in this way are strictly only lower limits. The spectral classification and analysis of the remaining early-type (non-CO-absorbing) stars in our sample is less straight-forward (Martins et al. 2007a), and we defer analysis of these stars to a later paper (Martins et al. 2007b, in prep).

Table 2.1. Comparison star properties

Name	Sp Type	Catalog	CO (%)	ΔCO (%)	T_{eff}(K) (K)	ΔT_{eff} (K)	T_{eff} Reference
HR 7001	A0 Va	WH	1.760	0.004	9420	60	Smalley (1993)
HR 4295	A1 V	WH	1.434	0.003	9600	25	Adelman et al. (2002)
HR 5054	A1 Vp	WH	1.823	0.004	8760	260	Sokolov (1998)
HR 6378	A2 V	WH	1.953	0.004	8690	78	Blackwell & Lynas-Gray (1998)
HR 4534	A3 V	WH	1.695	0.005	8857	185	Malagnini & Morossi (1997)
HR 4357	A4 V	WH	1.516	0.007	8243	150	Smalley (1993)
HR 7557	A7 V	WH	1.147	0.004	7500	200	Theodossiou & Danezis (1991)
HR 2943	F5 IV-V	WH	1.176	0.014	6532	39	Ramírez & Meléndez (2005)
HR 6927	F7 V	WH	1.219	0.014	6087	22	Taylor (2003)
HR 4375	F8.5 V	WH	1.540	0.015	5676	66	Taylor (2003)
HR 21	F2 III	WH	1.563	0.011	6847	137	Blackwell & Lynas-Gray (1994)
HR 403	A5 III-IV	WH	1.828	0.008	8420	360	Malagnini & Morossi (1990)
HR 1412	A7 III	WH	1.554	0.007	7690	320	Sokolov (1998)
HR 1457	K5+ III	WH	12.633	0.023	3866	35	Alonso et al. (1999)
HR 2985	G8 III	WH	5.540	0.018	5001	56	Alonso et al. (1999)
HR 3003	K4 III	WH	13.944	0.023	3961	99	Alonso et al. (1999)
HR 3323	G5 IIIa	WH	3.045	0.017	5136	88	Alonso et al. (1999)
		KH	3.039	0.007			
HR 4031	F0 III	WH	2.145	0.011	6880	150	Smalley (1993)
HR 4069	M0 III	WH	14.143	0.021	3730	149	Engelke (1992)
HR 4517	M1 III	WH	13.894	0.019	3828	53	Feast (1996)
HR 4883	G0 IIIp	WH	1.819	0.014	5747	54	Blackwell & Lynas-Gray (1998)
		KH	1.377	0.007			
HR 5017	F3 III	WH	1.395	0.017	7141	181	Alonso et al. (1999)
HR 5340	K1.5 IIIp	WH	10.997	0.021	4233	55	Alonso et al. (1999)
HR 6299	K2 III	WH	8.653	0.020	4571	100	Bell & Gustafsson (1989)
		KH	8.530	0.009			
HR 6703	G8.5 III	WH	4.426	0.020	5011	35	Blackwell & Lynas-Gray (1998)
HR 6705	K5 III	WH	12.859	0.023	3934	42	Alonso et al. (1999)
		KH	12.569	0.010			
HR 7635	M0− III	WH	13.035	0.025	3867	50	Alonso et al. (1999)
		KH	12.869	0.010			
HR 7806	K2.5 III	WH	9.993	0.022	4286	100	Bell & Gustafsson (1989)
		KH	9.785	0.010			
HR 7886	M6 III	WH	16.722	0.025	3243	79	Perrin et al. (1998)
HR 8317	K0.5 III	WH	7.319	0.024	4658	19	Gray & Brown (2001)
HR 8694	K0− III	WH	6.691	0.021	4830	100	Bell & Gustafsson (1989)
		KH	6.463	0.010			
HR 8905	F8 III	WH	1.265	0.014	5942	42	Blackwell & Lynas-Gray (1998)
		KH	0.797	0.007			
SWVir	M7 III	WH	18.350	0.024	2966	36	Dyck et al. (1996)
		KH	18.033	0.008			
BKVir	M7− III	WH	20.449	0.022	2944	34	Perrin et al. (1998)
		KH	20.730	0.006			
RXBoo	M7.5-8 III	WH	18.262	0.024	2786	46	Perrin et al. (1998)

2.2.2 Photometric Observations

We made photometric observations using the imaging system NAOS/CONICA (NaCo), consisting of the adaptive optics system NAOS (Rousset et al. 2003) and the NIR camera CONICA (Hartung et al. 2003) at the 8.2-m UT4 (Yepun) of the ESO VLT. In April 2006, we collected several AO-corrected images in each of H and K_S band with a pixel size of $\delta x = 27$ mas. The total exposure time was 64 s for each band, broken into thirty-two dithered images, in which every fourth image was separated from the previous exposure by 16 arcsec. We used our standard reduction pipeline to perform sky subtraction, bad pixel corrections, flat field corrections, and stacking of images to create final mosaics. In Figure 2.1, we display a sub-section of the final K_S band mosaic, containing all stars analyzed in this paper. Photometry was extracted for only this region to help ensure PSF constancy across the image.

We used the crowded field photometry package StarFinder (Diolaiti et al. 2000) to establish relative photometry and source detection. An empirical PSF for the central core (FWHM $\simeq$ 0.10 arcsec) was extracted from each image using seven bright, isolated stars. The full radial extent of the extracted PSF was r $\simeq$ 0.19 arcsec. To derive the photometric curve of growth needed to place these results on an absolute scale, we adopted the MTF-fitting technique of Sheehy et al. (2006). This technique fits the power spectrum of the image using a combination of the source spatial distribution function determined by StarFinder and a parameterized description of the modulation transfer functions (MTF) of the atmosphere, telescope, AO system, and science camera. The advantage of this technique is that it derives the PSF encircled energy curve of growth, including the extended, seeing-limited halo, and thus provides the aperture correction required for absolute photometric calibration. In deriving the curve of growth from the data themselves, we avoid systematic calibration errors introduced from using a PSF standard acquired at a different time and under different observing conditions than the target data. Given the rapid variations in AO performance (Fitzgerald & Graham 2006; Vacca et al. 2007), this technique is crucial for deriving accurate absolute photometry.

The MTF-fitting technique has so far only been applied to data obtained for the Keck Observatory LGSAO system (Sheehy et al. 2006; Vacca et al. 2007). To apply this technique to the VLT images, we used the Sheehy et al. (2006) software with appropriate input parameters for the VLT telescope pupil size and geometry, the camera platescale and pixel size, and the deformable mirror actuator spacing. The software uses the IDL procedure MPFIT[1] to perform a Levenberg-Marquardt least-squares fit of the parameterized model MTF to the data. The best fits to the H and K_S band image power spectra are shown in Figure 2.5. The spatial frequency, ν_n, is normalized relative to the telescope cutoff frequency in the image plane (D_{tel}/λ).

All images, even seeing-limited images, contain power up to the spatial frequency cutoff, which is D/λ for a circular pupil. To faithfully record all spatial information allowed by the telescope aperture, the pixel sampling frequency must therefore satisfy $1/\delta x \geq 2D/\lambda$ (see

[1]Available at http://cow.physics.wisc.edu/ craigm/idl/.

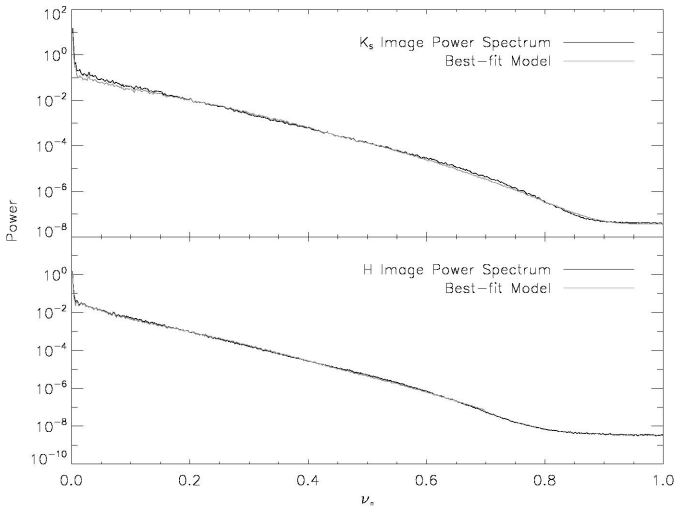

Figure 2.5 Comparison of the image power spectra to the best-fit models based on the parameterization of Sheehy et al. (2006). The H band data are aliased, and we therefore, fit only the power spectrum for $\nu_n < 0.7$ (see §2.2). The spatial frequency, ν_n, is normalized relative to the cutoff frequency in the image plane (D_{tel}/λ). The Strehl ratios implied by these fits are 10±0.5% and 19±1.0% , for H and K_S band, respectively.

Sheehy et al. (2006) for a detailed discussion). The K_S band data are Nyquist-sampled: $(1/\delta x)/(2D/\lambda) = 1$. However, the H-band data are undersampled: $(1/\delta x)/(2D/\lambda) = 0.76$. This aliasing causes power at frequencies $0.76 < \nu_n < 1$ to corrupt frequencies $0.52 < \nu_n < 0.76$. The contamination of frequencies between 0.52 and ∼0.7 is negligible, as the power aliased to these frequencies consists only of detector and background noise. This power is orders of magnitude less than the non-aliased power at these spatial frequencies, and thus, has very little effect on the total power spectrum. On the other hand, the aliased power for contaminated spatial frequencies $\nu_n \gtrsim 0.7$ is of the same order-of-magnitude as the non-aliased power, so the power spectrum at these frequencies is heavily influenced by the aliasing. We, therefore, chose only to fit the power spectrum for all spatial frequencies $\nu_n < 0.70$. As only detector and background noise contribute to the power spectrum for spatial frequencies $\nu_n \gtrsim 0.8$, we are excluding very little information about the PSF.

The relatively minor discrepency in Figure 2.5 between the model and data power spectra in K_S band is likely due to uncertainties in the deformable mirror influence function, as an explicit description of the VLT CILAS mirror influence function was not available. We, therefore, used the approximate influence function for the Keck Xinetics mirror from van Dam et al. (2004). The overall power spectra fits are satisfactory, and we do not expect that the photometric accuracy of our technique is significantly affected by this choice.

The Strehl ratios implied by the PSFs reconstructed from the fits in Figure 2.5 are 10% and 19%, for H and K_S band, respectively. To test the integrity of these fits, we divided the images into nine subimages and fit the power spectrum of each subimage. This process

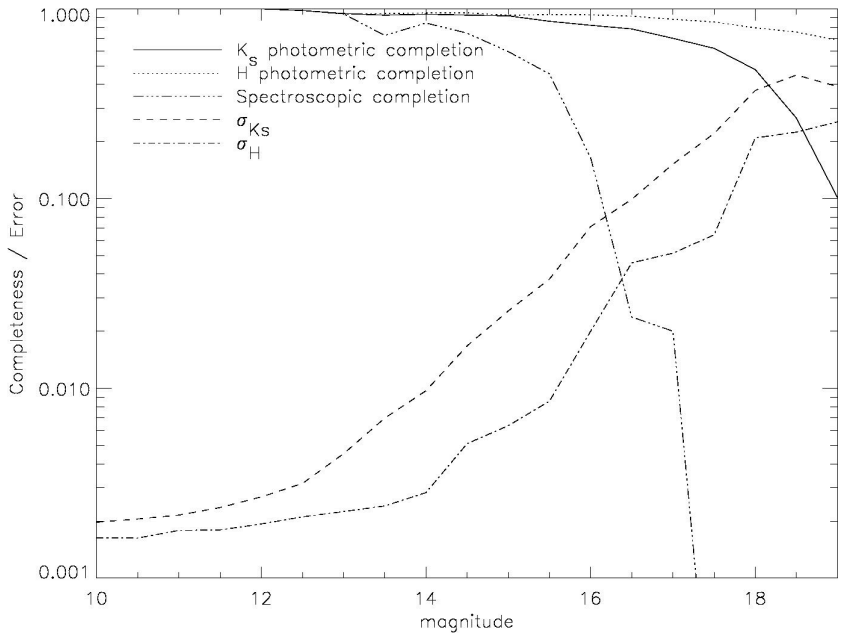

Figure 2.6 H and K_S band photometric errors and completeness based on the artificial star tests described in §2. The spectroscopic completeness is estimated based on the number of CO-stars for which we could extract spectra, compared to the total number of stars detected in the photometry.

yielded fairly consistent results for all subimages, implying an error in the H and K_S band Strehl ratios of 0.5% and 1.0%, respectively. This agreement between subimages suggests that PSF variations due to variable distance from the guide star and variable exposure time in the final mosaic are only present at a low level.

We determined the photometric zero point from observations of the near-IR standard star 9178 (Persson et al. 1998), obtained on the same night. The measured atmospheric extinction coefficients used to correct for the difference in airmass between our standard stars and science targets were 0.06 mag. airmass^{-1} for H and 0.07 mag. airmass^{-1} for K_S.

We derived photometric errors and completeness using the standard technique of inserting and recovering artificial stars of specified magnitude. Completeness is not uniform, so we calculated errors and completeness separately for each spectral field. To avoid artificially crowding our images, we inserted only fifty stars at a time to each spectral subimage and repeated this procedure five times for each magnitude bin. We computed the photometric error at each magnitude using a Gaussian fit to the difference between the input and recovered magnitudes. Figure 2.6 shows the average photometric errors and completeness at each magnitude bin. Also shown is the spectroscopic completeness, estimated by comparing the number of stars detected in the H and K_S band photometry to the number detected in the SINFONI data. The incompleteness in the SINFONI data at K_S ∼13-15 mag. is caused by crowding and confusion with nearby bright stars in the field of view.

2.3 Results

2.3.1 Hertzsprung-Russell Diagram Construction

Using the derived photometry and effective temperatures presented in the preceding section, we are able to place our GC sample on the Hertzsprung-Russell (H-R) diagram. To convert the measured photometric magnitudes to luminosity, we use models that assume the K band magnitudes are measured in the Johnson-Cousins-Glass system (Bessell & Brett 1988). Therefore, we first transformed the measured K_S magnitudes to the Johnson-Cousins-Glass system, using the approximate transformations given in Carpenter (2001), assuming the NaCo and 2MASS JHK_S color systems are identical, as in McCaughrean et al. (2004). We next adopted empirical bolometric corrections of Fluks et al. (1994) for M stars and theoretical corrections of Girardi 2005 (http://pleiadi/pd.astro.it) for hotter stars. For the theoretical corrections, we assumed a solar metallicity and a surface gravity of $\log g = 2.0$, though the results are largely independent of these assumptions. For all temperatures in the Galactic Center sample, we found systematic differences < 0.05 mag. in BC_K for $\Delta[M/H] = 1.0$ dex and $\Delta \log g = 1.0$ dex, leading to systematic differences in the luminosity of $\Delta \log(L/L_\odot) \lesssim 0.02$. Additionally, we assumed a distance to the Galactic Center of 8.0 kpc (Reid 1993; Eisenhauer et al. 2003c). There has been much recent debate concerning the precise distance to the Galactic Center. However, the choice of distance has only a small systematic effect on our derived luminosities; a change in distance of $\Delta d = 0.4$ kpc induces a change in luminosity of $\Delta \log(L/L_\odot) \sim 0.05$. Finally, we corrected each star's luminosity individually for extinction using the photometric color, the derived $\mathrm{T_{eff}}$, and the interstellar extinction law of Rieke (1999), derived from NICMOS observations of Galactic Center stars. All results are tabulated in Table 2.2.

Table 2.2: Properties of the late-type Galactic Center stars

ID	ΔRA ($''$)	ΔDec ($''$)	K (mag)	σ_K (mag)	H (mag)	σ_H (mag)	CO (%)	log $\mathrm{T_{eff}}$	$\sigma_{\log T_{eff}}$	A_K (mag)	σ_{A_K} (mag)	$\log(L/L_\odot)$	$\sigma_{\log(L/L_\odot)}$
1	6.26	6.24	15.275	0.042	17.419	0.072	8.28	3.658	0.006	2.99	0.15	1.88	0.06
2	6.32	6.05	15.259	0.042	17.316	0.072	8.30	3.658	0.007	2.86	0.15	1.83	0.07
3	5.67	5.91	14.898	0.031	17.051	0.056	6.93	3.674	0.004	3.03	0.11	2.09	0.05
4	5.67	6.13	14.239	0.013	16.344	0.049	8.61	3.654	0.006	2.93	0.09	2.25	0.04
5	5.51	6.24	15.304	0.042	17.438	0.072	7.01	3.673	0.005	3.00	0.15	1.91	0.06
6	5.02	6.48	15.531	0.042	17.826	0.204	7.15	3.672	0.008	3.23	0.37	1.91	0.15
7	4.86	6.29	15.131	0.031	17.274	0.072	7.01	3.673	0.007	3.01	0.14	1.98	0.06
8	4.99	6.16	15.327	0.042	17.406	0.072	7.34	3.669	0.005	2.91	0.15	1.86	0.06
9	4.75	6.13	15.503	0.042	17.678	0.072	8.76	3.652	0.006	3.03	0.15	1.78	0.06
10	4.35	6.34	15.474	0.042	17.135	0.056	6.82	3.675	0.004	2.30	0.12	1.57	0.05
11	4.35	6.51	15.240	0.031	17.387	0.072	6.69	3.677	0.004	3.02	0.14	1.96	0.06
12	3.54	6.56	14.318	0.017	16.427	0.049	7.73	3.665	0.005	2.95	0.09	2.26	0.04
13	3.56	6.40	13.803	0.013	15.707	0.012	9.40	3.643	0.005	2.62	0.03	2.27	0.02
14	3.48	6.13	14.969	0.031	16.899	0.056	6.90	3.675	0.005	2.70	0.11	1.93	0.05
15	3.08	6.13	12.132	0.003	14.305	0.006	11.62	3.611	0.005	2.96	0.02	2.99	0.01
16	3.05	5.83	14.123	0.013	16.226	0.042	8.65	3.653	0.006	2.93	0.08	2.30	0.04
17	2.81	5.86	15.867	0.078	17.802	0.204	8.77	3.652	0.005	2.67	0.39	1.49	0.16
18	3.27	5.62	15.596	0.042	17.751	0.204	9.25	3.645	0.007	2.99	0.37	1.71	0.15
19	2.78	5.32	15.115	0.031	17.234	0.056	9.20	3.646	0.007	2.94	0.11	1.88	0.05
20	4.35	5.18	11.399	0.002	13.519	0.003	12.10	3.604	0.005	2.87	0.01	3.23	0.01
21	4.78	5.37	14.438	0.017	16.735	0.049	9.71	3.639	0.004	3.19	0.09	2.24	0.04
22	5.13	5.51	15.436	0.042	17.641	0.072	8.55	3.655	0.004	3.08	0.15	1.84	0.06
23	4.97	5.10	15.341	0.042	17.335	0.072	10.09	3.634	0.005	2.74	0.15	1.68	0.06
24	5.53	4.54	14.770	0.031	17.054	0.056	6.77	3.676	0.006	3.22	0.11	2.22	0.05
25	5.10	3.46	14.078	0.013	15.666	0.012	8.31	3.658	0.005	2.17	0.03	2.02	0.02
26	5.16	3.67	15.087	0.031	17.025	0.056	9.92	3.636	0.011	2.66	0.12	1.76	0.06
27	5.45	3.91	15.316	0.042	17.369	0.072	10.07	3.634	0.007	2.82	0.15	1.73	0.06
28	5.08	4.18	13.152	0.005	15.121	0.006	10.32	3.631	0.006	2.69	0.02	2.53	0.02
29	5.13	4.51	13.238	0.005	15.345	0.012	10.91	3.622	0.005	2.88	0.02	2.55	0.02
30	5.05	4.70	13.980	0.013	16.298	0.049	12.37	3.600	0.007	3.16	0.09	2.30	0.04

ID	ΔRA	ΔDec	K	σ_K	H	σ_H	CO	log $T_{\rm eff}$	$\sigma_{\log T_{eff}}$	A_K	σ_{A_K}	$\log(L/L_\odot)$	$\sigma_{\log(L/L_\odot)}$
	($''$)	($''$)	(mag)	(mag)	(mag)	(mag)	(%)			(mag)	(mag)		
31	4.56	4.56	13.382	0.009	15.542	0.012	8.63	3.653	0.004	3.01	0.03	2.63	0.02
32	4.29	4.29	15.536	0.042	17.606	0.072	7.99	3.662	0.004	2.89	0.15	1.74	0.06
33	4.59	4.13	16.137	0.078	18.223	0.204	5.27	3.692	0.003	2.95	0.39	1.61	0.16
34	4.40	3.48	13.845	0.013	15.739	0.012	8.65	3.653	0.006	2.62	0.03	2.28	0.02
35	4.24	3.70	13.676	0.009	15.619	0.012	7.61	3.666	0.005	2.71	0.03	2.42	0.02
36	4.32	3.02	13.194	0.005	15.295	0.012	9.46	3.642	0.005	2.91	0.02	2.63	0.02
37	3.00	3.32	12.562	0.003	14.834	0.006	3.70	3.707	0.004	3.24	0.01	3.20	0.01
38	3.11	3.83	15.976	0.078	18.227	0.204	9.31	3.645	0.008	3.13	0.39	1.61	0.16
39	3.62	3.56	15.106	0.031	17.234	0.056	5.89	3.686	0.004	3.00	0.11	2.03	0.05
40	4.02	3.97	15.532	0.042	17.603	0.072	7.97	3.662	0.006	2.89	0.15	1.74	0.06
41	3.62	4.05	15.160	0.031	17.431	0.072	9.04	3.648	0.005	3.17	0.14	1.96	0.06
42	2.92	4.13	12.738	0.003	15.117	0.006	12.73	3.594	0.005	3.23	0.02	2.82	0.02
43	-6.97	10.15	15.030	0.026	16.988	0.058	8.98	3.649	0.008	2.71	0.11	1.83	0.05
44	-7.24	10.31	14.751	0.026	16.765	0.058	7.28	3.670	0.006	2.82	0.11	2.05	0.05
45	-7.10	9.85	15.112	0.026	17.048	0.058	5.96	3.685	0.006	2.72	0.11	1.91	0.05
46	-7.32	9.88	15.075	0.026	17.022	0.058	6.46	3.680	0.006	2.73	0.11	1.91	0.05
47	-7.94	9.88	15.494	0.040	17.295	0.060	4.70	3.698	0.006	2.53	0.13	1.72	0.06
48	-8.99	10.12	13.124	0.005	15.144	0.008	10.30	3.631	0.008	2.77	0.02	2.57	0.02
49	-8.80	9.67	15.374	0.040	17.408	0.060	7.61	3.666	0.009	2.84	0.13	1.80	0.06
50	-9.29	9.37	15.199	0.026	17.210	0.058	8.72	3.652	0.007	2.79	0.11	1.81	0.05
51	-8.69	9.21	15.156	0.026	17.093	0.058	6.25	3.682	0.006	2.71	0.11	1.88	0.05
52	-7.45	9.37	11.937	0.003	13.686	0.002	5.88	3.686	0.004	2.44	0.01	3.07	0.01
53	-5.59	9.21	10.319	0.002	12.222	0.002	11.08	3.619	0.008	2.58	0.02	3.59	0.02
54	-6.75	8.80	15.448	0.040	17.392	0.060	6.35	3.681	0.005	2.72	0.13	1.76	0.06
55	-6.75	8.56	15.948	0.090	18.090	0.245	6.47	3.679	0.008	3.02	0.46	1.68	0.19
56	-6.18	8.18	15.273	0.040	17.416	0.060	8.85	3.651	0.009	2.98	0.13	1.85	0.06
57	-6.29	8.07	15.706	0.040	17.964	0.245	8.91	3.650	0.007	3.15	0.44	1.74	0.18
58	-6.10	7.86	15.506	0.040	17.688	0.060	4.64	3.699	0.005	3.10	0.13	1.94	0.06
59	-5.97	7.29	15.037	0.026	17.188	0.058	4.32	3.702	0.008	3.05	0.11	2.12	0.05
60	-6.16	6.43	13.182	0.005	15.300	0.009	7.56	3.667	0.008	2.97	0.02	2.73	0.02
61	-6.51	6.64	15.628	0.040	17.772	0.245	9.21	3.646	0.008	2.98	0.44	1.69	0.18
62	-6.80	6.86	14.604	0.022	16.766	0.058	7.46	3.668	0.006	3.03	0.11	2.19	0.05
63	-7.32	7.78	13.190	0.005	15.195	0.008	8.64	3.653	0.006	2.78	0.02	2.61	0.02
64	-7.45	8.29	15.413	0.040	17.374	0.060	6.44	3.680	0.005	2.75	0.13	1.79	0.06
65	-7.64	8.56	15.467	0.040	17.477	0.060	6.86	3.675	0.006	2.82	0.13	1.78	0.06
66	-7.48	8.99	12.976	0.005	14.980	0.008	12.14	3.603	0.009	2.70	0.03	2.53	0.02
67	-8.23	8.88	15.498	0.040	17.511	0.060	5.75	3.687	0.008	2.83	0.13	1.81	0.06
68	-8.91	8.64	15.444	0.040	17.651	0.060	9.59	3.641	0.008	3.06	0.13	1.79	0.06
69	-8.59	8.18	12.292	0.004	14.300	0.005	8.80	3.651	0.005	2.78	0.01	2.97	0.02
70	-8.13	8.13	14.233	0.010	16.282	0.047	8.98	3.649	0.009	2.84	0.09	2.21	0.04
71	-8.18	8.32	15.497	0.040	17.501	0.060	7.83	3.664	0.007	2.79	0.13	1.72	0.06
72	-7.94	8.45	15.375	0.040	17.420	0.060	9.34	3.644	0.007	2.83	0.13	1.73	0.06
73	-7.75	8.26	15.616	0.040	17.814	0.245	6.29	3.682	0.006	3.10	0.44	1.85	0.18
74	-7.97	7.51	12.569	0.004	14.867	0.008	10.02	3.635	0.009	3.19	0.02	2.97	0.02
75	-7.61	7.21	14.774	0.026	16.954	0.058	5.67	3.688	0.007	3.08	0.11	2.20	0.05
76	-8.45	6.99	10.843	0.002	13.278	0.002	12.81	3.593	0.013	3.32	0.03	3.60	0.03
77	-9.21	6.53	12.543	0.004	14.852	0.008	10.86	3.623	0.008	3.18	0.02	2.95	0.02
78	-8.64	7.34	15.402	0.040	17.464	0.060	8.56	3.654	0.007	2.87	0.13	1.76	0.06
79	2.94	12.93	15.314	0.049	16.938	0.055	5.66	3.688	0.004	2.26	0.13	1.65	0.06
80	2.67	12.74	14.953	0.027	16.828	0.055	7.95	3.662	0.005	2.60	0.11	1.86	0.05
81	2.54	12.45	15.140	0.027	16.947	0.055	8.00	3.661	0.006	2.50	0.11	1.74	0.05
82	2.59	12.04	15.189	0.027	16.632	0.046	4.90	3.696	0.005	2.00	0.09	1.62	0.04
83	3.21	12.69	16.003	0.075	17.874	0.210	7.56	3.667	0.007	2.60	0.40	1.45	0.16
84	3.00	12.64	15.868	0.075	17.752	0.210	6.33	3.681	0.006	2.64	0.40	1.56	0.16
85	5.62	11.88	15.501	0.049	17.546	0.080	9.55	3.641	0.006	2.82	0.17	1.67	0.07
86	5.83	11.42	11.834	0.003	14.160	0.003	13.30	3.585	0.007	3.14	0.02	3.11	0.02
87	5.94	11.12	13.811	0.011	16.328	0.046	10.99	3.621	0.008	3.49	0.09	2.56	0.04
88	5.48	11.45	13.479	0.008	16.289	0.046	11.75	3.609	0.007	3.90	0.08	2.83	0.04
89	5.18	11.53	15.624	0.049	17.880	0.210	6.90	3.675	0.005	3.18	0.38	1.86	0.16
90	4.83	11.74	15.531	0.049	17.641	0.080	7.38	3.669	0.005	2.96	0.17	1.79	0.07
91	4.78	11.53	15.510	0.049	17.643	0.080	4.91	3.696	0.006	3.02	0.17	1.90	0.07
92	4.35	11.69	14.863	0.027	16.784	0.055	8.03	3.661	0.005	2.67	0.11	1.92	0.05
93	3.70	11.42	12.593	0.003	14.495	0.006	5.95	3.685	0.003	2.67	0.01	2.90	0.01
94	3.43	11.39	13.861	0.011	15.757	0.042	8.13	3.660	0.005	2.63	0.08	2.30	0.03
95	2.38	10.96	12.391	0.003	14.350	0.006	11.31	3.616	0.004	2.66	0.01	2.78	0.01
96	2.59	10.77	13.164	0.005	14.799	0.006	6.53	3.679	0.004	2.26	0.01	2.49	0.01
97	3.16	10.69	14.694	0.019	16.701	0.046	5.54	3.690	0.006	2.83	0.09	2.13	0.04
98	3.73	10.53	12.842	0.005	14.355	0.006	8.50	3.655	0.005	2.06	0.01	2.47	0.01
99	4.51	10.85	11.905	0.003	13.794	0.003	5.57	3.689	0.003	2.65	0.01	3.18	0.01
100	5.10	10.66	13.593	0.008	15.708	0.008	9.17	3.646	0.007	2.93	0.02	2.49	0.02
101	5.67	10.80	15.151	0.027	17.216	0.055	8.89	3.650	0.005	2.86	0.11	1.85	0.05
102	5.40	9.96	15.114	0.027	17.121	0.055	6.77	3.676	0.006	2.81	0.11	1.92	0.05
103	5.16	9.88	15.134	0.027	17.133	0.055	8.75	3.652	0.007	2.77	0.11	1.83	0.05
104	5.91	9.45	15.730	0.049	17.717	0.080	6.20	3.682	0.009	2.79	0.17	1.68	0.07
105	5.08	10.18	13.307	0.008	15.413	0.008	11.02	3.620	0.007	2.88	0.02	2.51	0.02
106	3.59	9.45	13.281	0.008	15.303	0.008	11.49	3.613	0.006	2.74	0.02	2.45	0.02
107	3.29	9.40	15.212	0.027	17.153	0.055	7.64	3.666	0.009	2.70	0.11	1.81	0.05
108	3.13	9.53	15.129	0.027	16.961	0.055	6.68	3.677	0.005	2.55	0.11	1.81	0.05
109	3.08	9.83	13.819	0.011	15.715	0.008	9.31	3.644	0.006	2.61	0.03	2.27	0.02
110	3.46	10.12	13.302	0.008	15.255	0.008	14.05	3.572	0.007	2.56	0.03	2.27	0.02
111	2.94	10.07	14.905	0.027	16.849	0.055	8.69	3.653	0.005	2.69	0.11	1.89	0.05
112	2.51	10.23	14.381	0.019	15.823	0.042	5.62	3.689	0.005	1.99	0.08	1.92	0.04
113	2.67	9.53	15.518	0.049	17.613	0.080	7.98	3.662	0.007	2.92	0.17	1.76	0.07
114	-4.86	12.72	15.647	0.042	17.899	0.224	7.68	3.665	0.007	3.16	0.41	1.82	0.16

ID	ΔRA ($''$)	ΔDec ($''$)	K (mag)	σ_K (mag)	H (mag)	σ_H (mag)	CO (%)	log $T_{\rm eff}$	$\sigma_{\log T_{eff}}$	A_K (mag)	σ_{A_K} (mag)	$\log(L/L_\odot)$	$\sigma_{\log(L/L_\odot)}$
115	-5.40	12.39	14.498	0.019	16.366	0.048	7.14	3.672	0.005	2.60	0.09	2.07	0.04
116	-6.18	12.69	15.679	0.042	17.406	0.072	6.76	3.676	0.005	2.40	0.15	1.53	0.06
117	-6.59	12.77	16.205	0.068	18.072	0.224	5.31	3.692	0.005	2.62	0.42	1.45	0.17
118	-6.78	12.66	16.404	0.119	18.180	0.224	6.30	3.681	0.008	2.48	0.45	1.28	0.19
119	-7.48	12.26	15.019	0.033	16.737	0.048	7.69	3.665	0.005	2.37	0.10	1.75	0.05
120	-7.70	12.45	15.224	0.033	16.988	0.053	6.94	3.674	0.005	2.45	0.11	1.73	0.05
121	-7.07	11.93	15.166	0.033	16.674	0.048	5.40	3.691	0.004	2.09	0.10	1.65	0.04
122	-6.86	11.85	15.556	0.042	17.281	0.072	6.11	3.683	0.004	2.40	0.15	1.60	0.06
123	-6.56	11.99	15.669	0.042	17.310	0.072	5.47	3.690	0.004	2.29	0.15	1.53	0.06
124	-6.21	12.10	15.638	0.042	17.358	0.072	6.14	3.683	0.006	2.40	0.15	1.56	0.06
125	-5.16	12.20	17.135	0.131	19.005	0.252	6.87	3.675	0.005	2.61	0.51	1.03	0.21
126	-4.89	12.12	15.325	0.042	17.257	0.072	5.98	3.685	0.005	2.71	0.15	1.82	0.06
127	-5.18	11.85	15.313	0.042	17.172	0.053	5.02	3.695	0.004	2.62	0.12	1.82	0.05
128	-5.83	11.56	14.756	0.033	16.508	0.048	7.64	3.666	0.004	2.42	0.10	1.88	0.05
129	-6.56	11.45	14.853	0.033	16.636	0.048	8.90	3.650	0.005	2.45	0.10	1.80	0.05
130	-7.21	11.53	13.517	0.008	15.305	0.010	9.99	3.635	0.005	2.43	0.02	2.29	0.02
131	-7.51	11.74	14.319	0.019	16.096	0.045	7.41	3.669	0.004	2.46	0.09	2.08	0.04
132	-7.75	11.58	15.081	0.033	16.952	0.053	8.21	3.659	0.007	2.59	0.11	1.80	0.05
133	-8.23	11.45	15.838	0.068	17.605	0.072	7.01	3.673	0.004	2.46	0.18	1.48	0.08
134	-8.29	11.12	15.889	0.068	17.677	0.072	6.84	3.675	0.004	2.49	0.18	1.48	0.08
135	-7.80	11.18	14.080	0.011	15.992	0.045	10.11	3.634	0.005	2.62	0.08	2.14	0.04
136	-7.70	10.83	15.377	0.042	17.235	0.053	6.32	3.681	0.005	2.60	0.12	1.74	0.05
137	-7.32	11.29	14.858	0.033	16.667	0.048	7.69	3.665	0.004	2.51	0.10	1.87	0.05
138	-7.07	10.85	15.836	0.068	17.186	0.053	5.97	3.685	0.006	1.85	0.15	1.27	0.07
139	-6.83	10.88	14.494	0.019	16.366	0.048	10.31	3.631	0.006	2.55	0.09	1.94	0.04
140	-7.02	10.53	14.002	0.011	16.085	0.045	9.61	3.641	0.005	2.88	0.08	2.29	0.04
141	-7.26	10.50	14.588	0.019	16.339	0.048	7.36	3.669	0.005	2.43	0.09	1.96	0.04
142	-5.99	11.18	11.861	0.003	13.400	0.002	10.47	3.628	0.005	2.06	0.01	2.79	0.01
143	-5.89	10.66	13.946	0.011	15.939	0.045	8.36	3.657	0.005	2.77	0.08	2.31	0.04
144	-5.45	10.31	15.461	0.042	17.386	0.072	5.11	3.694	0.004	2.71	0.15	1.79	0.06
145	-5.26	10.18	14.684	0.019	16.372	0.048	7.67	3.666	0.004	2.33	0.09	1.87	0.04
146	-4.86	9.85	12.872	0.004	14.806	0.007	10.37	3.630	0.005	2.64	0.02	2.62	0.01
147	4.94	16.85	15.552	0.033	17.771	0.193	8.39	3.657	0.007	3.10	0.35	1.80	0.14
148	4.18	16.82	14.313	0.014	16.510	0.043	9.01	3.649	0.006	3.06	0.08	2.26	0.04
149	3.51	16.69	15.608	0.033	17.420	0.058	7.22	3.671	0.005	2.52	0.12	1.59	0.05
150	5.94	16.58	15.878	0.073	18.001	0.193	5.31	3.692	0.005	3.00	0.37	1.74	0.15
151	5.83	16.28	15.617	0.033	17.657	0.058	7.14	3.672	0.006	2.86	0.12	1.72	0.05
152	5.59	16.09	15.837	0.073	17.933	0.193	6.11	3.683	0.005	2.95	0.37	1.71	0.15
153	4.97	16.42	12.691	0.003	15.117	0.005	14.50	3.564	0.006	3.24	0.02	2.76	0.02
154	4.32	16.28	16.030	0.073	18.088	0.193	6.94	3.674	0.008	2.89	0.37	1.58	0.15
155	2.73	16.60	15.914	0.073	17.716	0.058	5.83	3.686	0.008	2.52	0.17	1.51	0.08
156	2.84	16.25	13.465	0.007	15.255	0.007	8.70	3.653	0.006	2.46	0.02	2.37	0.02
157	3.00	15.98	15.508	0.033	17.399	0.058	4.92	3.696	0.006	2.66	0.12	1.76	0.05
158	3.35	15.90	15.638	0.033	17.629	0.058	7.04	3.673	0.005	2.79	0.12	1.69	0.05
159	3.73	15.96	15.501	0.033	17.434	0.058	6.61	3.678	0.006	2.71	0.12	1.73	0.05
160	4.67	15.93	15.194	0.026	17.162	0.046	6.63	3.678	0.004	2.76	0.09	1.87	0.04
161	5.32	15.77	15.439	0.033	17.512	0.058	7.90	3.663	0.005	2.89	0.12	1.78	0.05
162	5.43	15.88	15.235	0.026	17.402	0.058	9.64	3.640	0.005	3.00	0.11	1.85	0.05
163	5.78	15.80	15.236	0.026	17.399	0.058	8.57	3.654	0.007	3.01	0.11	1.89	0.05
164	5.83	15.52	15.698	0.033	18.004	0.193	8.79	3.651	0.006	3.22	0.35	1.78	0.14
165	5.99	15.58	16.165	0.073	18.239	0.193	6.62	3.678	0.008	2.91	0.37	1.54	0.15
166	5.08	15.50	16.363	0.076	18.561	0.216	8.51	3.655	0.006	3.07	0.41	1.46	0.17
167	4.99	15.15	15.308	0.033	17.408	0.058	10.85	3.623	0.007	2.88	0.12	1.72	0.05
168	3.81	15.31	12.615	0.003	14.638	0.005	13.49	3.581	0.007	2.68	0.02	2.61	0.02
169	3.38	15.31	15.383	0.033	17.319	0.058	8.35	3.657	0.006	2.68	0.12	1.71	0.05
170	3.16	15.15	14.040	0.008	16.061	0.043	9.34	3.644	0.006	2.79	0.08	2.25	0.04
171	2.92	15.66	15.052	0.026	16.976	0.046	8.92	3.650	0.008	2.66	0.09	1.81	0.05
172	2.78	15.34	14.778	0.026	16.934	0.046	9.07	3.648	0.005	3.00	0.09	2.05	0.04
173	2.54	14.80	13.166	0.004	14.934	0.005	5.00	3.695	0.005	2.48	0.01	2.62	0.01
174	3.21	14.42	15.317	0.033	17.176	0.046	6.99	3.674	0.006	2.59	0.10	1.74	0.05
175	3.24	14.66	15.590	0.033	17.545	0.058	7.46	3.668	0.006	2.73	0.12	1.67	0.05
176	3.62	14.80	15.449	0.033	17.362	0.058	9.52	3.642	0.005	2.63	0.12	1.61	0.05
177	4.10	14.88	15.905	0.073	18.090	0.193	7.66	3.666	0.005	3.06	0.37	1.67	0.15
178	6.10	15.07	15.197	0.026	17.898	0.193	10.05	3.634	0.006	3.78	0.35	2.16	0.14
179	5.75	14.50	10.803	0.002	13.327	0.002	16.04	3.536	0.007	3.31	0.02	3.49	0.02
180	4.56	14.23	12.404	0.003	15.485	0.007	14.27	3.568	0.007	4.22	0.02	3.28	0.02
181	4.00	14.28	15.637	0.033	17.484	0.058	4.80	3.697	0.003	2.60	0.12	1.69	0.05
182	3.89	13.77	12.332	0.003	14.286	0.005	12.22	3.602	0.007	2.62	0.02	2.75	0.02
183	3.67	14.09	15.154	0.026	17.022	0.046	9.60	3.641	0.005	2.56	0.09	1.70	0.04
184	3.21	13.47	13.180	0.004	15.232	0.005	11.63	3.611	0.007	2.78	0.02	2.50	0.02
185	3.00	14.09	15.071	0.026	17.010	0.046	7.33	3.670	0.005	2.70	0.09	1.88	0.04
186	2.46	13.45	15.667	0.033	17.564	0.058	7.33	3.670	0.005	2.64	0.12	1.61	0.05
187	4.75	13.82	15.838	0.073	17.896	0.193	7.32	3.670	0.004	2.88	0.37	1.64	0.15
188	5.35	13.53	15.493	0.033	18.000	0.193	9.48	3.642	0.009	3.51	0.35	1.95	0.14
189	5.21	13.01	13.400	0.007	15.575	0.007	11.59	3.612	0.006	2.97	0.02	2.49	0.02
190	4.86	13.04	15.419	0.033	17.675	0.058	4.92	3.696	0.005	3.20	0.12	2.01	0.05
191	4.62	13.28	15.571	0.033	17.613	0.058	7.31	3.670	0.005	2.86	0.12	1.74	0.05
192	4.29	13.42	15.229	0.026	17.173	0.046	7.96	3.662	0.007	2.70	0.09	1.79	0.04
193	4.13	13.18	15.177	0.026	17.135	0.046	5.54	3.690	0.006	2.76	0.09	1.91	0.04
194	3.81	12.96	14.855	0.026	17.095	0.046	7.21	3.671	0.005	3.15	0.09	2.14	0.04
195	3.75	12.82	14.958	0.026	16.816	0.046	6.62	3.678	0.006	2.59	0.09	1.90	0.04
196	3.46	12.18	14.986	0.026	16.925	0.046	7.58	3.667	0.007	2.70	0.09	1.90	0.04
197	4.62	12.31	14.028	0.008	16.714	0.043	11.82	3.608	0.007	3.72	0.08	2.53	0.04
198	4.67	11.96	15.444	0.033	17.517	0.058	8.54	3.655	0.011	2.88	0.12	1.76	0.06

ID	ΔRA ($''$)	ΔDec ($''$)	K (mag)	σ_K (mag)	H (mag)	σ_H (mag)	CO (%)	log $T_{\rm eff}$	$\sigma_{\log T_{eff}}$	A_K (mag)	σ_{A_K} (mag)	$\log(L/L_\odot)$	$\sigma_{\log(L/L_\odot)}$
199	5.48	12.34	14.066	0.008	16.048	0.043	9.55	3.641	0.009	2.73	0.08	2.21	0.04
200	5.75	11.96	15.084	0.026	18.396	0.216	10.30	3.631	0.010	4.68	0.39	2.55	0.16
201	5.83	12.50	15.007	0.026	16.824	0.046	7.83	3.664	0.007	2.52	0.09	1.81	0.04
202	5.56	12.80	15.206	0.026	17.276	0.058	7.35	3.669	0.009	2.90	0.11	1.90	0.05
203	5.32	12.64	15.004	0.026	16.793	0.046	7.93	3.662	0.006	2.47	0.09	1.79	0.04
204	17.98	18.79	13.875	0.008	15.987	0.041	12.13	3.603	0.006	2.86	0.08	2.23	0.03
205	17.42	18.66	12.761	0.005	14.750	0.005	7.67	3.665	0.004	2.77	0.01	2.82	0.01
206	16.96	18.36	15.226	0.021	17.257	0.058	8.52	3.655	0.005	2.82	0.11	1.82	0.05
207	16.63	18.68	14.970	0.021	16.876	0.048	8.24	3.658	0.005	2.64	0.09	1.86	0.04
208	16.42	18.63	15.582	0.027	17.474	0.058	6.17	3.683	0.004	2.65	0.11	1.69	0.05
209	16.42	18.39	15.578	0.027	17.470	0.058	8.39	3.657	0.007	2.62	0.11	1.60	0.05
210	15.55	18.36	15.736	0.027	17.868	0.202	6.30	3.681	0.006	3.00	0.36	1.76	0.15
211	15.47	18.68	16.367	0.083	18.105	0.202	5.70	3.688	0.004	2.43	0.39	1.30	0.16
212	15.39	19.06	16.023	0.061	17.959	0.202	3.62	3.708	0.004	2.74	0.38	1.62	0.15
213	15.15	18.58	14.538	0.015	16.357	0.047	7.22	3.671	0.004	2.53	0.09	2.02	0.04
214	14.61	18.50	15.400	0.027	17.426	0.058	7.51	3.667	0.008	2.83	0.11	1.79	0.05
215	14.61	18.04	12.841	0.005	14.809	0.006	5.63	3.689	0.003	2.77	0.01	2.85	0.01
216	15.07	18.09	15.299	0.027	17.248	0.048	6.82	3.675	0.006	2.73	0.10	1.81	0.04
217	15.61	17.90	15.055	0.021	16.851	0.048	4.29	3.702	0.003	2.53	0.09	1.90	0.04
218	15.82	17.93	15.329	0.027	17.293	0.058	5.46	3.690	0.004	2.76	0.11	1.86	0.05
219	16.09	18.01	15.249	0.021	17.087	0.048	7.03	3.673	0.004	2.56	0.09	1.76	0.04
220	16.36	17.82	16.300	0.083	18.281	0.204	8.44	3.656	0.006	2.75	0.39	1.36	0.16
221	16.96	17.98	13.942	0.008	15.841	0.041	9.37	3.644	0.004	2.61	0.07	2.22	0.03
222	17.60	18.09	15.513	0.027	17.565	0.058	9.45	3.643	0.006	2.83	0.11	1.67	0.05
223	17.12	17.74	14.996	0.021	16.761	0.048	8.00	3.661	0.004	2.44	0.09	1.78	0.04
224	16.98	17.58	13.668	0.005	15.518	0.007	9.04	3.648	0.004	2.54	0.02	2.31	0.01
225	16.52	17.55	15.812	0.061	18.124	0.202	5.87	3.686	0.004	3.28	0.38	1.85	0.15
226	16.31	17.28	14.495	0.015	16.480	0.047	9.03	3.648	0.004	2.74	0.09	2.06	0.04
227	15.74	17.39	15.275	0.027	17.219	0.048	6.77	3.676	0.006	2.72	0.10	1.82	0.04
228	15.34	17.39	15.470	0.027	17.529	0.058	6.90	3.675	0.005	2.89	0.11	1.80	0.05
229	15.42	16.98	16.262	0.083	18.066	0.202	6.45	3.680	0.007	2.52	0.39	1.35	0.16
230	15.34	16.71	15.123	0.021	17.461	0.058	6.69	3.677	0.005	3.30	0.11	2.12	0.05
231	15.93	16.71	13.527	0.005	15.422	0.007	10.90	3.622	0.006	2.57	0.02	2.31	0.02
232	16.44	17.15	13.639	0.005	15.636	0.007	10.57	3.627	0.005	2.73	0.02	2.34	0.02
233	16.98	17.17	14.927	0.021	16.440	0.047	7.26	3.670	0.004	2.07	0.09	1.68	0.04
234	17.25	17.04	15.273	0.027	17.212	0.048	8.20	3.659	0.006	2.69	0.10	1.76	0.04
235	17.39	17.20	14.481	0.015	16.331	0.047	8.79	3.651	0.005	2.55	0.09	2.00	0.04
236	17.77	16.69	14.440	0.015	16.309	0.047	7.90	3.663	0.007	2.59	0.09	2.06	0.04
237	17.31	16.69	15.226	0.021	16.971	0.048	4.79	3.697	0.004	2.45	0.09	1.79	0.04
238	16.98	16.77	16.383	0.083	18.381	0.204	6.51	3.679	0.008	2.80	0.39	1.42	0.16
239	17.52	16.07	15.026	0.021	16.916	0.048	10.57	3.627	0.009	2.57	0.09	1.72	0.05
240	17.31	15.71	13.073	0.005	15.095	0.006	10.61	3.626	0.005	2.77	0.02	2.58	0.02
241	16.39	15.63	15.333	0.027	17.192	0.048	6.66	3.677	0.005	2.59	0.10	1.75	0.04
242	16.12	15.42	14.285	0.015	16.163	0.041	8.51	3.655	0.008	2.59	0.08	2.10	0.04
243	16.04	15.77	15.011	0.021	16.470	0.047	4.92	3.696	0.004	2.02	0.09	1.70	0.04
244	15.28	15.47	15.066	0.021	16.950	0.048	6.97	3.674	0.005	2.63	0.09	1.86	0.04
245	15.31	16.09	15.352	0.027	17.243	0.048	6.55	3.679	0.007	2.64	0.10	1.76	0.05
246	15.50	16.42	15.382	0.027	17.339	0.058	7.03	3.673	0.004	2.73	0.11	1.77	0.05
247	15.12	16.36	14.726	0.015	16.606	0.047	10.30	3.631	0.006	2.56	0.09	1.85	0.04
248	18.71	13.90	14.621	0.016	17.520	0.065	11.38	3.615	0.005	4.04	0.12	2.44	0.05
249	18.58	13.80	13.958	0.009	15.403	0.009	6.33	3.681	0.004	1.99	0.02	2.07	0.02
250	17.87	13.93	14.910	0.027	16.616	0.044	4.50	3.700	0.004	2.39	0.09	1.90	0.04
251	16.98	13.61	14.856	0.027	17.116	0.055	8.54	3.655	0.004	3.16	0.11	2.10	0.05
252	16.17	13.66	16.296	0.100	18.025	0.198	5.75	3.687	0.006	2.41	0.39	1.32	0.16
253	15.93	13.45	15.774	0.064	17.581	0.065	5.53	3.690	0.007	2.53	0.16	1.58	0.07
254	16.33	13.23	14.934	0.027	16.765	0.055	6.30	3.681	0.004	2.56	0.11	1.90	0.05
255	16.60	13.45	16.083	0.064	18.269	0.233	4.92	3.696	0.003	3.10	0.43	1.70	0.17
256	16.90	13.45	15.023	0.027	16.766	0.055	6.39	3.680	0.004	2.43	0.11	1.81	0.05
257	17.09	13.18	15.868	0.064	17.650	0.065	5.28	3.692	0.006	2.50	0.16	1.54	0.07
258	17.28	13.18	14.923	0.027	16.713	0.044	6.56	3.678	0.004	2.49	0.09	1.88	0.04
259	17.55	13.31	15.131	0.027	16.904	0.055	7.08	3.672	0.005	2.46	0.11	1.76	0.05
260	18.14	13.58	15.066	0.027	16.834	0.055	7.71	3.665	0.004	2.45	0.11	1.76	0.05
261	18.31	13.50	15.182	0.027	16.984	0.055	7.14	3.672	0.004	2.50	0.11	1.76	0.05
262	18.90	13.20	11.054	0.002	12.618	0.002	11.69	3.610	0.005	2.06	0.01	3.06	0.01
263	18.50	12.58	14.975	0.027	16.649	0.044	7.40	3.669	0.005	2.31	0.09	1.75	0.04
264	18.31	12.28	12.522	0.003	14.414	0.005	10.74	3.624	0.004	2.57	0.01	2.72	0.01
265	18.71	12.26	15.774	0.064	17.527	0.065	5.80	3.687	0.005	2.45	0.16	1.54	0.07
266	19.17	12.18	12.940	0.005	14.683	0.005	11.04	3.620	0.007	2.34	0.02	2.45	0.02
267	17.87	12.64	15.189	0.027	17.110	0.055	7.94	3.662	0.005	2.67	0.11	1.79	0.05
268	17.74	12.26	13.417	0.008	15.210	0.006	9.23	3.646	0.004	2.46	0.02	2.37	0.01
269	17.15	12.18	16.087	0.064	18.519	0.233	6.83	3.675	0.006	3.44	0.43	1.78	0.17
270	16.98	12.31	15.043	0.027	16.845	0.055	8.59	3.654	0.003	2.48	0.11	1.75	0.05
271	16.69	12.18	12.248	0.003	14.120	0.003	12.93	3.591	0.006	2.48	0.02	2.70	0.02
272	16.77	12.99	14.951	0.027	16.704	0.044	6.96	3.674	0.003	2.43	0.09	1.83	0.04
273	16.39	12.61	12.552	0.003	14.315	0.005	4.08	3.704	0.002	2.48	0.01	2.89	0.01
274	15.55	13.10	15.324	0.039	17.308	0.065	4.81	3.697	0.003	2.80	0.13	1.89	0.06
275	15.42	12.50	14.718	0.016	16.613	0.044	6.34	3.681	0.003	2.65	0.08	2.03	0.03
276	15.96	12.23	13.624	0.008	15.550	0.009	8.26	3.658	0.004	2.67	0.02	2.41	0.01
277	15.47	11.77	15.327	0.039	17.333	0.065	4.94	3.696	0.005	2.83	0.13	1.90	0.06
278	15.50	11.56	15.479	0.039	17.545	0.065	6.01	3.684	0.008	2.91	0.14	1.84	0.06
279	15.85	11.34	13.934	0.009	15.885	0.045	7.63	3.666	0.006	2.72	0.08	2.32	0.04
280	16.01	11.15	15.087	0.027	17.174	0.055	9.49	3.642	0.008	2.89	0.11	1.86	0.05
281	15.82	11.10	15.398	0.039	17.480	0.065	6.14	3.683	0.005	2.93	0.13	1.87	0.06
282	16.50	11.58	15.047	0.027	16.877	0.055	8.00	3.661	0.010	2.53	0.11	1.79	0.05

ID	ΔRA ($''$)	ΔDec ($''$)	K (mag)	σ_K (mag)	H (mag)	σ_H (mag)	CO (%)	log $T_{\rm eff}$	$\sigma_{\log T_{eff}}$	A_K (mag)	σ_{A_K} (mag)	$\log(L/L_\odot)$	$\sigma_{\log(L/L_\odot)}$
283	16.74	11.58	14.931	0.027	16.922	0.055	8.07	3.661	0.009	2.77	0.11	1.93	0.05
284	16.71	11.31	15.040	0.027	17.024	0.055	9.80	3.638	0.005	2.73	0.11	1.81	0.05
285	16.71	10.99	15.251	0.039	17.147	0.055	10.42	3.629	0.009	2.58	0.12	1.64	0.06
286	16.96	10.66	16.019	0.064	17.658	0.065	5.89	3.686	0.006	2.28	0.16	1.37	0.07
287	17.17	11.20	15.337	0.039	17.459	0.065	8.96	3.649	0.007	2.95	0.14	1.81	0.06
288	17.20	11.58	15.334	0.039	17.229	0.055	5.43	3.691	0.005	2.66	0.12	1.81	0.05
289	17.58	11.29	15.161	0.027	17.013	0.055	4.87	3.696	0.002	2.61	0.11	1.88	0.05
290	18.28	11.50	15.082	0.027	16.835	0.055	6.09	3.684	0.005	2.44	0.11	1.81	0.05
291	18.33	11.69	15.143	0.027	16.849	0.055	5.51	3.690	0.004	2.38	0.11	1.78	0.05
292	18.06	10.77	14.916	0.027	16.814	0.055	10.69	3.625	0.008	2.58	0.11	1.76	0.05
293	17.77	10.75	14.598	0.016	16.558	0.044	11.05	3.620	0.005	2.66	0.08	1.91	0.04
294	17.63	10.34	15.301	0.039	17.319	0.065	8.23	3.659	0.007	2.81	0.14	1.79	0.06
295	-6.67	18.85	14.814	0.014	16.883	0.042	10.09	3.634	0.007	2.85	0.08	1.93	0.04
296	-7.51	19.31	15.600	0.029	17.609	0.051	4.45	3.700	0.004	2.84	0.11	1.81	0.05
297	-7.70	19.12	15.219	0.014	17.213	0.042	5.71	3.688	0.004	2.81	0.08	1.91	0.03
298	-8.29	19.01	14.783	0.014	16.753	0.042	8.22	3.659	0.005	2.74	0.08	1.97	0.03
299	-8.37	18.82	15.067	0.014	16.961	0.042	5.94	3.685	0.003	2.66	0.08	1.90	0.03
300	-9.15	18.74	11.437	0.002	13.493	0.002	8.46	3.656	0.003	2.86	0.01	3.35	0.01
301	-8.26	18.23	14.468	0.011	16.434	0.044	9.28	3.645	0.004	2.71	0.08	2.05	0.03
302	-6.72	18.14	13.651	0.005	15.524	0.007	9.17	3.646	0.004	2.58	0.02	2.33	0.01
303	-7.07	17.77	15.142	0.014	17.064	0.042	7.86	3.663	0.007	2.67	0.08	1.82	0.04
304	-8.13	17.63	15.598	0.029	17.594	0.051	5.03	3.695	0.004	2.82	0.11	1.78	0.05
305	-8.48	17.74	15.391	0.029	17.322	0.051	7.87	3.663	0.005	2.68	0.11	1.72	0.05
306	-8.72	17.63	15.467	0.029	17.360	0.051	7.25	3.670	0.004	2.64	0.11	1.69	0.05
307	-9.94	17.90	15.508	0.029	17.631	0.051	10.16	3.633	0.006	2.93	0.11	1.69	0.05
308	-10.07	17.28	15.566	0.029	17.617	0.051	7.43	3.668	0.006	2.87	0.11	1.74	0.05
309	-10.12	17.50	15.794	0.060	17.879	0.196	5.97	3.685	0.007	2.94	0.36	1.72	0.15
310	-8.88	17.28	15.160	0.014	17.095	0.042	8.64	3.653	0.005	2.68	0.08	1.78	0.03
311	-8.80	17.15	15.482	0.029	17.506	0.051	9.00	3.649	0.007	2.80	0.11	1.69	0.05
312	-8.56	17.31	15.606	0.029	17.457	0.051	8.29	3.658	0.004	2.56	0.11	1.57	0.05
313	-8.05	16.98	15.477	0.029	17.505	0.051	7.95	3.662	0.006	2.83	0.11	1.74	0.05
314	-6.94	17.12	15.234	0.014	17.284	0.051	9.04	3.648	0.007	2.84	0.10	1.80	0.04
315	-6.59	16.98	15.524	0.029	17.516	0.051	5.68	3.688	0.005	2.80	0.11	1.79	0.05
316	-6.86	16.71	15.647	0.029	17.546	0.051	6.88	3.675	0.004	2.65	0.11	1.64	0.05
317	-6.94	16.58	15.254	0.029	17.181	0.042	6.51	3.679	0.003	2.70	0.09	1.83	0.04
318	-7.64	16.39	15.395	0.029	17.375	0.051	8.66	3.653	0.007	2.74	0.11	1.72	0.05
319	-6.61	15.77	14.757	0.014	16.307	0.044	10.12	3.633	0.006	2.08	0.08	1.65	0.04
320	-7.48	15.36	15.453	0.029	17.392	0.051	8.26	3.658	0.005	2.69	0.11	1.68	0.05
321	-7.75	15.55	13.625	0.005	15.630	0.007	10.90	3.622	0.007	2.73	0.02	2.33	0.02
322	-8.34	16.52	13.477	0.005	15.438	0.007	8.02	3.661	0.004	2.73	0.02	2.50	0.01
323	-8.96	16.96	14.418	0.011	16.562	0.044	9.48	3.642	0.005	2.97	0.08	2.17	0.04
324	-9.10	16.79	13.835	0.008	15.898	0.039	10.18	3.633	0.005	2.84	0.07	2.32	0.03
325	-8.53	15.66	12.615	0.003	14.755	0.006	9.82	3.638	0.005	2.96	0.01	2.87	0.02
326	-8.59	15.34	13.698	0.005	15.683	0.007	10.55	3.627	0.005	2.71	0.02	2.31	0.01
327	-9.05	15.28	12.764	0.004	14.750	0.005	9.86	3.637	0.006	2.73	0.02	2.72	0.02
328	-9.18	15.85	15.145	0.014	17.151	0.042	6.83	3.675	0.004	2.81	0.08	1.90	0.03
329	-9.99	15.98	14.581	0.011	16.522	0.044	5.01	3.695	0.004	2.73	0.08	2.16	0.03

2.3.2 Observed Hertzsprung-Russell Diagram

The GC H-R diagram is shown in Figure 2.7. Our data clearly show the red clump at $\log(L/L_\odot) \sim 1.7$, as well as the upper red giant branch / early asymptotic giant branch. There is an indication of the AGB bump at $\log(L/L_\odot) \sim 2.3$, and we also detect some lower red giant branch stars at lower luminosities, though the observations are highly incomplete in this region. The data set in Figure 2.7 allows for a more robust analysis of the Galactic Center star formation history than any other previously published data set. Photometric studies are limited to the modeling of luminosities alone (Rieke 1987; Narayanan et al. 1996; Davidge et al. 1997; Philipp et al. 1999; Alexander & Sternberg 1999; Figer et al. 2004), due to intrinsic variations in late-type giant colors and the large variation in Galactic Center extinction. This point is illustrated in Figure 2.8, which compares the observed H-R diagram to a color-magnitude diagram (CMD) for the same GC stars. The RGB/AGB and RC populations are more clearly distinguished in the H-R diagram than in the CMD, and there is less scatter in $T_{\rm eff}$than $H-K$, due to variations in GC extinction. As a result, only the K-band luminosity function can reliably be modeled with broadband photometry alone.

The observed H-R diagram in this study is also an improvement with respect to previous spectroscopic work (Blum et al. 1996b, 2003), due to our improved magnitude limit (∼5 mag. deeper), which allows for the analysis of well-populated regions in the H-R diagram, in which the evolutionary models are fairly well understood.

The errors in temperature and luminosity are shown with the data in grey in Figure 2.7. Average errors in temperature and luminosity for stars with luminosities $1.6 < \log(L/L_{\odot}) < 2.0$ (the red clump region) are shown at right. The temperature limit for the minimum CO index and the 50% completeness limit for the average extinction correction ($A_K = 2.75$ mag.) are also shown. Solar metallicity (in red, left) and metal-poor (Z=0.008, in blue, right) isochrones from Girardi et al. (2000) are overplotted. The isochrones show the wide range of ages spanned by the Galactic Center population. Figure 2.7 also demonstrates the age-metallicity degeneracy inherent in this part of the diagram. Stars in the same part of the H-R diagram may represent a metal-rich, intermediate-age ($\lesssim$ a few Gyr) population or a metal-poor, old ($\gtrsim$ 5 Gyr) population. For stars younger than ∼5 Gyr, the Galactic Center stellar population is known to be approximately solar (Ramírez et al. 2000; Carr et al. 2000). For older stars, the Galactic Center metallicity distribution is not well-known. We will address this uncertainty later in the paper.

2.3.3 Deriving the Star Formation History

To investigate the star formation history implied by our sample, we begin with a qualitative discussion, followed by quantitative analysis in §3.4-3.5. We start by considering three models based on candidate star formation histories presented in the literature. The first scenario consists of an ancient burst of star formation 7.5-8.5 Gyr ago, similar to the single stellar population of the bulge. Genzel et al. (2003) compared this scenario to the K band luminosity function (KLF) of the inner parsec. The second model consists of constant star formation between 10 Myr and 10 Gyr ago. This model is based on the best-fit model of Figer et al. (2004), who considered the Galactic Center KLF within 40 pc of the center. The third model corresponds to the best-fit star formation history of Blum et al. (2003), who fit the H-R diagram of asymptotic giant branch and cool supergiant stars within the central 5 pc, using four specified age bins. All models are summarized in Table 2.3.

For each scenario, we generated model H-R diagrams using the synthetic color-magnitude diagram computation algorithm IAC-Star (Aparicio & Gallart 2004). The algorithm uses a Monte Carlo approach to compute composite stellar populations on a star-by-star basis, using a specified set of evolutionary tracks. The code accommodates several additional inputs, including the initial mass function, star formation rate function, and chemical enrichment law. To compare the generated models to the data, we added Gaussian noise based on the average observed errors in luminosity and temperature. We also randomly removed stars from the models according to our estimated spectroscopic completeness (Fig 2.6).

The models are shown against our Galactic Center sample in Figure 2.9. A qualitative comparison suggests that the ancient burst model is insufficient to fully describe the observed data set. The continuous star formation model and the Blum et al. (2003) model span the full

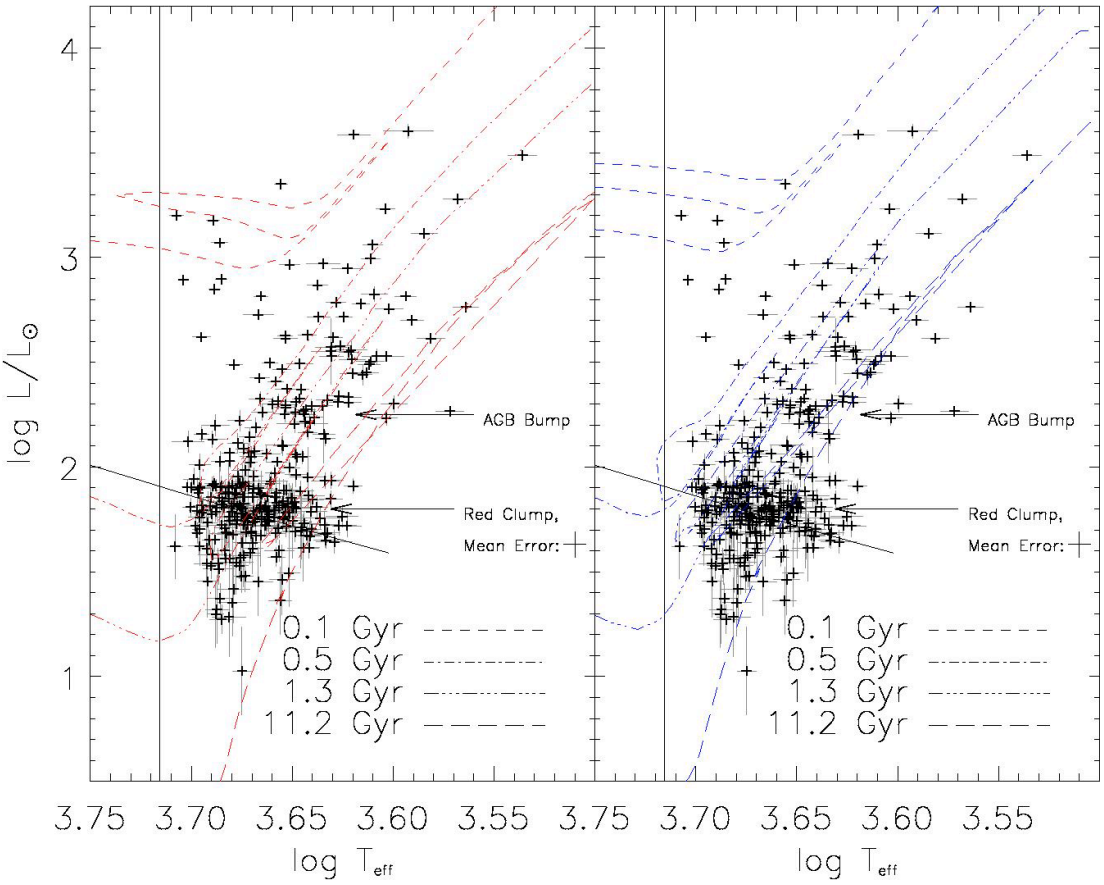

Figure 2.7 H-R diagram for the GC stars with solar-metallicity (in red, left) and metal-poor (Z=0.008, in blue, right) isochrones from Girardi et al. (2000) overplotted. The magnitude limit for 50% completeness (see Figure 2.6) and the temperature limit for which stars no longer show CO (see Figure 2.4) are overplotted as solid dark lines. Errors are shown in grey. The mean errors in temperature and luminosity for stars with luminosities $1.6 < \log(L/L_{\odot}) < 2.0$ (the red clump region) are shown at right.

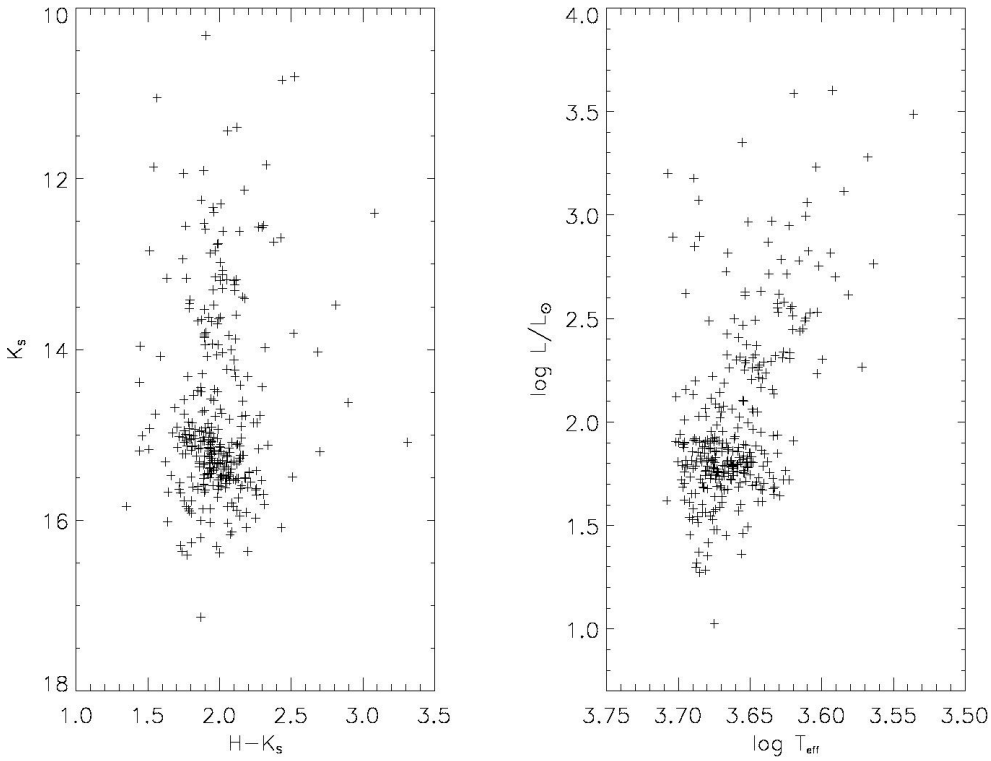

Figure 2.8 Comparison of the observed GC H-R diagram to a color-magntidue diagram for the same GC stars. The figure demonstrates the advantange of the spectroscopic temperature derivation. The RGB/AGB and RC populations are more clearly distinguished in the H-R diagram than in the CMD, and there is less scatter in T_{eff}than $H-K$, due to variations in GC extinction.

Table 2.3. Summary of star formation history models

Model	Description	Age (Gyr)	Z	IMF Slope	M_{lower} ($M_\odot$)	M_{upper} ($M_\odot$)	χ^2_λ [a]	P_λ [b] (%)	Relative SFR[c]	σ_{SFR} [d]
1	Bulge-like	7.50 - 8.50	0.015	2.35	0.7	120	3228.8	0.00	1.00	-
2	Continuous	0.01 - 10.0	0.019	2.35	0.7	120	404.9	3.76	1.00	-
3	Blum et al.	0.01 - 0.10	0.019	2.35	0.7	120	678.8	0.01	0.65	-
		0.10 - 1.00	0.019	2.35	0.7	120			0.06	-
		1.00 - 5.00	0.019	2.35	0.7	120			0.09	-
		5.00 - 12.0	0.019	2.35	0.7	120			0.21	-
4	Two-bin, solar	0.01 - 5.00	0.019	2.35	0.7	120	384.5	3.03	0.82	0.04
		5.00 - 12.0	0.019	2.35	0.7	120			0.18	0.07
5	Two-bin, solar	0.01 - 7.00	0.019	2.35	0.7	120	270.0	16.66	0.90	0.04
		7.00 - 12.0	0.019	2.35	0.7	120			0.10	0.09
6	Two-bin, poor	0.01 - 5.00	0.019	2.35	0.7	120	450.0	0.68	0.91	0.05
		5.00 - 12.0	0.008	2.35	0.7	120			0.09	0.08
7	Closed-box	0.01 - 12.0	0.004 - 0.019	2.35	0.7	120	1035.6	0.00	1.00	-
8	Flat IMF	0.01 - 12.0	0.019	0.85	0.7	120	242.8	39.70	1.00	-
9	High M_{lower}	0.01 - 12.0	0.019	2.35	2.5	120	4201.8	0.00	1.00	-
10	High M_{lower}	0.01 - 12.0	0.019	2.35	1.5	120	551.4	0.00	1.00	-
11	Model 5+8 Hybrid	0.01 - 7.00	0.019	0.85	0.7	120	257.0	26.3	0.48	0.02
		7.00 - 12.0	0.019	0.85	0.7	120			0.51	0.20

[a] Poisson likelihood parameter: $\chi^2_\lambda = 2\sum_i m_i - n_i + n_i \ln \frac{n_i}{m_i}$; n_i is the number of observed stars and m_i is the number of model stars in bin i.

[b] Goodness of Fit Parameter: Percentage of Monte Carlo trials in which synthetic data sets composed of stars drawn from the best-fit models have larger χ^2_λ than the χ^2_λ implied by the observed data set. If the model is an accurate representation of the true star formation history, this percentage should be approximately 50%.

[c] Average relative star formation rate for each age bin specified in the third column. The rates are normalized such that the total relative star formation rate is 1.

[d] Uncertainty in the relative star formation rate, derived by fitting the star formation history to a series of synthetic data sets consisting of stars drawn from the observed data set.

range in temperature and luminosity of the observed data set but seem to have relatively too many stars at cool temperatures. It is unlikely this observed effect is caused by systematic errors or a selection bias. A systematic underestimate of the GC CO indices would shift the pattern to hotter temperatures. However, the red edge of the Hertzsprung gap (log $T_{\rm eff} \sim$ 3.70) is well matched by the models, making such a systematic effect unlikely. In addition, some cool RGB/AGB stars are present in the data, while a systematic shift to warmer temperatures would allow none. Finally, the brightness and CO strength of cool RGB/AGB stars compared to warmer, dimmer red clump stars means that cool RGB/AGB stars are relatively easy to detect and classify. There is no obvious way of selectively removing these stars from the sample.

Motivated by the comparison in Figure 2.9, we consider three alternative scenarios that could potentially explain the relative paucity of stars at low temperatures:

1. The first and simplest possibility is that the star formation rate was low at early times ($\gtrsim$ 5 Gyr). To test this hypothesis, we generated two models consisting of linear combinations of constant star formation in two specified age bins (Models 4 and 5 in Table 2.3). Model 4 assumes bins of 0.01-5 Gyr and 5-12 Gyr. Model 5 assumes bins of 0.01-7 Gyr and 7-12 Gyr.

2. A second possibility is that the oldest stars are metal poor. The previously described models assume a solar metallicity for all times. This assumption is motivated by

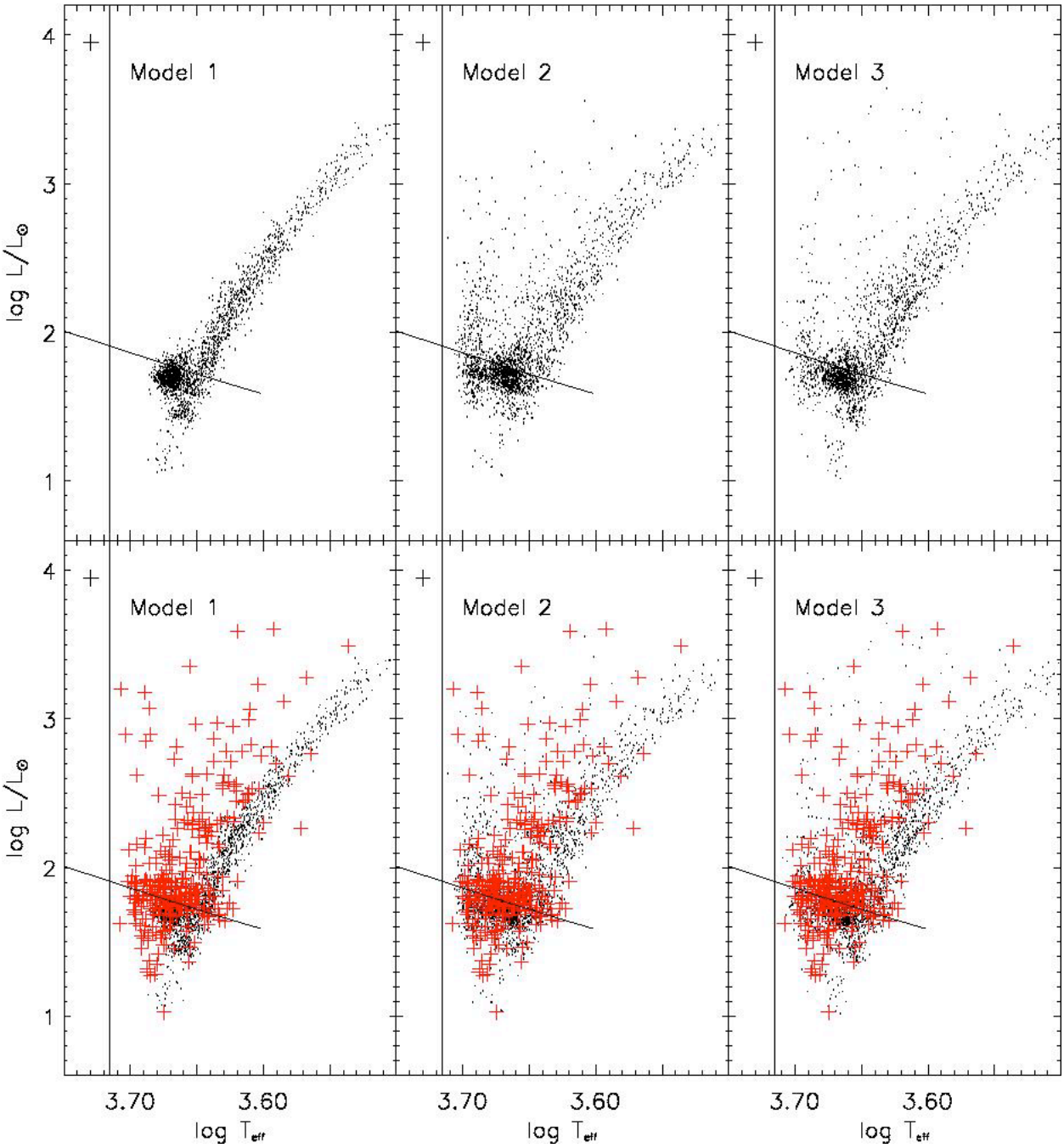

Figure 2.9 Comparison of the observed data (red crosses) to several proposed models given in the literature (black dots). See the text and Table 2.3 for a description of the models. We have added noise to the models based on the average observed errors in luminosity and temperature (upper left). We also corrected for the incompleteness function of the data (Fig 2.6). A qualitative comparison suggests that all literature models produce relatively too many cool stars to describe the observed data set.

the work of Ramírez et al. (2000), who found the stellar [Fe/H] abundance to be approximately solar for stars younger than ∼5 Gyr. For older stars, the Galactic Center metallicity distribution has not been determined. However, the bulge, which formed 7-12 Gyr ago, is known to have a nearly solar distribution (Sadler et al. 1996). An extremely metal poor ancient population would, therefore, represent a completely separate population from the bulge. Given the current observed differences between the bulge and the nucleus discussed in §1, we can not exclude this possibility. We, therefore, generated two models to represent this scenario. The first model, Model 6, consists of a linear combination of constant star formation in two age bins with solar metallicity for 0.01-5 Gyr and a metallicity of 0.008 for 5-12 Gyr. The second model, Model 7, is a simple closed box model assuming constant star formation for 0.01-12 Gyr, a starting metallicity of 0.004 and an ending metallicity of solar.

3. A final way to explain the relative lack of stars at cool temperatures invokes a non-standard initial mass function (IMF). In all above models, we assume a Salpeter IMF with an upper mass limit of 120 $M_{\odot}$ and a lower mass limit of 0.7 $M_{\odot}$. As stars less massive than $\sim 0.7 M_{\odot}$ have main sequence lifetimes comparable to the age of the Universe, we are not sensitive to stars below this mass limit. Recent results indicate that the current initial mass function of the Galactic Center is flatter than a Salpeter function or has an unusally high lower mass cut-off (Nayakshin & Sunyaev 2005; Paumard et al. 2006). Such a mass function could explain the relative lack of low mass stars in the observed old stellar population. To test this hypothesis, we consider three models, all assuming continuous star formation at solar metallicity for 0.01-12 Gyr. The first model, Model 8, assumes a flat single power-law slope ($dN/dm = m^{-0.85}$), chosen to match the results of Paumard et al. (2006). Models 9 and 10 both assume a standard Salpeter slope ($dN/dm = m^{-2.35}$), but with lower mass limits of 2.5 $M_{\odot}$ and 1.5 $M_{\odot}$, respectively.

Results stemming from these three hypotheses are tested in §3.5.

2.3.4 Quantification of Fit

To quantitatively compare the models described above to the data, we adopted the numerical techniques described in Dolphin (2002). We first binned the observed and model H-R diagrams in temperature and luminosity for stars above our 50% completeness threshold, using uniform bins with size three times our average errors ($\delta \log(L/L_{\odot}) = 0.12$, $\delta \log T_{eff} = 0.018$). The choice of bins in this technique is somewhat subjective. However, tests using different bins sizes showed that while the binning scheme does change the fit quality, it does not significantly affect the derived star formation rates. This finding is in agreement with Dolphin (2002).

For models with two age bins, we used the Numerical Recipes procedure AMOEBA (Press et al. 1992) to search for the linear combination of models that minimized the Poisson

maximum likelihood parameter: $\chi^2_\lambda = 2\sum_i m_i - n_i + n_i \ln \frac{n_i}{m_i}$ (Dolphin 1997). Here, n_i is the number of observed stars and m_i is the number of model stars in bin i. For models with fixed relative star formation rates, we scaled the model distribution to minimize χ^2_λ. To estimate the errors in the derived star formation history, we implemented the technique described in Blum et al. (2003). We built a set of 100 H-R diagrams consisting of a random sampling of 329 stars drawn from the observed H-R diagram, allowing each observed star to be selected any number of times. We then re-derived the star formation history for each H-R diagram and given model. The resulting standard deviation in the derived star formation rate was taken as the 1σ uncertainty.

We measured the fit quality through a second set of Monte Carlo simulations. In this set, we generated 10,000 synthetic data sets drawn from the fitted models, selecting 329 stars randomly for each trial and re-deriving the star formation history for the selected subset. For a model that is an accurate representation of the true star formation history, χ^2_λ derived from the actual data set should be comparable to χ^2_λ derived from a typical synthetic data set. Therefore, to establish the goodness of fit, we calculated the percentage of trials, P_λ, in which χ^2_λ was larger when fitting the synthetic data sets to the models than when fitting the true data sample to the models. If the model is a good representation of the true star formation history, P_λ should be approximately 50%.

2.3.5 Model Results

The results of all model fits are listed in Table 2.3. Hess diagrams showing the difference between the observed data histogram and the best-fit model histograms are shown in Figure 2.10. White indicates regions where the model produces too many stars relative to the observed data set, and black indicates regions where the model produces too few stars relative to the observed data set. Examination of the P_λ values in Table 2.3 confirms the qualitative result discussed in §3.3 that no literature model (Models 1-3) is a likely description of the observed data set. This result is also reflected in the first three panels in Figure 2.10, which show white diagonal streaks, corresponding to the overdensity of cool stars in the models relative to the data.

Table 2.3 also suggests that the early-history low star formation rate models (Models 4 and 5) are unlikely representations of the data, though Model 5 returns a considerably better fit, and we are unable to completely exclude this model. However, examination of the fourth and fifth panels in Figure 2.10 show that both models systematically overpredict the number of cool stars, as in Models 1-3. The early-history low metallicity models (Models 6 and 7) also show systematic deficiencies when compared to the data. Both models predict a red clump / horizontal branch morphology that is too blue compared to the observed distribution. Similar discrepencies between the models and data are present in the high IMF mass limit models (Models 9 and 10). Each predicts a hotter and more luminous red clump than is observed. However, while Models 9 and 10 predict no old, cool stars, the flat IMF model (Model 8) predicts few old, cool stars, in good agreement with the observations. Model 8 also gives a satisfactory goodness of fit ($P_\lambda = 40\%$) suggesting that this model is a

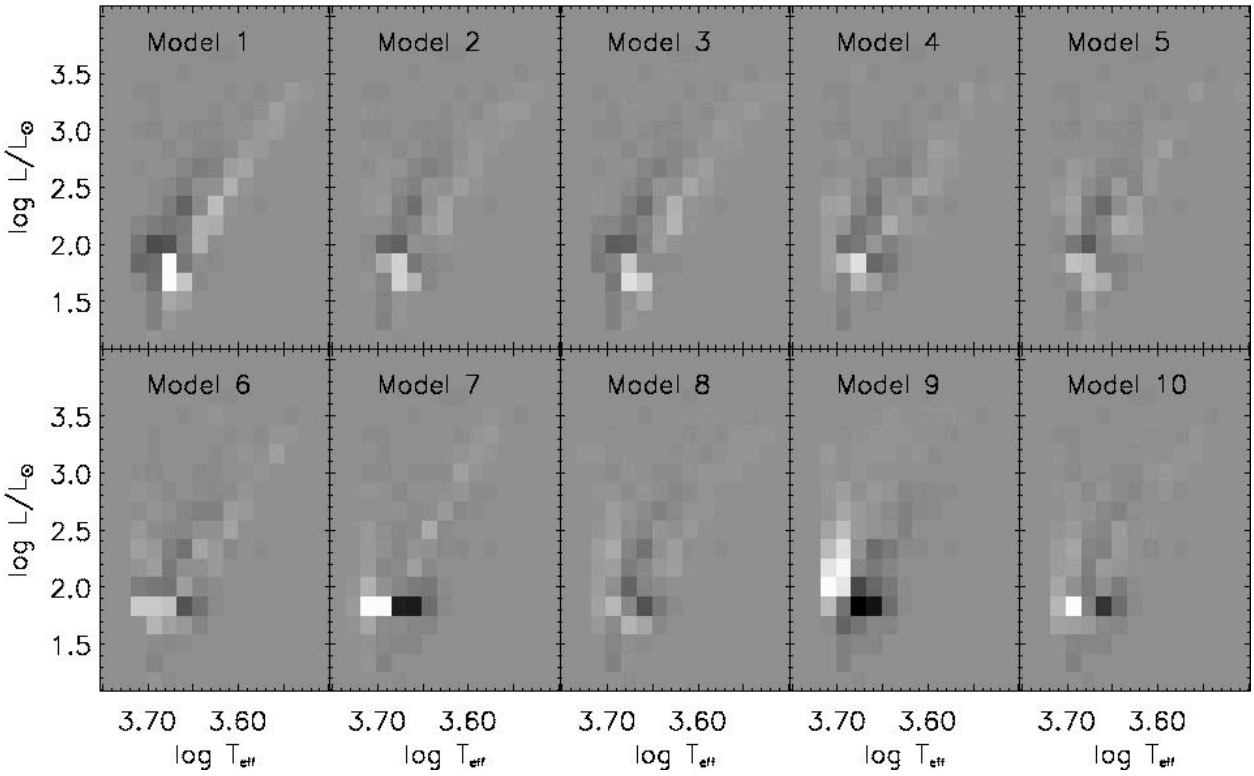

Figure 2.10 Hess diagrams showing the difference between the observed data histogram and the best-fit model histograms summarized in Table 2.3. White indicates regions where the model produces too many stars relative to the observed data set, and black indicates regions where the model produces too few stars relative to the observed data set. The first three panels correspond to models proposed in the literature and described in the text. All show white diagonal streaks, corresponding to the overdensity of cool stars in the models relative to the data. The early-history low star formation rate models (Models 4 and 5) suffer similar systematic deficiencies. The early-history low metallicity models (Models 6 and 7) predict a red clump / horizontal branch morphology that is too blue compared to the observed distribution. The high IMF mass limit models (Models 9 and 10) predict a hotter and more luminous red clump than is observed. The flat IMF model (Model 8) corresponds to the best fit and shows minimal systematic trends compared to the other models.

likely representation of the observed distribution.

Using the models listed in Table 2.3, we tested for population differences as a function of distance from the cluster center. Such differences within the central 1-2 pc are expected due to mass segregation, and several broadband photometry studies have found indications of such an effect (Philipp et al. 1999; Genzel et al. 2003; Schödel et al. 2007). To test for this effect in our data, we separated the data into two sets containing the four innermost ($4'' - 15''$, $11''$ median) and outermost ($13'' - 26''$, $20''$ median) spectral regions shown in Figure 2.1. We then refit the two best-fit models (Models 5 and 8) to each subset, applying the average errors and completeness specific to that subset. This process returned fits for each subset that are consistent with those obtained for the entire data set. In particular, the subset P_λ values were within 10% of that obtained for the entire data set, and the relative star formation rates returned by both subsets for Model 5 were within 1σ of the rates returned by the entire data set. We therefore, find no significant evidence in our data for a population gradient. This result is not that surprising, as the broadband photometry results of Schödel et al. (2007) suggest that variations in the cool, low-mass stellar population within the central parsec should be most evident 3-7 arcsec from Sgr A*. Our sample is outside of the region expected to exhibit the largest population differences (see Figure 2.1). In the future, the technique we describe could be applied to regions closer to Sgr A*, although limited spectroscopic completeness due to increased stellar density would complicate such a study. Still, a thorough spectroscopic study of the red-clump and RGB/AGB populations as a function of distance from Sgr A* could provide the first definitive test of mass segregation within the central parsec (Alexander 2005).

With the restriction to simple models, the top-heavy IMF model appears to be superior to the remaining three model families we consider (low star formation rate (SFR) at early times, low metallicity at early times, IMF with high lower mass limit). The low-SFR, low-Z, and high M_{lower} families all show consistent systematic deficiencies when compared to the data. It is, therefore, unlikely one could slightly change the chosen parameters (i.e. precise metallicity, age bin cut-offs, mass ranges, etc.) within these families to produce a model that is an adequate description of the data.

2.4 Discussion

Of the models considered in Table 2.3, Model 8 (continuous star formation at solar metallicity with a top-heavy IMF) fits the observations best, and our Monte Carlo tests show that it is a reasonable description of the data. Based on the goodness of fit, we cannot completely exclude Model 5. However, as discussed in the previous section, this model shows systematic deviations from the data; we, therefore, favor Model 8. We note that Model 8 is probably not the only possible description of the data with this degree of likelihood. All models so far discussed assume a simplistic description of the GC star formation history, and there are likely more complicated scenarios that also adequately describe the data. For instance, an additional model with age bins identical to Model 5 and an IMF slope identical

to Model 8 yields a reasonable fit ($\chi^2_\lambda = 257.0$, $P_\lambda = 26.3\%$). However, we do not feel that increasing the number of free parameters is justified, given the limits, uncertainties, and size of our data set.

In the context of our current knowledge about the Galactic Center, continuous star formation with a top-heavy IMF is reasonable. At present, there is substantial evidence for stars in the Galactic nucleus spanning a wide range of ages, based on results from broadband photometry, and several distinct age tracers, including supergiants, AGB stars, and OH/IR stars (see §1). The present distribution and kinematics of gas in the inner Galaxy is also consistent with continuous star formation (Morris & Serabyn 1996).

In addition, the most recent epoch of star formation in the Galactic Center is likely represented by a top-heavy initial mass function (Nayakshin & Sunyaev 2005; Paumard et al. 2006). If this recent epoch of star formation is not anomolous and periodic bursts of GC star formation have occurred throughout the history of the Galaxy, there is no a priori reason to believe the GC IMF would change with time. The present data set appears to support this picture. We note that the mass traced by giants in the Central Cluster is primarily set by the initial mass formed, rather than dynamical effects, since mass segregation is expected to only strongly affect the central $\sim$0.01 pc of the Galactic Center (Hopman & Alexander 2006; Freitag et al. 2006). On the 1-2 pc scale studied in this paper, the efficiency of mass segregation is thought to be much lower, in agreement with observational photometry results (Genzel et al. 2003; Schödel et al. 2007).

Though our findings are broadly consistent with several stellar population studies of the Galactic Center and the nucleus at large, there remains some disagreement. In particular, our results are somewhat different from those presented in Blum et al. (2003), who probed the central 5 pc and used supergiants and bright AGB stars to quantify the star formation history in a method very similar to that employed here. Using their observed H-R diagram, Blum et al. (2003) argued for variable star formation over a wide range of ages, with the majority of stars formed more than 5 Gyr ago at solar metallicity. We find a much smaller fraction of our sample is represented by solar-metallicity low-mass stars with ages $\gtrsim$ 5 Gyr.

The present work and the work of Blum et al. (2003) study different regions in the H-R diagram. Each regime has relative advantages and disadvantages for studying the GC star formation history, and we discuss each in turn:

1. *Field of View*: Due to the rarity of supergiants and bright AGB stars in the Galactic Center, Blum et al. (2003) probed all late-type stars above their magnitude limit for the entire Central Cluster (r $<$ 2.5 pc). They, therefore, derived absolute star formation rates and were able to compare the cluster mass implied to estimates from dynamical studies. In contrast, our study probes a relatively small region on the sky ($\sim$0.2 pc^2 within r $<$ 1.0 pc). As such, our results are somewhat susceptible to population inhomogeneities in the Central Cluster, and we are able to derive only relative star formation rates.

2. *Stellar Crowding*: Spectral extraction from our SINFONI fields is complicated by stellar crowding. While we took care to ensure that our derived CO indices are largely

independent of exact pixel and background selection, contamination by neighboring stellar spectra remains a source of uncertainty for many of the dim stars. The stars studied by Blum et al. (2003), on the other hand, are well separated from each other. In addition, the GC AGBs and supergiants are much brighter than neighboring stars, so there is negligible uncertainty in the Blum et al. (2003) spectra due to crowding.

3. *Spectral Classification*: The spectral classification method presented by Blum et al. (2003) is very similar to that presented here. Our depper study has the advantage that only giants are observed, and thus, a separate luminosity class determination is not required. Additionally, the stars we study are warmer than those studied by Blum et al. (2003), and thus, our CO-$T_{\rm eff}$relationship is tighter than theirs, due to reduced uncertainties in model atmosphere spectra at warmer temperatures (Reid & Hawley 2000). We further note that the derived temperatures for the red supergiants in the work of Blum et al. (2003) are likely systematically too cool, as Levesque et al. (2005) recently showed that red supergiants are $\sim$400 K warmer than previously thought.

4. *Adequacy of Stellar Evolution Models*: The evolutionary models in the part of the H-R diagram probed by our study (red clump, red giant branch, early AGB) are much less uncertain than the part of the H-R diagram studied by Blum et al. (2003) (supergiants, TP-AGBs). Gallart et al. (2005) review the adequacy of AGB stellar evolution models for deriving star formation histories, concluding that the observed bright AGB populations are often more sensitive to poorly known modeling parameters than the star formation history. The input physics for the late AGB stages is not well determined (e.g. mass loss, convection, efficiency of the third dredge-up), and currently, only the Padova libraries include these stages (Girardi et al. 2000). While uncertainties in mass loss and convection are also present for the red clump, RGB, and early AGB, the input physics for these stages is much better understood, and a number of stellar evolution models including these phases have been compared and tested against observations. For this reason, we believe our star formation history fit is more reliable than that presented in Blum et al. (2003). Finally, our data set also has the benefit that it contains several evolutionary features (red clump, AGB bump) that are cleraly distinguishable from surrounding regions in the H-R diagram. The diagram morphology assures us that no large systematic effects are present in the data and allows us to construct physically motivated models. The region of the H-R diagram studied by Blum et al. (2003) has no such morphological features.

While we believe that our results are more robust than those presented in Blum et al. (2003), we also note that the findings are not necessarily in conflict. The region probed by Blum et al. (2003) extends to $\sim$2.5 pc from the center, whereas we probe only the central parsec. Furthermore, we note that there are some similarities in our findings. Both studies find evidence for star formation throughout the history of the Galaxy, and both studies suggest that purely solar metallicity models are needed to produce the observed data. Still, further work is needed to resolve the remaining discrepencies (i.e., variable versus continuous

star formation, Salpeter versus flat IMF). Specifically, a sample tracing a large region on the sky and containing thousands of stars would represent a significant step forward in this field. The planned FLAMINGOS-2 GC Survey on Gemini (Eikenberry et al. 2006) will obtain 4000 late-type giant spectra out to one degree in Galacto-centric radius ($\sim$140 pc) and with a spectral resolution of R$\sim$20,000. It will, therefore, provide unprecedented information on the Galactic Center chemical enrichment and star formation history.

2.5 Summary and Conclusion

We observed 329 late-type giants $4'' - 26''$ north of Sgr A* with the integral field spectrometer SINFONI on the VLT. Combining spectral classifications with NaCo photometry, we derived luminosities and effective temperatures for these stars. Due to the improved magnitude limit of our sample relative to previous work, our derived H-R diagram clearly shows the red clump, as well as the red giant branch and asymptotic giant branch. Using a maximum likelihood analysis, we compared the observed distribution to models representing ten possible star formation histories. The best-fit model corresponds to continuous star formation over the last 12 Gyr with a top-heavy IMF. The similarity of this result to the IMF observed for the most recent epoch of star formation is intriguing and perhaps suggests a connection between recent star formation and the stars formed throughout the history of the Galactic Center. The upcoming FLAMINGOS-2 GC Survey on Gemini will provide important information needed to further understand this suggestive result.

Chapter 3

The M Dwarf GJ 436 and its Neptune-Mass Planet

Abstract

We determine stellar parameters for the M dwarf GJ 436 that hosts a Neptune-mass planet. We employ primarily spectral modeling at low and high resolution, examining the agreement between model and observed optical spectra of five comparison stars of type, M0-M3. Modeling high resolution optical spectra suffers from uncertainties in TiO transitions, affecting the predicted strengths of both atomic and molecular lines in M dwarfs. The determination of $T_{\rm eff}$, gravity, and metallicity from optical spectra remains at $\sim$10%. As molecules provide opacity both in lines and as an effective continuum, determing molecular transition parameters remains a challenge facing models such as the PHOENIX series, best verified with high resolution and spectrophotometric spectra. Our analysis of GJ 436 yields an effective temperature of $T_{\rm eff}$ = 3350 $\pm$ 300 K and a mass of 0.44 $M_{\odot}$. New Doppler measurements for GJ 436 with a precision of 3 m s^{-1} taken during 6 years improve the Keplerian model of the planet, giving a minimum mass, $M \sin i$ = 0.0713 $M_{\rm JUP}$ = 22.6 $M_{\rm Earth}$, period, P = 2.6439 d, and e = 0.16$\pm$0.02. The noncircular orbit contrasts with the tidally circularized orbits of all close-in exoplanets, implying either ongoing pumping of eccentricity by a more distant companion, or a higher Q value for this low-mass planet. The velocities indeed reveal a long term trend, indicating a possible distant companion.

3.1 Introduction

To date, radial velocity surveys have revealed three exoplanetary systems with M dwarf hosts: GJ 876, GJ 436, and GJ 581 (Rivera et al. 2005; Butler et al. 2004; Bonfils et al. 2005b). Remarkably, all three of these M dwarfs host planets with minimum masses ($M \sin i$) less than 0.1 $M_{\rm JUP}$, ranking them among the lowest mass exoplanets known. Microlensing

surveys have strengthened the case for the preferntial occurence of such "super-Earths" around M dwarfs. Current results suggest four M dwarf systems, with two harboring planets in the super-Earth mass range (Beaulieu et al. 2006; Gould et al. 2006; Bond et al. 2004; Udalski et al. 2005). Given detection biases against the discovery of low mass planets, all these findings imply that super-Earths are more common close companions to M dwarfs than gas giants (Endl et al. 2006; Beaulieu et al. 2006). The frequency of longer period planets remains poorly constrained.

From a theoretical viewpoint, the growth of planets around low mass stars has been explored only recently. Low mass stars likely form by accretion at the centers of protoplanetary disks having lower mass than those surrounding solar mass stars. Such low mass disks may spawn low mass planets, both because of less available mass and because of shorter survival times for the disks (Laughlin et al 2004). However, core accretion models of giant planet formation that include growth of a rocky core from dust particles followed by the gravitational accretion of gas suggest that giant planets may have enough time to form. Solutions to the time scale competition between planet growth and disk lifetime have been proposed by invoking both migration to move the planet to gas-rich areas and also by adopting lower opacities to allow faster accretion of the envelope onto the core (Hubickyj et al. 2004, Alibert et al. 2005). Nonetheless, rocky cores that are starved of gas may instead become ice giants similar to Neptune and Uranus (Goldreich et al. 2004, Thommes et al. 2002, Ida & Lin 2005). Under the core accretion paradigm, it remains unknown how commonly planets fail to accrete gas after successful growth of a rock and ice core, thereby leaving behind a super-Earth planet. Most recently, Boss (2006) provided a very different viable alternative to the core accretion scenario, showing that disk instability can also be invoked to explain current M dwarf observations. Distinguishing between these competing models of planet formation requires more observational results.

To further understanding in this area, we present a follow-up study of GJ 436, an M dwarf recently discovered to host a Neptune-mass planet ($M \sin i = 0.066$ M_{JUP} ; Butler et al. 2004). At present, little is known about this system. As there is no other giant planet within a few AU of the host star, a larger planet cannot easily be invoked to explain a curtailed accretion of gas of the known planet, hereafter GJ 436b. Furthermore, since the stellar luminosity and mass are not well known, the planet's minimum mass and predicted temperature are poorly constrained. To better characterize this system, we have obtained new Doppler measurements and attempted to deduce accurate stellar parameters. In §2, we discuss photometric observations leading to estimates of the stellar mass and luminosity. In §3, we present an effort to determine the effective temperature, surface gravity, and metallicity of GJ 436 via low and high resolution spectral modeling. In §4, new Doppler measurements are presented, leading to an improved orbit and minimum mass for the planet. In §5 and 6, we discuss the implications of our results.

3.2 Photometric Observations and Analysis

We first assess the stellar properties of GJ 436 using photometric measurements and published calibrations. We use optical and near-infrared photometry for GJ 436 taken from the compilation by Leggett (1992). The quoted values are V = 10.66, I = 8.28, J = 6.93, H = 6.34, and K = 6.10. We adopt the Hipparcos parallax for GJ 436 of 97.73 mas (Perryman et al. 1997).

3.2.1 Stellar Mass

We estimate the mass of GJ 436 from various empirical mass-luminosity relations (MLRs) and theoretical models for M dwarfs. Delfosse et al. (2000) have determined empirical MLRs for visual and near-infrared magnitudes using their newly discovered M dwarf binaries. With these relations, the V, J, H, and K band photometry from Leggett (1992) yield inferred masses for GJ 436 of 0.418, 0.439, 0.441, and 0.442 $M_{\odot}$, respectively. Thus, the JHK photometric calibrations all yield a stellar mass of $M_{\star} = 0.44 \pm 0.04$ $M_{\odot}$. We adopt an accuracy of $\sim$10% in stellar mass from the scatter in the calibrations of Delfosse et al. (2000). The V band estimate of 0.418 $M_{\odot}$ is lower than the mass derived from the the JHK calibration, but the V-band calibration has more scatter. Moreover, the particular metallicity of GJ 436 will affect the mass estimate from the V band more than from the IR bands. As metallicity remains somewhat uncertain (§3), we give more weight to the mass from the near-IR calibrations.

For comparison, the mass estimates derived from both the empirical relations of Henry & McCarthy (1993) and Benedict et al. (2001) agree within 10% of 0.44 $M_{\odot}$. The theoretical models of Baraffe et al. (1998) and Siess et al. (2000) applied to GJ 436 also yield masses that are in agreement at the 10% level, though the theoretical relation between mass and optical flux has a strong metallicity dependence. Here, we adopt the mass derived from the near-infrared relations of Delfosse et al. (2000), giving $M_{\star} = 0.44 \pm 0.04$ $M_{\odot}$. This value is 7.3% higher than that adopted by Butler et al. (2004), who gave more weight to the mass derived from the various V band calibrations.

3.2.2 Stellar Luminosity

Extensive observational analyses of M dwarf luminosities have been performed by Leggett et al. (1996), who derived luminosities for 16 M dwarfs by combining spectrophotometry and broadband measurements over the wavelength range, 0.35 to 5 μm. Reid & Hawley (2000) have fit second-order polynomials to the derived bolometric corrections of Leggett et al. (1996) in the V, I, and K bands. Employing these relations for GJ 436 yields implied luminosities of 0.024, 0.024, and 0.025 $L_{\odot}$, respectively.

These estimates are in good agreement with those derived from the tight empirical relation between M_K and M_{BOL} of Veeder (1974). The observed relations for luminosity are also in agreement with those from theoretical models constructed by Baraffe et al. (1998),

Siess et al. (2000), and D'Antona & Mazzitelli (1994). Here, we assume the simple average of the derived luminosities quoted above: $L = 0.024 \pm 0.004 L_{\odot}$, slightly lower than the value, L=0.025 $L_{\odot}$, that was found by Butler et al. (2004).

3.3 Spectral Modeling

3.3.1 Model Atmospheres

To constrain the effective temperature, metallicity, and surface gravity of GJ 436, we compared observed spectra obtained at both low and high resolution to synthetic spectra. We used an updated grid of the NEXTGEN set of M dwarf models (Hauschildt et al. 1999) that includes an updated molecular line list, a revised treatment of dust grain formation, and a treatment of spherical geometry. A detailed description of the model atmospheres used in calculating the synthetic spectra presented here can be found in Allard et al. (2001).

3.3.2 High Resolution Modeling

We obtained high resolution (R $\sim$ 60,000) echelle spectra for GJ 436 and five comparison M dwarfs (GJ 411, GJ 424, GJ 752A, GJ 860 A, and GJ 908) using the Keck 1 telescope with the HIRES spectrometer between June 1997 and November 2001. The wavelength range was 3700-6200 Å, contained in 33 spectral orders. Only spectra at wavelengths greater than 5203 Å were used in spectral modeling. The standard planet-hunting procedure for reduction of the raw echelle images was employed to perform flat-fielding, sky subtraction, order extraction, and wavelength calibration (Butler et al. 1996; Vogt et al. 1994). All spectral modeling was performed on template spectra not containing iodine.

To compare the observations to the models, several adjustments were made to the continuum and wavelength scale of the observed spectra. The pseudo-continuum levels of the M dwarf spectra consist of overlapping molecular bands, and the echelle spectra are not flux calibrated. To bring the models and the observed spectra to the same continuum value, we fit a second degree polynomial to the points of highest flux across each echelle order and also to the corresponding wavelength section of the model spectrum. We then divided by these pseudo-continuum polynomials to obtain normalized fluxes for both observed and synthetic spectra. We next degraded the resolution of the model spectra to match the observed resolution by convolving each model spectrum with a Gaussian of the appropriate width. It was not necessary to modify the models further to correct for rotational line broadening, as none of the stars in our sample have significant rotation, having $V \sin i < 3$ km s^{-1} (Delfosse et al. 1998). Finally, we removed the stellar Doppler shift from the observed spectra by cross-correlating the observed and model spectra and shifting the observed spectra by the appropriate amount.

Comparing observed to synthetic spectra constitutes a standard approach in determining M dwarf stellar parameters (Jones et al. 1994; Leggett et al. 1996; Valenti et al. 1998; Basri et

al. 2000; Leggett et al. 2000, 2001, 2002; Kirkpatrick et al. 1993; Bean et al. 2006). However, deducing characteristics of early type M dwarfs using high resolution spectral modeling has been performed rarely and has revealed uncertainties with the molecular constants (Valenti et al. 1998). To derive characteristics of GJ 436 from high resolution spectral modeling, we therefore tested the integrity of our model fits by tests on other early type M dwarfs. The comparison M dwarfs were selected to encompass the range of early spectral types and metallicities near GJ 436.

The results of our high resolution modeling of GJ 436 are summarized in Figure 3.1, showing overplotted synthetic and observed spectra for a representative portion of one echelle order. Figure 3.1 demonstrates that the model TiO lines, constituting a pseudo-continuous opacity for M dwarfs in the optical, do not match the observed molecular lines. This discrepency was observed in all orders and for all M dwarfs in our sample. The specific wavelengths and pattern of wavelengths of the observed TiO lines is so different from those in the synthetic spectrum that no association of the two sets of TiO lines was possible. The apparent flaws in the molecular constants for TiO are reminiscent of those described for TiO by Valenti et al. (1998) in their high resolution spectra of M dwarfs. Apparently, the treatment of TiO at high resolution remains inadequate. We, therefore, decided that only the atomic lines could be used in modeling the observed echelle spectra.

With this limitation, the observed echelle spectra were compared to the model spectra in two ways. First, we examined each spectral order by eye against the model spectra, concentrating on the depths and wings of atomic lines, identified using a solar atlas. We monitored, but gave little weight to, the average strengths of the molecular lines. We considered only the strong atomic lines with equivalent widths greater than 0.1 Å, which suffer little contamination from any blended TiO lines. Second, we performed a least squares fit to the strong atomic lines (giving no weight to the TiO lines). We extracted a small segment of spectrum centered on each atomic line extending three line widths on both sides of line center. In some cases, the observed atomic lines were significantly blended with molecular lines. These lines were not included in the least squares fit. To avoid unphysical results due to degeneracy in the three free parameters (temperature, metallicity, and surface gravity), we fixed the metallicities of our sample stars to match the results of Bonfils et al. (2005a) listed in Table 1. These metallicities were in all cases consistent with our classifications by eye.

Table 3.2 lists the derived temperatures from the spectral modeling for the six M dwarfs examined here. The first and second columns give the star name and spectral type. The fourth and fifth columns list our derived values of $T_{\rm eff}$ from the high resolution spectra found by eye and by least squares fitting, respectively. For all stars but one (GJ 424), the estimates by eye are within 60 K of the results derived by least squares fitting, suggesting that our two fitting procedures are self-consistent. For GJ 424, the two methods gave $T_{\rm eff}$ different by 150 K. We note that the temperatures derived were nearly the same among all echelle orders fitted for a given star, also suggesting self-consistency.

The top panel in Figure 3.1 shows the best fit to GJ 436 for the high resolution modeling ($T_{\rm eff}$ = 3200 K, log g = 4.0, [M/H] = 0.0), obtained both by least squares fitting and by

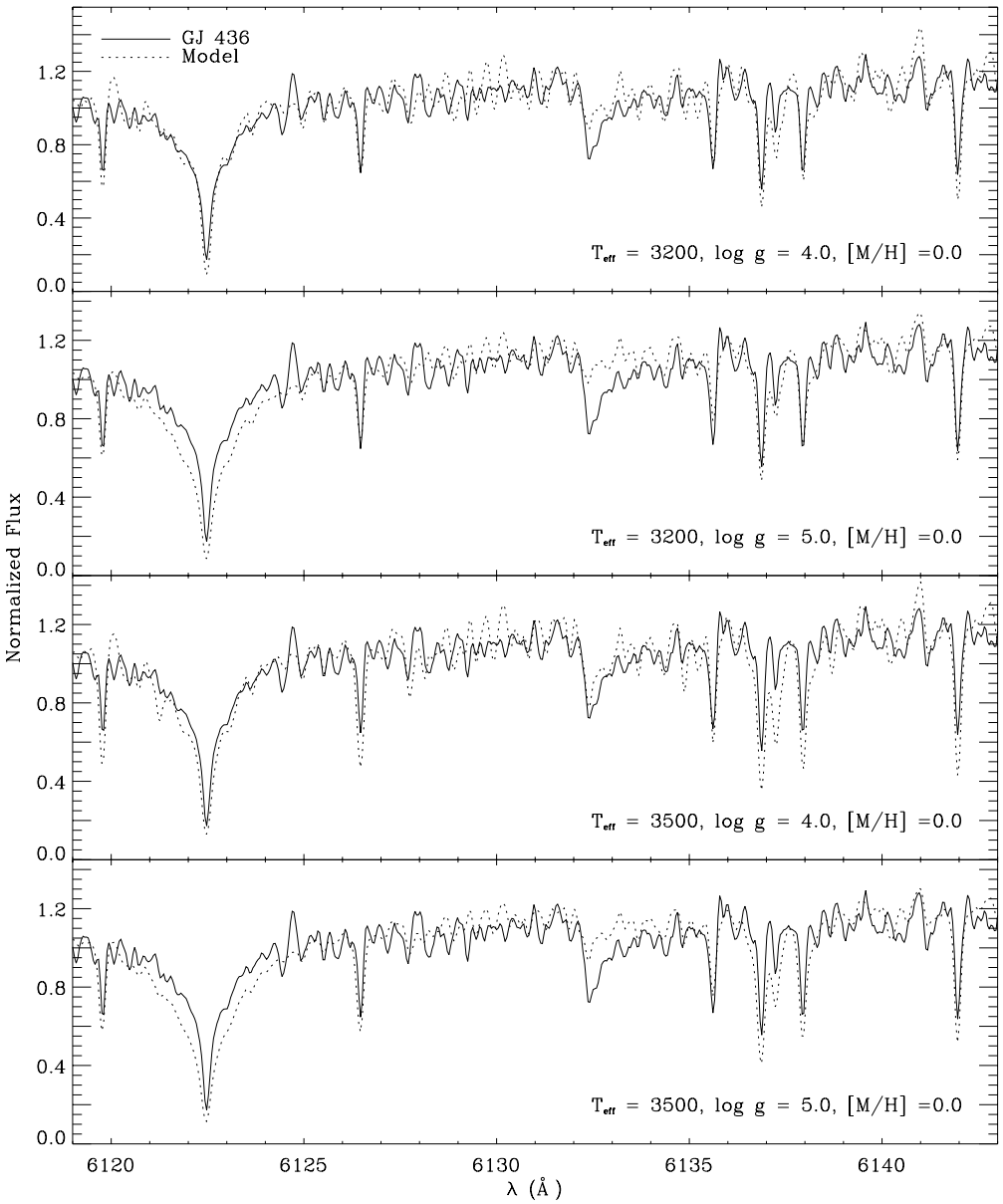

Figure 3.1 Comparison at high resolution of the high resolution best fit and the low resolution best fit for GJ 436. The figures show a representative portion of one echelle order; notice that in all figures, the model TiO molecular lines do not match the observed lines. The top panel shows the best fit at this resolution. However, while the atomic line profiles are well fit, and the overall strength of the TiO lines is similar, the surface gravity for this model is unphysical (see the text). When the surface gravity is fixed to a reasonable value (panels 2 and 4), the overall strength of the molecular lines and the atomic line profiles can not be simultaneously matched.

Table 3.1. Metallicities reported by Bonfils et al. 2005a

Star	[M/H]
GJ 436	-0.03
GJ 411	-0.42
GJ 424	-0.48
GJ 752A	-0.05
GJ 860A	-0.02
GJ 908	-0.53

Table 3.2. Summary of effective temperature results

Object	Spec. T.	T_{eff} Low res. (K)	T_{eff} Echelle by eye (K)	T_{eff} Echelle num. (K)	T_{eff} Echelle log g = 5.0, fixed (K)
GJ 436	M2.5	3500	3200	3200	3400
GJ 411	M2	>3500, 3500, 4000*	3400	3370	3630
GJ 424	M0	-	3400	3550	3830
GJ 752A	M2.5	-	3300	3240	3430
GJ 860A	M3	-	3200	3140	3380
GJ 908	M1	3700+	3500	3530	3790

*Derived by Kirkpatrick (1993), Leggett et al. (1996), and Jones et al. (1996), respectively.

+Derived by Leggett et al. (1996)

Table 3.3. Summary of surface gravity results

Object	Spec. T.	log g Low res. (dex)	log g Echelle (by eye) (dex)	log g Echelle (num.) (dex)
GJ 436	M2.5	5.0	4.0	4.0
GJ 411	M2	5.0*	4.5	4.3
GJ 424	M0	-	4.0	4.2
GJ 752A	M2.5	-	4.5	4.0
GJ 860A	M3	-	4.0	4.0
GJ 908	M1	-	4.5	4.4

*Derived by Jones et al. (1996)

eye. The observed and synthetic atomic line depths are similar in this model, and the overall strength of the molecular lines match well. But note that the TiO lines that pervade the spectrum do not correspond in detail, as discussed above. The Lorentzian line wings of the Ca I line at 6122 Å are also well matched. However, while the best fit model spectrum appears to match the observed atomic lines and the strength of the molecular lines, the surface gravity derived is significantly lower than the known surface gravities of M dwarfs, log g $\sim$ 4.75. This underestimate of surface gravity was consistently observed in high resolution modeling of all the M dwarfs in our sample, if we let log g float. Columns 4 and 5 of Table 3.3 demonstrate this bias towards low surface gravities, showing that in all cases the best fit to surface gravity yielded log g $\leq$ 4.5.

To investigate this discrepancy in gravity further, we fixed the surface gravity in our high resolution modeling to higher, and more likely, values than those that appear to best fit the models. Both log g = 4.5 and log g = 5.0 were tested. The second and fourth panels in Figure 3.1 display representative results obtained from this test with surface gravity fixed to log g = 5.0. The strengths of the atomic lines are well-matched in the second panel, notably those between 6135 and 6143 Å. However, the Lorentzian line wings of the Ca I line at 6122 Å are too pronounced. The overall strength of the TiO lines also appear too weak in this model, though this discrepency is more pronounced in other echelle orders. Similar results were observed for all stars in our sample. Specifically, for realistic values of surface gravity, we were unable to find models that simultaneously matched the observed atomic line profiles and the overall strength of the TiO lines.

We believe this anomaly is due to inaccuracy in the continuous opacity of the models. For M dwarfs observed in the optical, the dominant source of continuous opacity is TiO. Problems due to treatment of TiO are immediately seen in the lack of agreement between

the resolved lines in the observed and model spectra. The pattern of model and observed TiO lines do not agree, suggesting significant errors in the model of the TiO energy levels, as noted previously by Valenti et al. (1998). Moreover, TiO molecules, in their role as an effective continuous opacity source, affect the predicted atomic line depths. Increased continuous opacity causes the $\tau = 2/3$ surface of the star to reside higher in the star's atmosphere where the temperature is lower. In the LTE interpretation, the source function is the Planck function, which is lower due to the lower temperature. The atomic lines form in a similarly cool region and are thus less deep relative to the continuum.

However, increasing the surface gravity is degenerate with increasing the continuous opacity, as larger gravity results in a larger TiO abundance. This effect is seen in the model spectra. Increasing the assumed surface gravity reduces the model atomic line depths (e.g. see panels 1 and 2 or 3 and 4 of Figure 3.1). Therefore, if the amount of continuous opacity in the models is effectively too high, the surface gravity need not be as high in order for the atomic line depths to match. As a result, the best fit surface gravities will be too low. This effect may explain the modeling bias towards low surface gravities discussed above.

In addition, we note that if the derived surface gravities are in error, the derived effective temperatures will also be in error (Buzzoni et al. 2001). For medium-high resolution spectral modeling, Buzzoni et al. (2001) have quantified the coupling between errors in derived surface gravity and those in effective temperature:

$$\frac{\Delta \log g}{\Delta T_{\rm eff}} = 1.3 \left(\frac{1000}{T_{\rm eff}} \right)^4 {\rm dex\,K^{-1}}$$

According to this relation, a decrease in surface gravity of $\sim$1.0 dex will lead to a decrease in effective temperature for early-type M dwarfs of $\sim$100 K. Applying this result to our high resolution modeling results and assuming a gravity deficiency of $\Delta \log g \sim 1.0$ dex leads to an adjusted effective temperature of $T_{\rm eff} \sim 3300$ K for GJ 436. This result is in agreement with the effective temperature derived with surface gravity fixed to log g = 5.0 dex; in that case, we found $T_{\rm eff} \sim 3400$ K (see column 6 of Table 3.2).

3.3.3 Low Resolution Modeling

We also modeled a low resolution red spectrum of GJ 436 kindly provided by D. Kirkpatrick. This spectrum was taken on 3 December 1995 using the red channel of the double spectrograph with the 158 line mm^{-1} grating on the Hale 5 m telescope with an integration time of 5 sec. It extends from 5140-9176 Å and the resolution is $R = 1140$, corresponding to an instrumental profile having a FWHM of 7 Å. To compare the observed spectrum to the models, the spectra were cross-correlated and matched in resolution in the same way as was done for the high resolution spectra. Because the individual molecular lines are not resolved at this resolution, the full spectrum was used in the fit.

The low resolution modeling of GJ 436 yielded $T_{\rm eff} = 3500$ K, log g = 5.0, and [M/H] = 0.0. This result is somewhat different from the result obtained from our high resolution

spectrum that gave T_{eff} = 3200 K, log g = 4.0, and [M/H] = 0.0. Figure 3.2 provides a comparison at low resolution of the best fit high resolution model to the best fit low resolution model. The discrepency between the results obtained at high resolution versus low resolution is not surprising, as the high resolution modeling is sensitive to strengths of the atomic lines, which are influenced by the oscillator strengths of the TiO lines. In contrast, the low resolution modeling is sensitive to the shape of the continuum dictated by the gross structure of the TiO bands. It is interesting to note that for the three stars in our sample that have been modeled at low resolution (GJ 436, GJ 411, and GJ 908), the derived effective temperatures are consistently higher than those derived at high resolution when surface gravity is left as a free parameter. On the other hand, when surface gravity is fixed to a reasonable value of log g = 5.0, the high and low resolution results come into good agreement (see Table 3.2).

However, due to the inaccuracies in the TiO line list revealed by the high resolution spectra, it is likely that the continua in the model spectra carry significant errors at both low and high resolution. Therefore, while the fits at low and high resolution come into good agreement when the surface gravities are fixed to the same value, the derived parameters may still be systematically in error. For future work in this area, an important distinction between modeling at high resolution versus that at low resolution is that at high resolution, errors in the continuous opacity due to the poorly determined TiO lines can be directly observed in the TiO lines themselves. At low resolution, errors in the TiO opacity are not as directly obvious. High resolution observational spectra are therefore required to test new models that incorporate adjustments to the molecular continuous opacity. We note that while the current TiO line list and corresponding oscillator strengths have been adjusted and improved in the last decade, molecular opacities remain the primary source of uncertainty in model synthetic spectra of M dwarf atmospheres (Valenti et al. 1998, Allard et al. 2000, Bean et al. 2006). The accuracy of derived parameters at the moment appears to be largely dependent on the observed spectral region. Valenti et al. (1998) and Bean et al. (2006), for example, have improved portions of the M dwarf models by deriving wavelengths and oscillator strengths of the TiO lines from the M dwarfs themselves. As a result of this effort, Bean et al. (2006) showed that careful treatment of specific TiO bandheads can lead to improved synthesis of the spectra of those lines. However, in the absence of observations containing these carefully tuned regions, stellar parameters derived directly from synthetic spectra remain highly uncertain. The TiO opacities for the PHOENIX models continue to be revised and tested, and improved opacities will likely be incorporated into the next set of available grids (Allard et al., in prep). It would be valuable if these new grids were tested using a sizable sample of M dwarf spectra at high resolution, as it is likely that uncertainties in the TiO opacity have led to biases in the currently-accepted M dwarf temperature scale. For the present purposes of characterizing GJ 436, however, we tentatively assign an effective temperature that is the simple average of our low and high resolution results: $T_{eff} \sim 3350 \pm 300$ K.

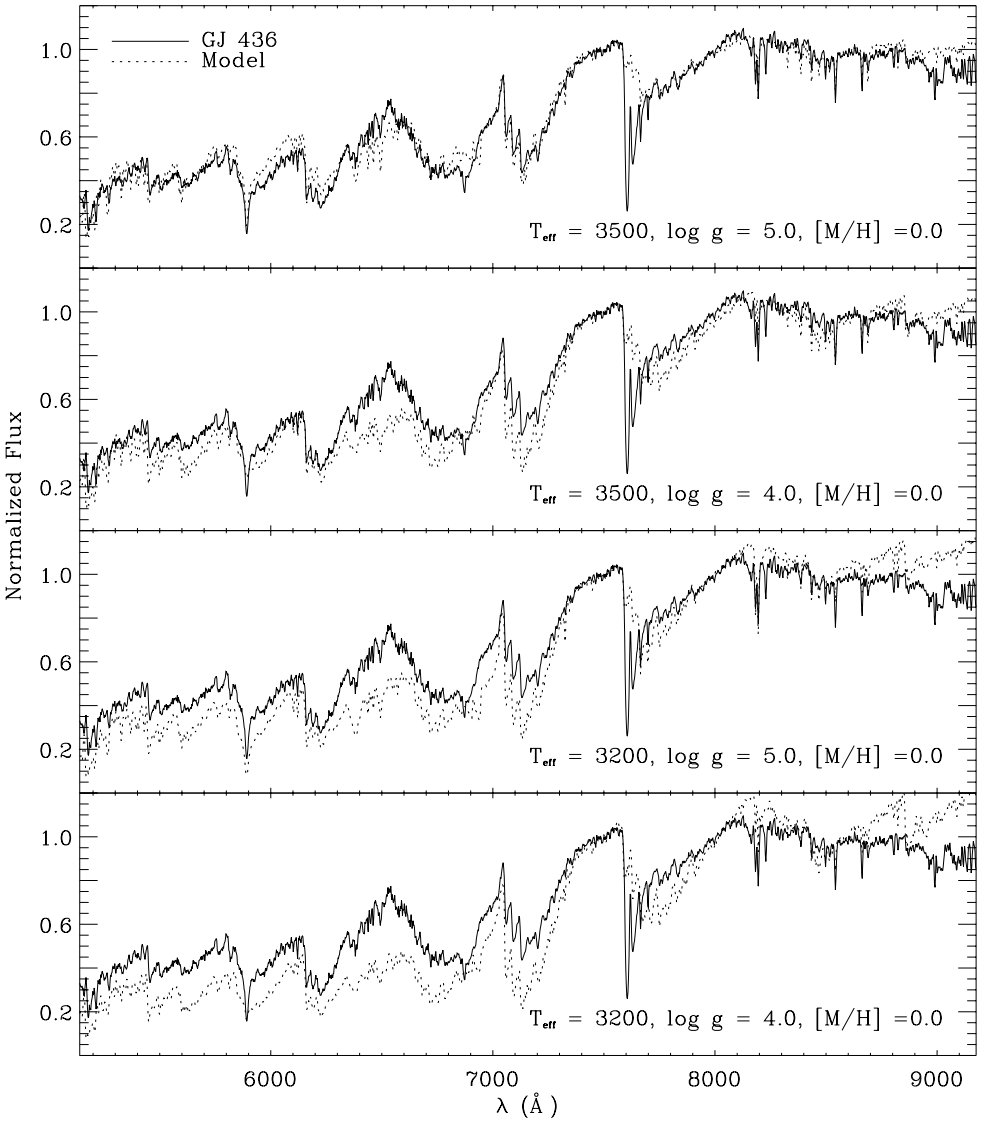

Figure 3.2 Comparison, at low resolution, of the high resolution best fit and the low resolution best fit for GJ 436. The top panel shows the best fit to the low resolution spectrum, while the bottom panel shows the high resolution best fit model. Note that at low resolution, errors in the continuum introduced by the poorly determined TiO lines cannot be directly observed, in contrast to the situation at high resolution (see Figure 3.1).

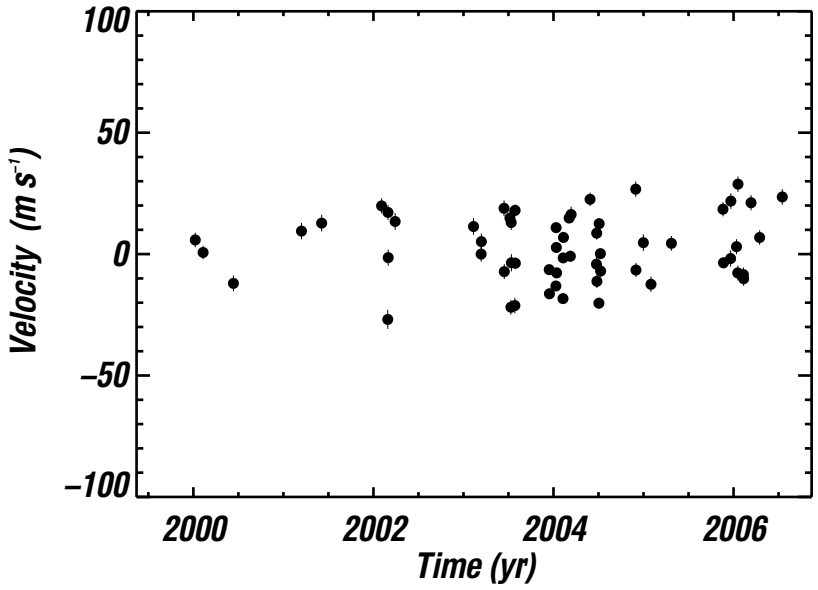

Figure 3.3 Measured velocities vs. time for GJ 436. The RMS scatter of ∼13.5 m s^{-1} is greater than the uncertainties (∼4 m s^{-1}) shown as error bars, indicating real variation in velocity. There is a hint of an upward trend in the velocities. The error bars show the quadrature sum of the internal errors (median 2.6 m s^{-1}) and jitter (1.9 m s^{-1}).

3.4 Doppler Measurements & New Orbital Model for GJ 436b

We have obtained 59 spectra of GJ 436 at the Keck 1 telescope with the HIRES echelle spectrometer (Vogt et al. 1994) during the 6.5–year period, Jan 2000 to July 2006 (JD = 2451552-2453934). These velocities include 17 new, unpublished measurements made during the past two seasons since announcement of the planet, GJ 436b (Butler et al. 2004). In addition, we remeasured the Doppler shifts of all past spectra using a newly improved Doppler analysis pipeline that includes a filter for the telluric absorption lines and a superior template spectrum for spectral modeling. The exposure times were typically 8 min yielding S/N ≈ 150 and resulting in an uncertainty in the radial velocity of 2.6 m s^{-1} (median) per exposure.

The times of all observations, the velocities, and the uncertainties are listed in Table 4. Effects due to secular acceleration have been calculated and removed from the listed velocities. The uncertainties consist of internal errors only, based on the uncertainty in the mean Doppler shift of all ∼700 spectral segments. Occasionally we obtained two or three consecutive spectra within a 30 minute interval from which we computed the weighted average velocity and the correspondingly reduced uncertainty. Figure 3 shows all of the measured velocities vs. time for GJ 436.

We attempted to fit the velocities for GJ 436 with several orbital models shown in Figures 4-6. A circular orbit fit to the velocities, shown in Figure 4, yields residuals correlated in phase and a large value of $\sqrt{\chi^2_\nu}$= 2.04. This fit is unacceptable, and we carry out a statistical assessment of it in section §5 . A full Keplerian model, with the eccentricity allowed to float, produced a superior fit, as shown in Figure 5. This model yields residuals with RMS = 4.76 m s^{-1} and $\sqrt{\chi^2_\nu}$= 1.69, both considerably smaller than the circular orbit. The best-fit parameters from this Keplerian model were P = 2.6439 d, e=0.185, K=18.25 m s^{-1} . Adopting the (revised) stellar mass of 0.44 $M_\odot$ implies a minimum mass for the planet of $M \sin i$ = 0.0706 $M_{\rm JUP}$ = 22.4 $M_{\rm Earth}$ and a semi-major axis of 0.0285 AU.

Table 3.4: Radial velocities for GJ 436

JD -2440000	RV (m s^{-1})	Unc. (m s^{-1})
11552.077	5.84	2.3
11583.948	0.67	2.0
11706.865	-12.05	2.6
11983.015	9.48	2.8
12064.871	12.76	2.9
12308.084	19.86	2.5
12333.038	-26.89	3.4
12334.054	17.15	2.4
12334.935	-1.45	2.7
12363.039	13.43	2.9
12681.057	11.36	2.9
12711.898	0.00	2.4
12712.902	5.14	2.7
12804.878	18.86	2.6
12805.829	-7.21	2.4
12828.800	14.85	2.5
12832.758	-21.88	2.4
12833.763	13.01	2.4
12834.779	-3.56	3.0
12848.752	-21.18	2.6
12849.762	17.95	2.1
12850.764	-3.77	2.1
12988.146	-6.43	1.2
12989.146	-16.33	1.8
13015.141	-13.13	1.5
13016.073	11.10	1.5
13017.046	2.74	1.6
13018.142	-7.65	1.8

JD -2440000	RV (m s^{-1})	Unc. (m s^{-1})
13044.113	-18.32	1.5
13045.018	-1.57	1.5
13045.985	6.91	1.4
13069.032	14.71	1.5
13073.991	-0.89	1.9
13077.066	16.30	2.7
13153.817	22.57	2.0
13179.759	-4.15	2.6
13180.803	8.51	2.3
13181.746	-11.20	2.0
13189.787	-20.17	1.7
13190.754	12.47	1.8
13195.767	0.19	1.7
13196.772	-7.03	2.0
13339.140	26.74	2.5
13340.129	-6.55	2.2
13370.133	4.71	2.9
13401.055	-12.44	2.5
13483.876	4.43	2.4
13693.112	18.49	2.2
13695.138	-3.55	1.8
13724.143	-1.82	2.8
13725.120	21.84	2.6
13748.059	3.06	2.4
13753.075	-7.75	2.4
13754.040	28.81	2.6
13776.052	-8.42	2.2
13777.023	-10.13	2.2
13807.020	21.15	2.5
13841.887	6.84	2.3
13933.781	23.54	2.6

The linear trend in the velocities evident in Figure 3 motivated a final model that combines both a Keplerian orbit and a linear trend in the velocities, presumably caused by a more distant orbiting companion. A least-squares fit to the velocities gave residuals with RMS = 4.27 m s^{-1} , $\sqrt{\chi^2_\nu}$= 1.57, both superior to (lower than) those from the Keplerian model without a trend. (The additional free parameter for the trend was suitably included in both statistics.) This model with the trend gave orbital parameters, P=2.64385±0.00009 d, e = 0.160 ±0.019, $K = 18.34 \pm 0.52$ m s^{-1}, and a linear velocity slope of 1.36 m s^{-1} per year. All orbital parameters are listed in Table 5, and they are not greatly different from

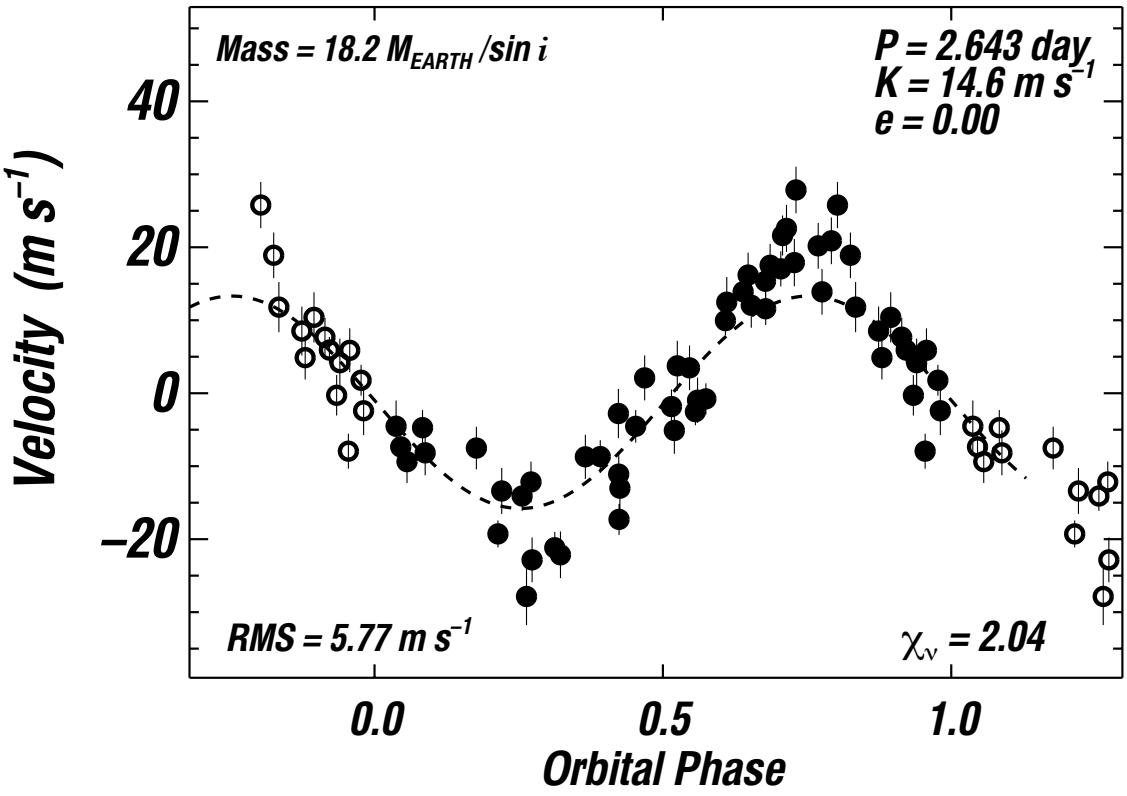

Figure 3.4 Circular orbit fit (dashed line) to measured velocities (filled dots) vs. orbital phase for GJ 436. Repeated points outside phases 0 to 1 are shown as open circles. The resulting parameters are: $P = 2.644$ d, $M \sin i = 0.057$ M_{JUP}= 18.1 M_{Earth}. No velocity trend was added to the Keplerian model. The RMS of the residuals to this fit is 5.77 m s^{-1} and reduced $\sqrt{\chi^2_\nu} = 2.04$, clearly inferior to models with non-zero eccentricity (Fig. 5, Fig. 6).

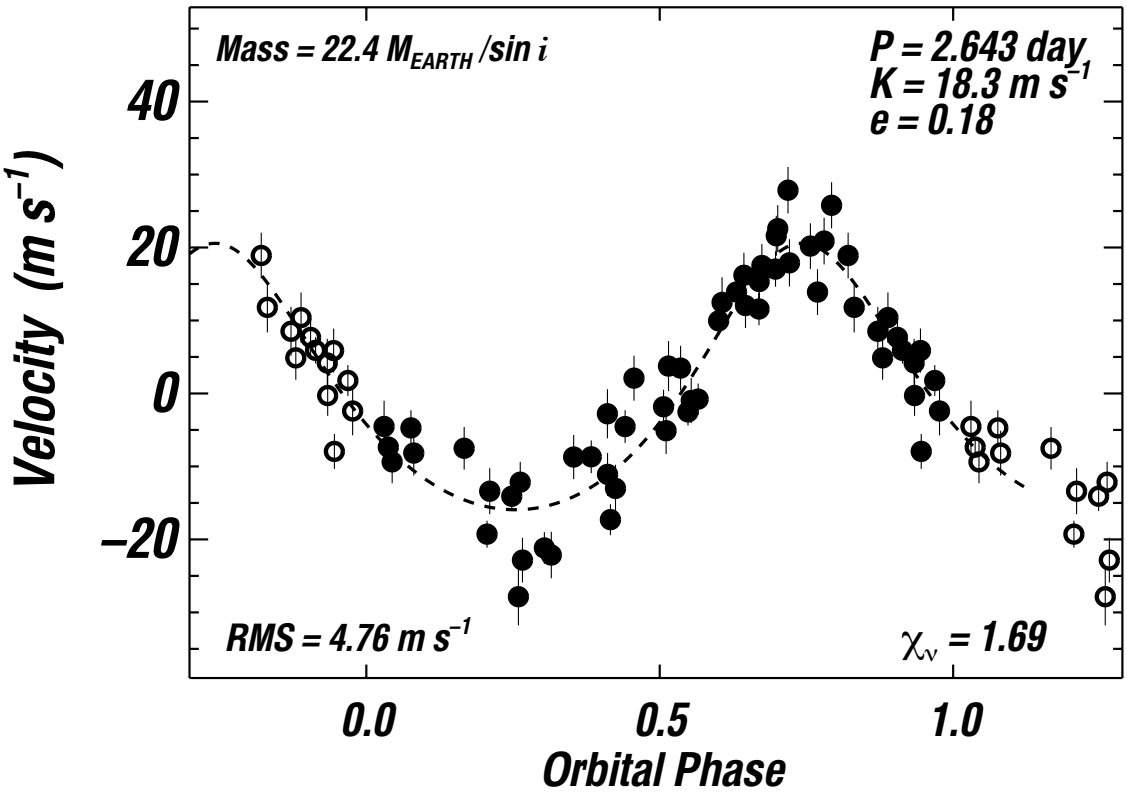

Figure 3.5 Full Keplerian model fit (dashed line) to measured velocities (dots) vs. orbital phase for GJ 436, with repeated points (outside phases 0–1) shown as open circles. $P = 2.6439$ d, $e = 0.18$, $M \sin i = 0.0706$ M_{JUP}= 22.4 M_{Earth}. No velocity trend was added to the Keplerian model. The RMS of the residuals to this fit is 4.76 m s^{-1} with a reduced $\sqrt{\chi^2_\nu} = 1.69$. The uncertainties include internal errors and jitter added in quadrature.

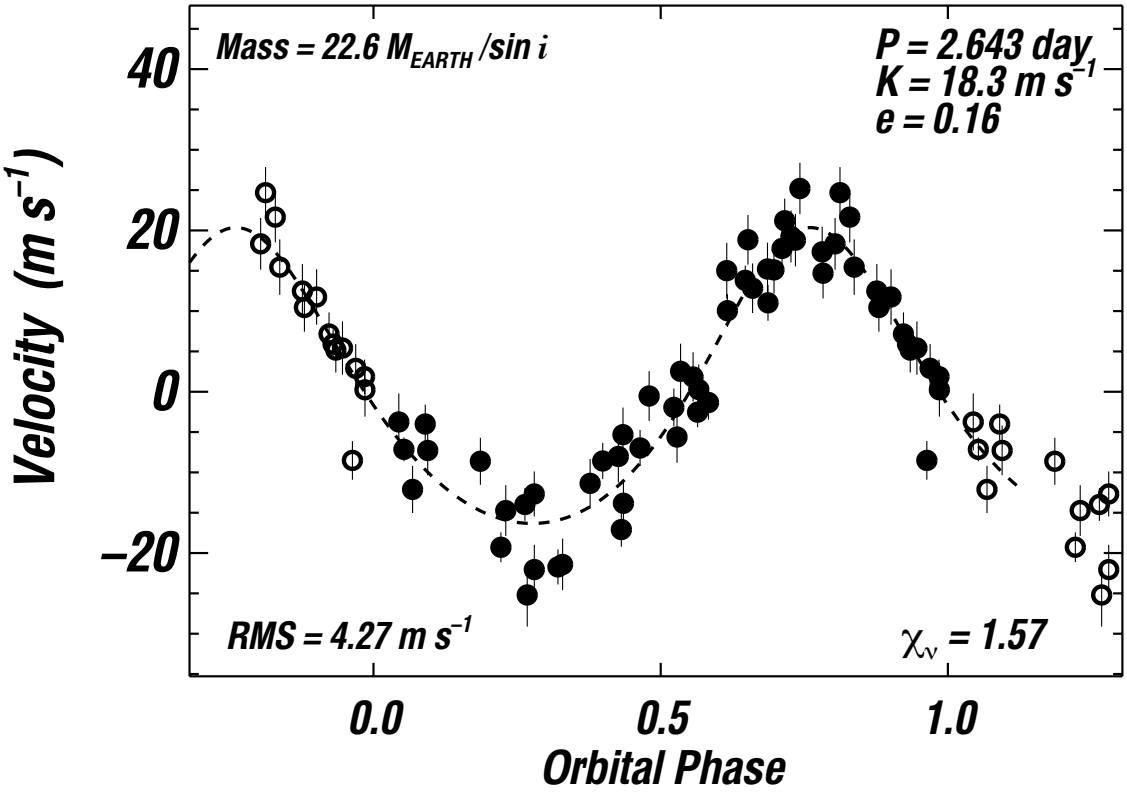

Figure 3.6 Keplerian model plus a linear trend (dashed line) fit to measured velocities (dots) vs. orbital phase for GJ 436. The best-fit orbital parameters are $P = 2.6439$ d, $e = 0.16$, $M \sin i = 0.0713$ M_{JUP}= 22.6 M_{Earth}. This model with a linear trend gives the lowest RMS of the residuals, 4.27 m s^{-1} , and the lowest value of $\sqrt{\chi^2_\nu}$=1.57.

Table 3.5. Orbital parameters for GJ 436

Parameter	
P (d)	2.64385 (0.00009)
T_p (JD)	2451551.716 (0.01)
e	0.160 (0.019)
ω (deg)	351 (1.2)
K_1 (m s^{-1})	18.34 (0.52)
f_1(m) ($M_\odot$)	1.6258e-12
$a_{\rm rel}$(AU)	0.0285
$M \sin i$ (M_{Jup})	0.0713 (0.006)
dv/dt (m s^{-1} per yr)	1.36 (0.4)
Nobs	59
RMS (m s^{-1})	4.27
$\sqrt{\chi^2_\nu}$	1.57

those obtained with no linear trend. The new orbital parameters are only slightly different from those in Butler et al. (2004) who found P=2.6441 d, K=18.1 m s^{-1} , e=0.12. But the current linear trend of 1.36 m s^{-1} per year is smaller than that found by Butler et al. (2004): 2.7 m s^{-1} per year. The modest reduction in RMS and $\sqrt{\chi^2_\nu}$ warrants an assessment of the reality of the trend, provided in §5.

We carried out all Keplerian fits by assigning weights to each Doppler measurement that are the inverse of the quadrature sum of the internal velocity errors and the estimated jitter, 1.9 m s^{-1} for similar M dwarfs, based on the velocity RMS of stable M dwarfs. The best-fit orbital parameters are very weakly dependent on the precise value of jitter.

The model that includes a Keplerian with a linear trend yields the most likely physical parameters for the planet. Adopting the (revised) stellar mass of 0.44 $M_\odot$, the best-fit model implies a minimum mass for the orbiting companion of $M \sin i = 0.0713$ $M_{\rm JUP} = 22.6$ $M_{\rm Earth}$ and a semi-major axis of 0.0285 AU. We note that the value of $M \sin i$ found here is higher than that (0.067 $M_{\rm JUP}$) reported by Butler et al. (2004) due primarily to the 7% higher stellar mass adopted. However, the improvements to the Doppler analysis have reduced the RMS of the velocity residuals to the fit from 5.3 m s^{-1} to 4.3 m s^{-1} .

The non-zero eccentricity of e=0.16±0.02 is somewhat surprising. Among the 23 exoplanets with periods under 4 d, this eccentricity is the highest (Butler et al. 2006), and only one other planet may have an eccentricity as high as 0.10. Tidal circularization is thought to be responsible for the nearly circular orbits of the short period planets. If so, the high orbital eccentricity of this close-in, Neptune-mass planet poses a mystery about its origin.

Two possible resolutions are that a more distant planet pumps its eccentricity or that the tidal Q value is high enough to avoid tidal circularization during the 3-10 Gyr age of this system.

3.5 Orbital Constraints on GJ 436b

Given the short orbital period of GJ 436b, a detection of a non-zero eccentricity can carry implications for eccentricity evolution in this system. In this section, we evaluate the observational evidence for the planet's non-zero eccentricity and the presence of a long-term trend in the radial velocity data. Because the eccentricity of a bound orbit must lie between zero and unity, the best-fit orbit for systems with small orbital eccentricities will suffer from a systematic Lutz-Kelker bias toward larger eccentricities.

As noted in §4, the best-fit orbital solution has an eccentricity of $e = 0.160$ and bootstrap-style resampling suggests an uncertainty of order 0.019. Unfortunately, the error estimates derived from bootstrap-style resampling can significantly underestimate the true uncertainties in orbital parameters, as demonstrated by comparisons with Bayesian analyses (Ford 2005; Gregory 2005). Modern computers and advanced statistical algorithms make it practical to replace this type of frequentist analysis with a statistically rigorous Bayesian analysis. We perform a Bayesian analysis to determine the posterior probability density function (posterior PDF) for the Keplerian orbital elements, assuming the observed radial velocity variations are due to a single planet on a Keplerian orbit. We assume a prior PDF that is the product of prior PDFs for each of the model parameters individually. We assign prior PDFs as follows: $p(P) \sim 1/P$ for $P_{\rm min} \leq P \leq P_{\rm max}$ for the orbital period, $p(K) \sim 1/(K_o + K)$ for $K \leq K_{\rm max}$ for the velocity semi-amplitude, $p(e) \sim 1$ for $0 \leq e < 1$ for the orbital eccentricity, $p(\omega) = 1/2\pi$ for $0 \leq \omega < 2\pi$ for the argument of pericenter, $p(M_0) = 1/2\pi$ for the mean anomaly at a specified epoch, $p(C) \sim 1$ for the mean stellar velocity, and $p(\sigma_j) \sim 1/(\sigma_o + \sigma_j)$ for $\sigma_j \leq \sigma_{\rm max}$ for the stellar jitter. In some simulations where we also include a linear velocity trend, D, we have assumed a prior PDF uniform in slope, $p(D) = 1/2D_{\rm max}$ for $-D_{\rm max} \leq D \leq D_{\rm max}$. We choose the constants $P_{\rm min} = 1$ d, $P_{\rm max} = 6.3$ yr, $K_{\rm max} = 2.8$ km s^{-1} , $\sigma_{\rm max} = 2.8$ km s^{-1} , $K_o = \sigma_o = 1$ m s^{-1} , and $D_{\rm max} = 10$ m s^{-1} per yr, so that the corresponding priors can be properly normalized. We assume that the stellar jitter is Gaussian and uncorrelated, and we add it in quadrature with the observational uncertainty for each observation ($\sigma_i = \sqrt{\sigma_{{\rm obs},i}^2 + \sigma_j^2}$).

The likelihood (the probability of making the actual observations for a given set of model parameters) is computed as the product of independent Gaussians with mean $v_{{\rm obs},i}$ and standard deviation σ_i, at each time t_i, using the actual observation times, observed velocities, and uncertainties in Table 5. We sample from the posterior PDF using the numerical techniques of Markov chain Monte Carlo (Ford 2005, 2006; Gregory 2005). Fig. 3.7 (upper panel) shows the posterior probability distribution marginalized over all model parameters except the orbital eccentricity. When we include a linear slope (solid line), there is only a 5% posterior probability that the eccentricity is less than 0.068 and a 0.1% posterior proba-

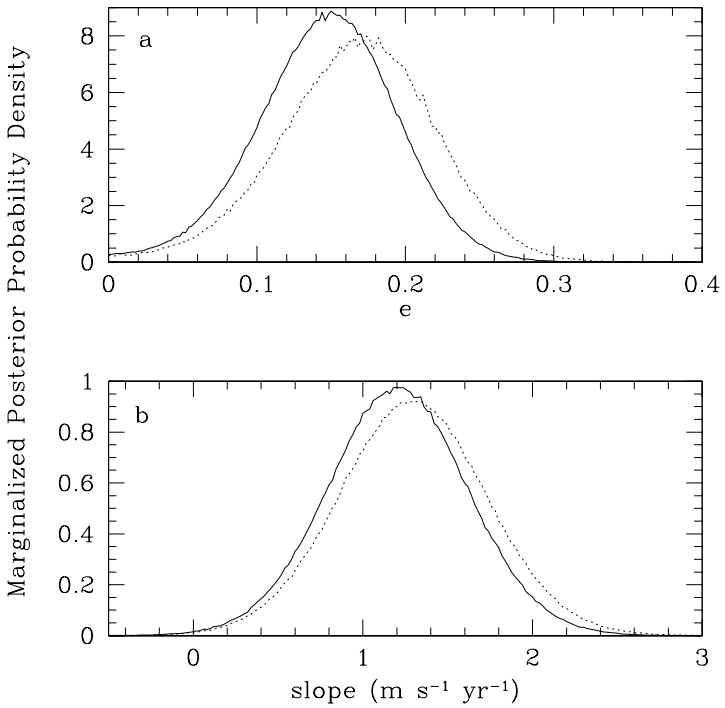

Figure 3.7 The upper panel shows the posterior probability distributions marginalized over all model parameters except the orbital eccentricity for the observations of GJ 436. In the upper panel the solid (dotted) curve assumes a model with (without) a linear slope. The lower panel shows the posterior probability distribution marginalized over all model parameters except the slope. In the lower panel the solid (dotted) curve assumes a model with a slope and a single planet on a Keplerian (circular) orbit.

bility that the eccentricity is less than 0.004, *if we assume a uniform prior for eccentricity.* Similarly, Fig. 3.7 (lower panel) shows the posterior probability distribution marginalized over all model parameters except the slope. When we allow for an eccentric orbit for GJ 436b (solid line), there is a 99.8% posterior probability that the linear slope is positive, *if we assume a uniform prior for the velocity slope.*

The above analyses do not directly address the question of whether the radial velocity observations provide evidence for a non-zero eccentricity and/or non-zero linear slope. To address these questions, we must consider four sets of models: one set of models with a planet on a circular orbit and no slope ($\mathcal{M}_{cn}$), one set of models with a planet on an eccentric orbit and no slope ($\mathcal{M}_{en}$), one set of models with a planet on a circular oribt and a linear slope ($\mathcal{M}_{cs}$), and one set of models with a planet on an eccentric orbit and a linear slope ($\mathcal{M}_{es}$). Since the $\mathcal{M}_{es}$ models have three more model parameters than the models in $\mathcal{M}_{cn}$, we should expect that some models from $\mathcal{M}_{es}$ will provide better fits to the observations than the best models from $\mathcal{M}_{cn}$, even if the planet were actually on a circular orbit. Bayesian

model selection naturally provides a framework for quantifying the "Occam's razor" factor that determines how much better the more complex model must fit must to justify adding the extra model parameters. We construct a composite model ($\mathcal{M}$) that includes a discrete indicator variable that specifies whether to use model $\mathcal{M}_{cn}$, $\mathcal{M}_{cs}$, $\mathcal{M}_{en}$, or $\mathcal{M}_{es}$. We assume prior probabilities for each of these models, $p_{cn} = p_{en} = p_{cs} = p_{es} = 0.25$.

To determine the posterior probability for an eccentric orbit, we must compute the posterior probability PDF marginalized over all parameters except the index specifying the model. Unfortunately, the standard MCMC techniques (e.g., Ford 2005, 2006) allow us to sample from the posterior PDF assuming any one of these models, but do not provide the normalizations. We have used additional simulation techniques to evaluate the ratio of the normalizations of each pair of these models. A detailed description of the various algorithms and the advantages and disadvantages of each will be presented in a subsequent paper (Ford et al. 2006, in prep). Here, we describe only one of the more conceptually simple algorithms. We estimate the necessary integrals with regular Monte Carlo integration, but limit the range of integration to the small volume of parameter space that dominates the contribution to the marginalized posterior probability (as determined from the MCMC simulations).

Our Monte Carlo integration reveals the model with both an eccentricity and a linear slope is strongly favored (by a factor of $\simeq 10^{10}$) over the model with a circular orbit and no slope. If we assume there is a linear slope, then the eccentric model is $\simeq 200$ times more likely than the circular model. Similarly, if we assume an eccentric model, then the model with a linear slope is $\simeq 10^4$ times more likely than the model without a slope. *Therefore, we conclude that the radial velocity observations provide strong evidence for both a non-zero eccentricity and a non-zero linear velocity trend.*

3.6 Discussion

The revised mass for the star GJ 436 of 0.44 $M_\odot$ and the revised orbital parameters and $M \sin i$ for the planet have tightened the constraints on the structure of this planetary system. The minimum mass of the planet remains slightly greater than that of Neptune with $M \sin i = 22.6$ $M_{\rm Earth}$ and orbiting with semimajor axis, $a = 0.0285$ AU .

Two new results have emerged from the present analysis that render the system interesting and puzzling. The eccentricity is definitely non-zero, with $e = 0.16 \pm 0.02$, the highest eccentricity for any exoplanet with an orbital period less than 4 d. It has apparently avoided tidal circularization. Moreover, the velocities exhibit a linear trend of 1.3 m s^{-1} per year that appears to be real, indicating the presence of a more distant companion, the mass and orbit of which remain poorly constrained. It is tempting to suppose that this outer companion is responsible for pumping the eccentricity of the inner planet.

Two scenarios seems possible. In the first scenario, planet b resides in an eccentric orbit and the linear velocity slope is due to a companion so far away that it isn't exciting the eccentricity of planet b. In this case, tidal theory would argue for a not-low value of Q and hence against a rocky planet. Scaling the Earth's Q$\sim$300 by the forcing period and

scaling the Earth's radius by $22^{1/3}$, one gets a tidal circularization time of 2 million years, not consistent with the age of the star that is certainly several billion years. It shows no signs of youth such as rapid rotation, or enhanced magnetic, chromospheric and coronal activity.

If one scales Neptune's Q value, $Q \sim 10^5$, by the forcing period and uses its radius, then the tidal circularization time is 2×10^9 yr. If the planet started on an eccentric orbit, then this timescale is plausible, as the orbit will have only partially circularized. The Q estimates for the ice giants in the solar system range from 10^4 to a few 10^6. Such values provide an interesting constraint on Q for a hot-Neptune.

In a second scenario, the planet b resides on an eccentric orbit, but the slope is due to a planet or binary star that comes close enough to pump the planet's eccentricity despite the tidal damping. In this case, planet b can be terrestrial or an ice giant since it is continually being pumped.

But one wonders if such pumping is consistent with the velocity data. If we naively approximate the outer "planet c" to be on a circular orbit, then $m_c \sin i \sim 0.2$ M_{JUP} (P/20 yr)$^{4/3}$ (slope / 1.25 m/s/yr), where a 20 yr minimum orbital time scale comes from ∼4 times the duration of observations. Even if we take the duration of observations to be the minimum orbital period for planet c, then the ratio of semimajor axes is at least ∼100. With such large separation, the outer planet is unlikely to be effective at exciting an eccentricity.

To test this, we have performed numerical integrations in the secular octupole approximation (averaging over orbits and expanding in terms of ratio of semi-major axes, but not eccentricities, inclinations, or mass ratios). We assume that this approximation gives a rough estimate of the mass of an outer planet in a coplanar system with $\sin i = 1$. For an outer planet orbital period less than 14 years (and hence masses less than 0.12 M_{JUP}), the outer planet would need an eccentricity larger than 0.5 to be able to induce an eccentricity of 0.16 for planet b. Alternatively, an outer planet with orbital period of 25 years (and hence a mass of ∼0.27 M_{JUP}) would need an eccentricity of only 0.2 to be able to induce the observed eccentricity of GJ 436b. The timescale for the secular eccentricity perturbations is less than 10^6 yr. So this configuration would maintain the observed eccentricity of GJ 436b, regardless of the assumed composition and value of the tidal Q. Given that we observe both an eccentricity and a slope, this scenario offers a reasonable explanation. Doppler observations during the upcoming years may reveal the mass and period of the outer planet, if it exists.

Chapter 4

CARMA Millimeter-Wave Aperture Synthesis Imaging of the HD 32297 Debris Disk

Abstract

We present the first detection and mapping of the HD 32297 debris disk at 1.3 mm with the Combined Array for Research in Millimeter-wave Astronomy (CARMA). With a sub-arcsecond beam, this detection represents the highest angular resolution (sub)mm debris disk observation made to date. Our model fits to the spectral energy distribution from the CARMA flux and new Spitzer MIPS photometry support the earlier suggestion that at least two, possibly three, distinct grain populations are traced by the current data. The observed millimeter map shows an asymmetry between the northeast and southwest disk lobes, suggesting large grains may be trapped in resonance with an unseen exoplanet. Alternatively, the observed morphology could result from the recent breakup of a massive planetesimal. A similar-scale asymmetry is also observed in scattered light but not in the mid-infrared. This contrast between asymmetry at short and long wavelengths and symmetry at intermediate wavelengths is in qualitative agreement with predictions of resonant debris disk models. With resolved observations in several bands spanning over three decades in wavelength, HD 32297 provides a unique testbed for theories of grain and planetary dynamics, and could potentially provide strong multi-wavelength evidence for an exoplanetary system.

4.1 Introduction

Debris disks provide the principal means of studying the formation and evolution of planetary systems on timescales of 10−100 Myr. Evidence for exoplanets in these systems can be found by matching density variations in debris disks to theoretical models of the

gravitational perturbations caused by planets (e.g., Reche et al. 2008). A modest sample of debris disks have now been imaged in the visible, and many show substructure such as clumps, warps, and offsets, consistent with dynamical perturbations by massive planets. However, a wide variety of other mechanisms can produce similar structures (Moro-Martin et al. 2007, and references therein). As different wavebands are sensitive to different grain sizes, which are in turn subject to different dynamical influences, multi-wavelength observations offer the most promising path towards definitively classifying the physical mechanisms at work in these systems. At present, only a few debris disks have resolved observations spanning more than a decade in wavelength. A particularly critical, though technologically challenging, deficit of observations lies at (sub)millimeter wavelengths, which trace large grains primarily affected by gravitational forces. To date, bolometer arrays have resolved 8 debris disks in the (sub)mm (e.g., Holland et al. 1998, Greaves et al. 1998). However, such low-resolution ($\theta_{\rm beam} \gtrsim 10''$) single-dish measurements are limited to the largest, nearest disks. Higher resolution interferometric observations are needed to access the larger debris disk population already imaged at shorter wavelengths. Some pioneering work has been done in this area; OVRO and PdBI have detected and resolved two debris disks (Vega: Koerner et al. 2001, Wilner et al. 2002; HD 107146: Carpenter et al. 2005). Recently, Corder et al. (2009) mapped HD 107146 with the Combined Array for Research in Millimeter-wave Astronomy (CARMA) at 1.3 mm, providing the highest fidelity interferometric debris disk map to date. Here, we report the near-simultaneous CARMA detection of HD 32297, the third debris disk mapped with a (sub)mm interferometer. With a sub-arcsecond beam, this detection is the highest angular resolution (sub)mm debris disk observation made to date.

HD 32297 is a ∼30 Myr A-star at 112^{+15}_{-12} pc (Perryman et al. 1997), first discovered to host a resolved debris disk with HST/NICMOS near-infrared (NIR) imaging (Schneider et al. 2005). The discovery image showed an edge-on debris disk extending to 400 AU (3.3″), with an inner-disk brightness asymmetry inward of 60 AU (0.5″). Kalas (2005) subsequently imaged HD 32297 in the optical, revealing an asymmetric, extended outer disk (∼1700 AU, 15″) likely interacting with the interstellar medium. Later, Redfield (2007) detected circumstellar gas in this system, reporting the strongest Na I absorption measured toward any known debris disk. Most recently, Fitzgerald et al. (2007b), hereafter F07, and Moerchen et al. (2007) resolved HD 32297 in mid-infrared (MIR), thermal emission. Detailed analysis of the spectral energy distribution (SED) by F07 showed that multiple grain populations may be present in the disk. The lack of long wavelength data needed to characterize the large grain properties of HD 32297 motivated the CARMA observations presented here.

4.2 Observations and Data Reduction

We observed HD 32297 with CARMA, located 7200 ft above sea level outside Big Pine, California and consisting of six 10.4-m and nine 6.1-m antennas, previously comprising the OVRO and BIMA arrays. We used CARMA's D configuration (baselines: 11−148 m) on 2008 March 06 and the more extended C configuration (baselines: 26−370 m) on 2007

October 26 and 2007 November 08. We tuned the receivers to a central frequency of 227 GHz. The total continuum bandwidth is 1.5 GHz, contained in three 500 MHz bands. Our total observation time was 19 hours in good weather with rms path errors of $\lesssim 175\mu$m and zenith opacities of $\tau_{230} \lesssim 0.35$. Throughout our observations, we used optical offset guiding to maximize pointing accuracy (Corder, Carpenter & Wright 2008, in prep).

We calibrated the data using the MIRIAD software package. We performed passband calibration with 15 minutes integrations on a bright quasar (3C 84, 3C 111) observed at the start of each track. We derived time-dependent phase solutions from 3 minutes integrations on J0530+135, observed following each 15 minutes integration on source. In addition, we used 1 minutes integrations on a secondary calibrator, 3C 120 (observed every cycle), to test the astrometric accuracy of the interferometer and the integrity of our phase solutions. Finally, we flux-calibrated the data using a 5 minutes integration on a planet (Uranus, Mars) observed once per track. The systematic uncertainty in CARMA's absolute flux scale is ∼20% (W. Kwon, private communication).

The 1.3 mm map of HD 32297 combining all observations is shown in Figure 4.1. For this map, we adopted natural weighting to provide optimal sensitivity and processed the visibility data as a mosaic to accomodate the heterogeneous array. We deconvolved the dirty map using the Steer CLEAN algorithm for mosaics (Steer et al. 1984), set to bring the rms in the cleaned region of the residual map to that measured in an off-source region. To emphasize possible resolved structure, we restored the map with a circular beam with radius equal to that of the semimajor axis of the naturally weighted beam ($\theta_{\rm beam} = 0.9''$).

In addition to the new CARMA data presented here, we also extracted Spitzer MIPS photometry from director's discretionary time program 225 (PI: G. Schneider). Using the MOPEX package, we manually calibrated the 24 μm data to remove the strong background gradient and "jailbars" evident in the pipeline processed image. The 70 μm data did not suffer severe artifacts; in this case, we simply mosaicked the data. The 160 μm data are contaminated by a spectral leak, which occurs for bright sources and is typically corrected using observations of a calibration star. However, no such calibration observation was made in this program; we, therefore, include the 160 μm data in this analysis only as an upper-limit. The MIPS fluxes as derived from aperture photometry are $F_\nu(23.68\ \mu{\rm m}) = 0.21 \pm 0.01$ Jy, $F_\nu(71.42\ \mu{\rm m}) = 0.85 \pm 0.06$ Jy, $F_\nu(155.9\ \mu{\rm m}) < 0.46 \pm 0.06$ Jy. In the SED modeling (§4), we adopt calibration uncertainties listed in the MIPS data handbook and apply a color correction appropriate to the modeled grain temepratures.

4.3 Results

Figure 4.1 shows a 1.3 mm continuum source detected at the 7σ level. The observed peak in the map is 2.8 ± 0.4 mJy beam^{-1}. The probability of detecting an unrelated background source within $1''$ of the HD 32297 stellar position is $\ll$1%, based on recent source counts at 850 μm (e.g., Scott et al. 2002). Thus, we conclude that the detected emission is associated with the HD 32297 debris disk. The map morphology suggests the source may be resolved

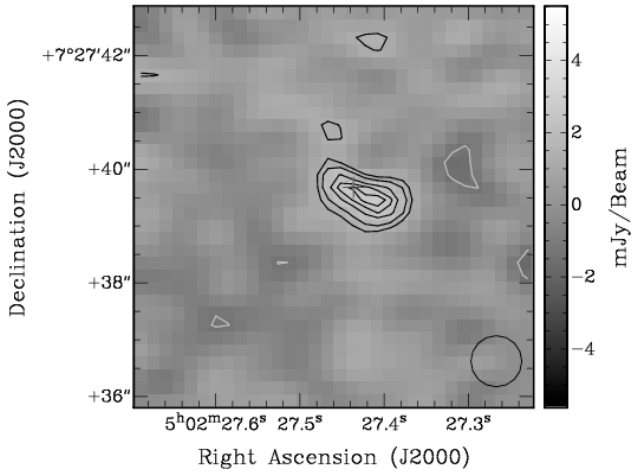

Figure 4.1 CARMA 1.3-mm continuum map of HD 32297. The black cross marks the stellar position, with the full-width representing four-times the total rms millimeter positional uncertainty. Contours begin at 2σ and increase by 1σ thereafter ($\sigma = 0.44$ mJy beam^{-1}, $\theta_{\rm beam} = 0.9''$). The source morphology suggests that HD 32297 may be marginally resolved. The measured position angle is consistent with that observed in the NIR and MIR ($45 - 57°$). The centroid of the disk emission is offset from the stellar position at the 4σ level.

(see below). However, in the D-array data set alone the visibility amplitudes are constant with baseline length (Figure 4.2), suggesting the source is unresolved. We therefore, adopt an integrated flux measured using the D-array data set only: 5.1 ± 1.1 mJy.

The source centroid in Figure 4.1 appears offset from the Hipparcos stellar position (located at phase center). To quantify this result, we fit a point source model to the visibility data; the measured offset is $\Delta r = 0.43 \pm 0.08''$ ($\Delta\alpha = -0.30 \pm 0.08''$, $\Delta\delta = -0.31 \pm 0.07''$). This offset is significantly larger than that observed for test calibrator, 3C 120, observed each source cycle ($\Delta r = 0.041 \pm 0.001''$, $\Delta\alpha = -0.010 \pm 0.002''$, $\Delta\delta = 0.040 \pm 0.001''$). In addition to systematic astrometric uncertainties, we estimate a statistical positional error for HD 32297 of $\Delta\theta = (4/\pi)^{1/4}/\sqrt{8\ln 2} \cdot \theta_{\rm beam}/SNR \sim 0.06''$, in agreement with the formal errors derived from fitting the visibilities. Combining the systematic and statistical errors, the total rms positional uncertainty for HD 32297 is $0.09''$. Thus, the peak continuum emission is offset from the stellar position at the 4σ level.

As previously noted, the Figure 4.1 map suggests the source is marginally resolved. To quantify this effect, in Figure 4.2, we show the visibility amplitudes for the combined data set as a function of projected baseline length from phase center. The data are binned by baseline length in three circularly symmetric annular bins, with widths chosen to provide approximately the same number of visibilities per bin. The errors in amplitude represent the standard deviation in the mean of the visibilities in each bin. Figure 4.2 shows that the source amplitudes decline with baseline length, with a deviation from a point-source model

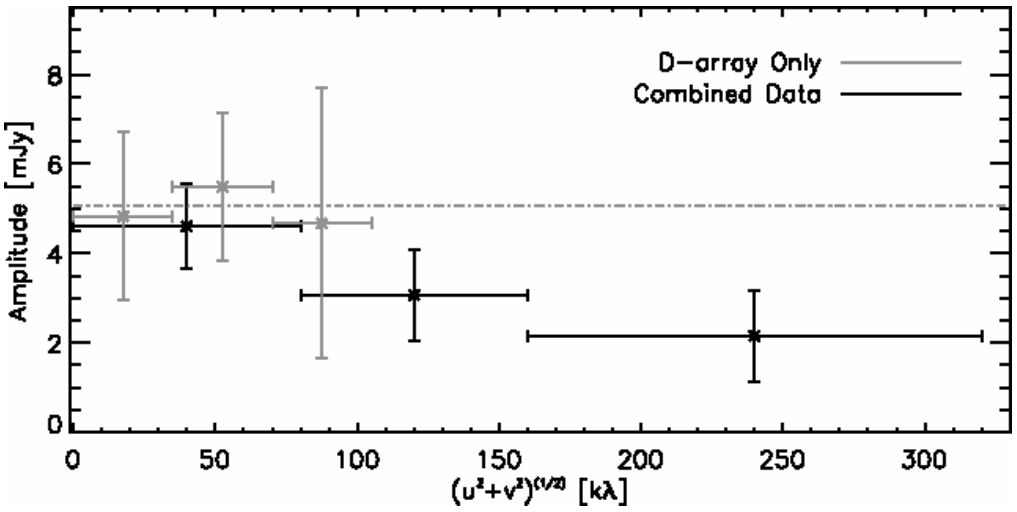

Figure 4.2 Vector-averaged visibility amplitudes as a function of projected baseline length from phase center. The combined data amplitudes decrease with distance from phase center, suggesting the source is resolved at the 2σ level. The D-array data, on the other hand, are consistent with a point-source model (grey dashed line), allowing a robust flux measurement.

of approximately 2σ. Thus, the source appears to be indeed resolved, though additional data are needed to confirm this result. In particular, we note that uncorrected atmospheric phase errors at mm wavelengths can artificially enlarge targets. Still, the observed morphology agrees with that observed at other wavelengths. Fitting an elliptical Gaussian to the visibilities yields a FWHM of $1.8 \pm 0.6'' \times 0.2 \pm 0.6''$ with a position angle of $55 \pm 10°$, consistent to within 1σ of the orientation observed in the NIR and MIR (P.A.$= 45 - 57°$, Schneider et al. 2005, F07, Moerchen et al. 2007).

We observe no CO $J = 2 - 1$ line emission in our data. The 3σ limit is 22 mJy beam^{-1} (1.5 K, $\theta_{\rm beam} = 0.70'' \times 0.52''$) in a 42 km s^{-1} channel. Adopting the same assumptions as Dent et al. (2005), the corresponding gas mass limit is $M_{gas} \lesssim 0.3 M_{\rm Jup}$.

4.4 Discussion

F07 attempted to model the observed SED and N'-band image of HD 32297 with a single ring of grains of characteristic size, but found that a second population of grains was needed to adequately fit the observed SED for $\lambda \gtrsim 25\mu$m. Indeed, the contrast between the observed mm and N'-band morphologies (see below and Figure 4.4) suggests that the grains responsible for the emission at each wavelength constitute separate populations. To test whether the population of mm-emitting grains is consistent with the second, larger grain population proposed by F07 to fit the SED at 25 μm $\lesssim \lambda \lesssim$ 60 μm, we revisit the F07 model, adopting their data and fitting method, and incorporating the Qa-band flux of Moerchen et al. (2007) and the new MIPS and CARMA fluxes. The free parameters in

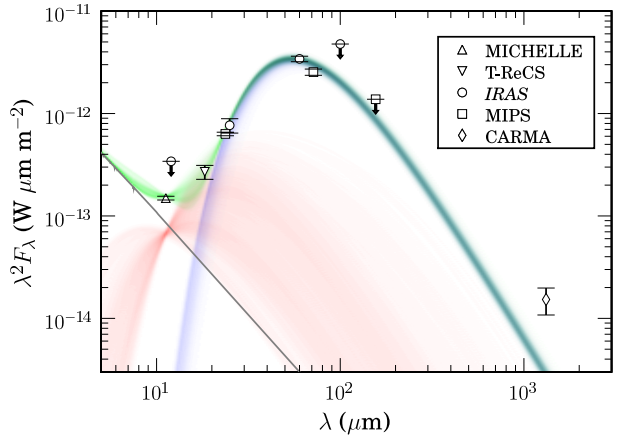

Figure 4.3 Two-population SED fit (see text and F07). The small-grain population is plotted in red, the large-grain population in blue, the stellar photosphere in grey, and the composite model in green. The relative shadings correspond to the 2-d histograms of the component SEDs for each model state in the Markov chains. Photometry references are as follows: MICHELLE (F07), T-ReCS (extracted from data in Moerchen et al. (2007)), IRAS (Moór et al. 2006), MIPS (this paper), CARMA (this paper). The model provides a good fit to the mid- and far-infrared data but underestimates the observed mm flux, potentially providing evidence for a third grain population.

the single population model of F07 are the disk inclination (i), position angle (PA), radii of the inner and outer edges (ϖ_0, ϖ_1), surface density power-law index (γ), vertical optical depth to absorption at the inner edge ($\tau_0 \equiv \tau_\perp^{\rm abs}(\varpi_0)$), stellar flux factor ($\xi$), and effective grain size ($\lambda_{\rm sm}$). To fit the long-wavelength SED ($\lambda \gtrsim 25\mu$m), we augment this model with a population of larger grains of effective size $\lambda_{\rm lg}$ and total emitting area $A_{\rm lg}$, located in a narrow ring at the small-grain inner-disk edge, ϖ_0. These grains contribute flux, $F_{\nu,{\rm lg}}$, according to:

$$\epsilon_{\nu,{\rm lg}} = \begin{cases} \lambda_{\rm lg}/\lambda & \text{if } \lambda > \lambda_{\rm lg}, \\ 1 & \text{otherwise,} \end{cases} \tag{4.1}$$

$$T_{\rm lg}(r) = 468 \left(\frac{L_*/L_\odot}{\lambda_{\rm lg}/1\,\mu{\rm m}}\right)^{1/5} \left(\frac{r}{1\,{\rm AU}}\right)^{-2/5} {\rm K}, \tag{4.2}$$

$$F_{\nu,{\rm lg}} = \left(\frac{A_{\rm lg}}{d^2}\right) \epsilon_{\nu,{\rm lg}} B_\nu[T_{\rm lg}(\varpi_0)]. \tag{4.3}$$

Following F07, we ran three Monte Carlo Markov chains with 3×10^4 samples, and simulataneously fit both the large and small grain populations. The results of this procedure are listed in Table 4.1, and the corresponding range of allowed dust emission is plotted in Figure 4.3 (red: small grains, blue: large grains, grey: photosphere, green: composite). While the two-population model provides a satisfactory fit to the mid- and far-infrared data, the mm flux is underestimated at the 4σ level, suggesting that the second grain population

Table 4.1. Best-fit model parameters

Parameter	Best-fit	Description
i (deg)	90 ± 5	disk inclination
PA (deg)	46 ± 3	disk position angle
ϖ_0 (AU)	70^{+20}_{-10}	inner edge
ϖ_1 (AU)	> 1200	outer edge
$\log_{10} \tau_0$	$-2.4^{+0.3}_{-0.2}$	vertical optical depth at ϖ_0
γ	$<$ -1.63	surf density power-law index
$\xi/7.22 \times 10^{-20}$	1.03 ± 0.03	$(R_*/d)^2$, stellar flux factor
$\log_{10}(\lambda_{\rm sm}/1\,\mu{\rm m})$	$-1.4^{+0.6}_{-1.3}$	small grain effective size
$\log_{10}(A_{\rm lg}/1\,{\rm cm}^2)$	28.9 ± 0.2	large grain emitting area
$\log_{10}(\lambda_{\rm lg}/1\,\mu{\rm m})$	$1.3^{+0.2}_{-0.1}$	large grain effective size

Note. — Confidence intervals are 95% for marginal posterior distributions. Adopted priors are as in F07, except for γ, which is constrained to be in the domain [-4,0] due to the inconsistency of rising surface density with the scattered-light image and CARMA map; the large grain effective size was constrained by a log-uniform prior from 1 nm to 100 mm and a requirement that $\lambda_{\rm lg} > \lambda_{\rm sm}$.

proposed by F07 is not responsible for the majority of the mm flux. Nevertheless, the new MIPS data lend further evidence to the F07 suggestion that two populations are needed to fit the observed SED for $\lambda \lesssim 160\mu$m. Therefore, the fit suggests at least three distinct populations are traced by the current observations. However, from the two-population model, only the 1.3 mm flux appears to trace the putative third population. Since this population is described by both a mass/emitting area and a size/temperature, we lack sufficient data to fully characterize it via modeling. We note, though, that this population likely traces $\gtrsim 95\%$ of the total dust mass. Assuming a characteristic stellocentric distance of $\sim$50 AU (§3), $L_* = 5.4 L_\odot$ (F07), and an effective grain size of 1.3-mm, the implied mm grain temperature is $\sim$30 K, suggesting a dust mass of $M_{\rm mm} \sim M_\oplus$ (adopting an opacity of 1.7 cm^2 g^{-1}). This estimated mass is among the highest observed for debris disks detected in the (sub)mm and is two orders of magnitude larger than that implied for the "large-grain" population in the SED fit: $M_{\rm lg} \sim 0.02 M_\oplus$ (using the fitted parameters in Table 4.1 and assuming spherical grains with a density of 1 g cm^{-3}). Future far-infrared / sub-mm observations are needed to confirm the three populations proposed here and better constrain their properties.

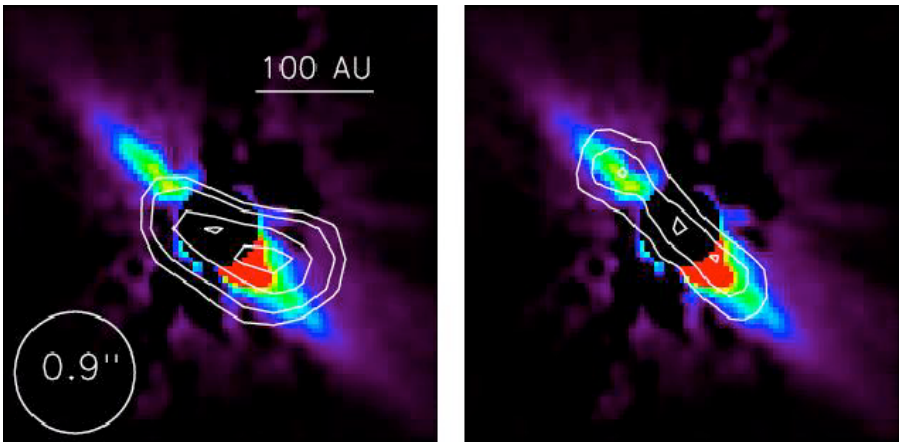

Figure 4.4 *Left:* CARMA contours of HD 32297, overlaid on the NIR scattered-light image from Schneider et al. (2005). *Right:* Photosphere-subtracted MIR contours from F07 overlaid on the same image. The asymmetry in the CARMA data between the northeast and southwest lobes suggests the large, mm-sized grains may be trapped in resonance with an unseen exoplanet. A similar asymmetry is also observed in scattered light but not in the MIR. The contrast between asymmetry at short and long wavelengths and symmetry at intermediate wavelengths is a direct prediction of the resonant debris disk models of Wyatt (2006).

To address the observed mm morphology, in Figure 4.4, we qualitatively compare the CARMA mm map (contours, left panel) to the MIR image of F07 (contours, right panel) and the NIR scattered-light image of Schneider et al. (2005) (color, both panels). The images at all three wavelengths are consistent with an edge-on disk. However, while both the NIR and CARMA data exhibit a brightness asymmetry between the northeast and southwest lobes inward of $\sim$0.5″, the F07 MIR image is consistent with azimuthal symmetry. We note that Moerchen et al. (2007) found evidence for asymmetry in their Qa-band data, though their data were not PSF subtracted, and the asymmetry was in the opposite sense as observed in the NIR / CARMA data (NE lobe brighter than SW).

Recently, Grigorieva et al. (2007) used predictions from their numerical model of collisional avalanches to suggest that the observed scattered-light asymmetry in HD 32297 results from the breakup of a large planetesimal. However, while a massive collision can explain the observed NIR and mm morphology, it is not clear why the MIR image would not show a similar asymmetry. An alternative hypothesis is that the structure results from a planetary-induced resonance. In this case, the dust is either trapped in resonance as it drifts inward due to Poynting-Robertson drag, or it remains locked in resonance after being generated by parent planetesimals in resonance themselves (e.g., Krivov et al. 2007, and references therein). Interestingly, a recent study of the latter mechanism by Wyatt (2006) directly predicts a contrast between asymmetry at short and long wavelengths and symmetry at intermediate wavelengths, as observed in HD 32297. In this model, (sub)mm emission is dominated by

large grains, which have the same clumpy resonant distribution as the parent planetesimals. Small grains, traced at short wavelengths, exhibit a similar asymmetry, as they are preferentially born in the high density, resonant structures before being rapidly expelled from the system. Lastly, moderately-sized grains sampled at intermediate wavelengths remain bound to the star, but have fallen out of resonance due to radiation pressure and are subsequently scattered into an axisymmetric morphology.

This proposed scenario of Wyatt (2006) conveniently explains the qualitative picture for HD 32297 depicted in Figure 4.4, yet we caution that this suggestion is highly speculative, and future rigorous modeling of this system is needed to draw firm conclusions from the available data. One potential problem with this hypothesis is that the SED model predicts that the small (N'-band-emitting) grains have sizes $\lesssim 1$ μm (Table 4.1), similar to that expected to produce the NIR scattered-light image (see discussion in F07). However, the interpretation of Figure 4.4 in terms of the Wyatt (2006) models requires that the NIR-scattering and MIR-emitting grains have different sizes. This ambiguity could potentially be resolved through simultaneous modeling of scattering and emission, incorporating the optical image presented in Kalas (2005). Most importantly, and independent of speculation, HD 32297 is currently one of only a few debris disks with resolved observations in four wavelength regimes (optical, NIR, MIR, mm). Taken together, these observations can provide a unique testbed for theories of grain and planetary dynamics.

Chapter 5

Hubble Space Telescope Optical Imaging of the Eroding Debris Disk HD 61005

Abstract

We present Hubble Space Telescope optical coronagraphic polarization imaging observations of the dusty debris disk HD 61005. The scattered light intensity image and polarization structure reveal a highly inclined disk with a clear asymmetric, swept back component, suggestive of significant interaction with the ambient interstellar medium. The combination of our new data with the published 1.1 μm discovery image shows that the grains are blue scattering with no strong color gradient as a function of radius, implying predominantly sub-micron sized grains. We investigate possible explanations that could account for the observed swept back, asymmetric morphology. Previous work has suggested that HD 61005 may be interacting with a cold, unusually dense interstellar cloud. However, limits on the intervening interstellar gas column density from an optical spectrum of HD 61005 in the Na I D lines render this possibility unlikely. Instead, HD 61005 may be embedded in a more typical warm, low-density cloud that introduces secular perturbations to dust grain orbits. This mechanism can significantly distort the ensemble disk structure within a typical cloud crossing time. For a counterintuitive relative flow direction—parallel to the disk midplane—we find that the structures generated by these distortions can very roughly approximate the HD 61005 morphology. Future observational studies constraining the direction of the relative interstellar medium flow will thus provide an important constraint for future modeling. Independent of the interpretation for HD 61005, we expect that interstellar gas drag likely plays a role in producing asymmetries observed in other debris disk systems, such as HD 15115 and δ Velorum.

5.1 Introduction

Nearly two dozen dusty debris disks surrounding nearby stars have now been spatially resolved at one or more wavelengths. Many of these systems show clear similarities. For example, the radial architecture of several debris disks can be understood in terms of a unified model of steady-state dust production via collisions in a parent planetesimal belt (e.g., Strubbe & Chiang 2006). However, while the observed structure of many systems is ring-like (Kalas et al. 2006; Wyatt 2008), most disks show substructure such as clumps, warps, offsets, and brightness asymmetries not explained in traditional steady-state collisional grinding models.

These unexpected features have triggered a great deal of recent theoretical work. The effects of massive planetesimal collisions, sandblasting by interstellar grains, close stellar flybys, dust avalanches, and secular and resonant perturbations by exoplanets have all been invoked to explain the observations (e.g., Moro-Martin et al. 2007, and references therein). However, as many of these theories produce similar structures, further observational constraints are needed to better understand the key forces affecting disk structure and the circumstances in which they apply.

At a heliocentric distance of 34.5 pc (Perryman et al. 1997), the debris disk surrounding HD 61005 (SpT: G8 V; Gray et al. 2006), is a promising target for advancing our understanding in this area. The significant infrared excess for this source ($L_{\rm IR}/L_* = 2 \times 10^{-3}$) was recently discovered as part of the Spitzer FEPS survey (Carpenter et al. 2009), indicating 60 K blackbody-emitting grains $\gtrsim$ 16 AU from the star. Follow-up Hubble Space Telescope (HST) coronagraphic imaging observations with the Near Infrared Camera and Multi-Object Spectrometer (NICMOS; HST/GO program 10527; D. Hines, PI) resolved the source (Hines et al. 2007, hereafter H07), revealing an unprecedented swept, asymmetric morphology, suggestive of significant interaction with the interstellar medium (ISM). H07 suggested that this system could be a highly inclined debris disk, undergoing ram pressure stripping by the ambient ISM. However, this interpretation requires an unusually high interstellar density for the low-density Local Bubble in which HD 61005 resides. Furthermore, the single wavelength intensity image was insufficient to provide strong constraints on the dominant size of the scattering grains and the overall scattering geometry.

To further quantify the physical properties of grains seen in scattered light and the overall geometry of the system, we obtained optical coronagraphic polarimetry imaging observations of HD 61005 with the Advanced Camera for Surveys (ACS) onboard HST. As demonstrated by Graham et al. (2007) for the case of AU Mic, polarization observations in scattered light are invaluable for breaking degeneracies between grain scattering properties and their spatial distribution. Furthermore, the ACS data represent a factor of two improvement in angular resolution compared to the 1.1 μm discovery observations. In addition to these new imaging data, we also obtained a high resolution optical spectrum to characterize ambient interstellar gas surrounding this system. In §2, we describe the steps taken in observing and reducing these data. In §3, we discuss the results of these observations, their consequences for the system scattering geometry, and the additional constraints they

provide when combined with the 1.1 μm NICMOS image. In §4, we explore whether interactions with ambient interstellar gas can plausibly explain the observed swept, asymmetric morphology in this system. We discuss the implications for these potential explanations in §5 and summarize our findings in §6.

5.2 Observations and Data Reduction

We obtained optical coronagraphic observations of HD 61005 using the ACS high resolution camera (HRC) 1.8″ diameter occulting spot on 2006 December 19 (HST/GO program 10847; D. Hines, PI). In each of two contiguous orbits, we imaged HD 61005 with the F606W filter in combination with the POL0V, POL60V and POL120V polarizer filters (two 340 second exposures per filter combination). Aside from the telescope position angle, which is rotated 23.032 degrees between orbits, the observational procedures for the two HD 61005 orbits were identical. Before the HD 61005 orbits, we observed the point-spread function (PSF) reference star HD 82943 (SpT: F9 V; Gray et al. 2006; B = 7.16, V = 6.56) using an observing sequence identical to the two orbits allocated to HD 61005 (B = 8.93, V = 8.22). We also observed a second PSF star, HD 117176 (SpT: G5 V; Gray et al. 2001; B = 5.69, V = 5.00), in an identical manner following the HD 61005 orbits.

For each filter combination, we combined the two 340 second, pipeline processed (bias subtracted, flatfielded) frames by excluding the maximum value at each pixel position, thereby minimizing the impact of cosmic ray events. After dividing by the cumulative integration time of each frame, we performed sky subtraction by taking the median value in a 10×20 pixel box in the lower left corner of the chip, which is the position farthest from the bright target star. We registered the images by selecting a fiducial HD 61005 image (the POL0V image in the first orbit) and subtracting all other HD 61005 frames using small offsets (0.02 pixels) to minimize the residuals in regions dominated by light from the stellar PSF. The offsets that minimize residual differences between frames were then applied to the individual POL0V, POL60V, and POL120V images to align them to a common reference frame relative to the star. We carried out an identical registration procedure for the two PSF reference stars.

We then subtracted the HD 61005 PSF in each of the three POL0V, POL60V, and POL120V frames by the corresponding frames from each of the two PSF reference stars. Prior to subtraction, we scaled each reference star to match the expected brightness of HD 61005, using photometry obtained from the direct images. The HD 117176 observations, made immediately following the HD 61005 orbits yielded a better subtraction than the HD 82943 observations, made five weeks prior to the HD 61005 orbits. We therefore used the subtraction obtained with HD 117176 for all subsequent analysis.

Following PSF subtraction, we corrected the resultant images for geometric distortion yielding 25 mas × 25 mas pixels. We then constructed Stokes parameter images corrected for instrumental polarization following Pavlovsky (2006). For the ACS/HRC/F606W/POLV instrumental configuration and high fractional linear polarization ($p = (Q^2+U^2)^{1/2}/I \geq 0.2$),

the residual systematic error is 10% of the computed polarization fraction. For less strongly polarized sources ($p < 0.2$), the systematic error in the degree of linear polarization is approximately constant at $\sigma_p = 0.01$. In both cases, the systematic uncertainty in position angle is 3°.

We next calculated polarization vectors from the derived Stokes images. As the polarization fraction is intrinsically positive and biased upwards by noise, we employed the spatial binning algorithm of Cappellari & Copin (2003) to bin the Stokes I, Q, and U images to approximately constant signal-to-noise prior to this calculation. Within $\sim 1.4''$ of the star, the computed polarization vectors become significantly disordered in magnitude and direction, as a result of systematic PSF subtraction errors. We therefore only consider polarization vectors outside this radius in our analysis. The surface brightness at $0.9 - 1.4''$ is similarly compromised and should be treated with caution.

Finally, we converted from instrumental to physical brightness units using the synthetic photometry package, Synphot. As input, Synphot requires the instrument configuration (camera, coronagraph, wideband and polarizing filters) and the source spectrum across the band. Since the latter is unknown, we performed the calculations three times assuming: (1) a flat spectrum, (2) a $T_{\rm eff} = 5500$ K Kurucz synthetic spectrum approximating the G-dwarf stellar spectrum, and (3) a spectral slope across each band that is the same as that calculated between the NICMOS and ACS bands using method (2). All methods yielded conversion factors within 1% of each other, suggesting the assumed source spectrum factors negligibly into the total color uncertainties.

In addition to the ACS observations, we analyze two additional data sets: (1) The NICMOS F110W image; a full description of the NICMOS data acquisition and reduction is given in H07. (2) High resolution (R $\approx$ 60,000) echelle spectra for HD 61005 and two comparison stars of similar spectral type (HD 33822: $T_{\rm eff} = 5850$ K, HD 13836: $T_{\rm eff} = 5580$ K; Masana et al. 2006). The spectra were obtained on the Keck I telescope with the HIRES spectrometer on 30 Dec 2004, 16 Jan 2006, and 09 Nov 2008. The wavelength range was 3700-6200 Å, though our analysis concerns only the Na I D lines at 5889.951 Å and 5895.924 Å. We used a standard procedure to perform flat-fielding, sky subtraction, order extraction, and wavelength calibration of the raw echelle images (Butler et al. 1996; Vogt et al. 1994).

5.3 Results

5.3.1 ACS Scattered Light and Polarization

Two-dimensional morphology and polarization structure

Figures 5.1 and 5.2 display the F606W total intensity image of HD 61005 on a logarithmic and linear scale, respectively. The figures show two distinct morphological components. The first component, denoted by NE1 and SW1 in Figure 5.2, resembles a near edge-on disk. The putative midplane for this component is observed to extend out to $\sim 3''$ from the star, where the signal-to-noise per pixel falls below unity. The second morphological component is

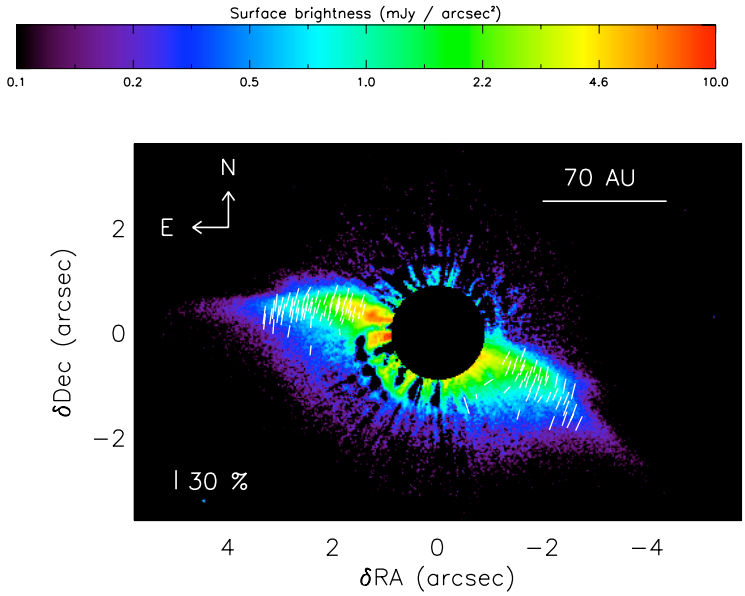

Figure 5.1 Logarithmically-scaled image of HD 61005 in Stokes I at ≥ 0.1 mJy arcsec^{-2} with polarization vectors and a 1.8″ coronagraphic mask overplotted. The color bar units were calculated using the synthetic photometry package, Synphot. The plotted polarization vectors were computed from Stokes images binned to approximately constant signal-to-noise.

detected below the nominal disk midplane. This component exhibits an asymmetric, "swept back" morphology, suggestive of significant interaction with the interstellar medium. This unusual structure was first noted by H07 in their NICMOS F110W discovery image. Both the disk-like and swept back components additionally exhibit a striking asymmetry between the northeast and southwest sides of the source. At a given projected radius, the northeast side of the source is approximately twice as bright as the southwest side. This brightness asymmetry is also seen in the NICMOS F110W image (e.g., H07, Figure 4).

Figure 5.3 displays the polarized flux of image of HD 61005, while Figure 5.1 overplots polarization vectors on the Stokes I image, spatially binned according to the procedure outlined in §2. The polarization vectors in Figure 5.1 show that along the plane of the disk, the fractional polarization increases with radial distance from the star from $\sim 10\%$ to $\sim 35\%$. The orientation of the electric field within $\sim 2.1''$ also appears perpendicular to the nominal disk midplane. In the swept back area of the source, the polarization vectors rotate to become approximately perpendicular to the outer edge of this component. The fractional polarization in this region is similar to that seen in the outer part of the disk component.

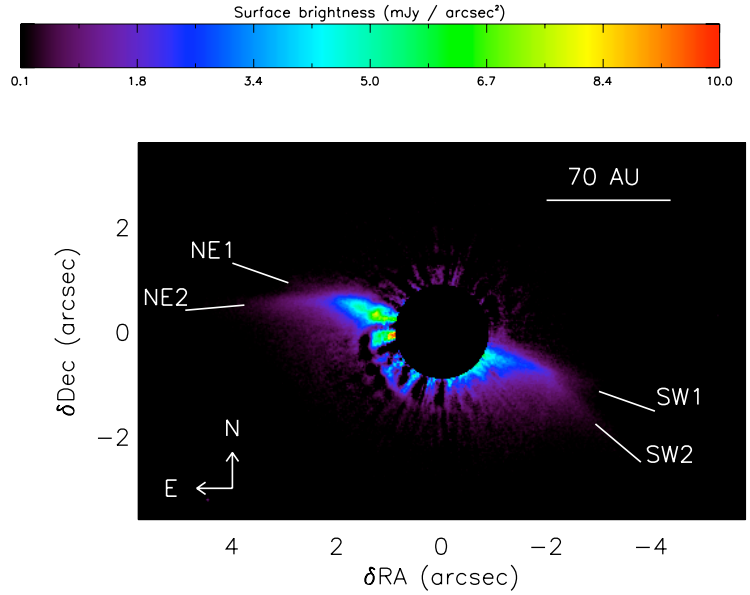

Figure 5.2 Same as Figure 5.1, only with a linear display scale and without polarization vectors. Overplotted are labels for the surface brightness components displayed in Figure 5.5.

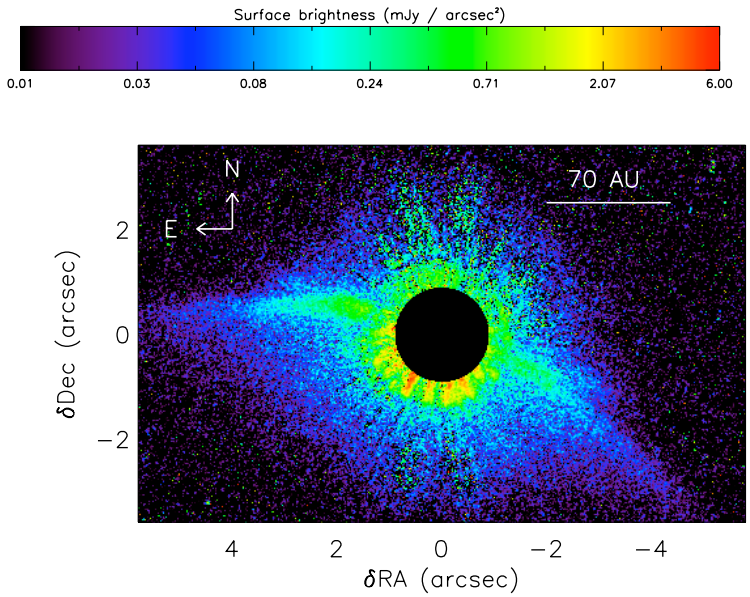

Figure 5.3 Logarithmically-scaled polarized flux ($\sqrt{Q^2 + U^2}$) image of HD 61005.

Disk component parameters

The ACS polarization results add further evidence to the suggestion by H07 that HD 61005 is a near edge-on debris disk. In particular, the HD 61005 polarization structure is very similar to that seen in the spectrally blue edge-on debris disk around the M dwarf, AU Mic, observed using the same instrumental configuration (Graham et al. 2007). The midplanes of both HD 61005 and AU Mic exhibit high fractional polarization ($p_{\max} \sim 0.4$) which increases with projected radius. Similarly, both disks exhibit an electric field orientation perpendicular to the disk midplane at all projected radii. These features are expected for small-particle ($x \lesssim 1$) scattering in an edge-on disk (Kruegel 2003).

For HD 61005, these effects are quantified in Figure 5.4, which shows the binned polarization vector position angles and magnitudes from Figure 5.1. Linear fits to the one-dimensional polarization position angles (PA) versus projected distance within 2.1″ imply flat slopes, as expected for a highly-inclined disk geometry (-5.1 ± 2.5 and 1.0 ± 3.3 for the northeast and southwest sides, respectively). Averaging all polarization position angles within 2.1″, the implied disk position angle is 71.7 ± 0.7 deg, where the listed uncertainty is purely statistical and does not include the additional 3 deg calibration uncertainty (§2). The steady increase in polarization fraction with projected radius is also seen in Figure 5.4. Linear fits to the binned polarization fraction over the full extent of the source imply slopes of 0.09 ± 0.01 and 0.11 ± 0.01 for the northeast and southwest disk sides, respectively.

As an independent check on our disk interpretation, we fit elliptical isophotes to the total intensity image from Figures 5.1 and 5.2, assuming a circularly symmetric disk viewed in projection. We independently fit eight isophotes outside 1.4″ for $I > 1.3$ mJy arcsec^{-2}. The implied disk position angle from these fits is 70.7 ± 0.5 deg, in good agreement with the position angle inferred from the electric field orientation within 2.1″. The implied inclination to the line of sight from these fits is $i = 80.3 \pm 0.6$ deg.

Swept component parameters

The disk structure described above contrasts with previously imaged presumed interstellar dust phenomena, such as the infrared bow structure surrounding the A star δ Velorum (Gáspár et al. 2008) and the filamentary cirrus surrounding some Vega-like stars with significant infrared excess (Kalas et al. 2002). Nevertheless, Figures 5.1 and 5.2 clearly reveal a second asymmetric component of the source not typical of nearby debris disks and suggestive of interaction with the interstellar medium.

The polarization signature of this component is evident in the systematic rotation of the polarization vectors outside $\sim$ 2.1″. Linear fits to the one-dimensional polarization position angles versus projected distance (Figure 5.4) give non-zero slopes of 8.2 ± 1.0 for the northeast lobe -5.8 ± 1.9 for the southwest lobe. Estimates for the position angles of the outer edge of this component (cuts NE2 and SW2 in Figure 5.2) are obtained from the outermost polarization vector position angles. The implied position angle for component NE2 is 82.8 ± 2.1 deg; the result for SW2 is 65.1 ± 3.8 deg.

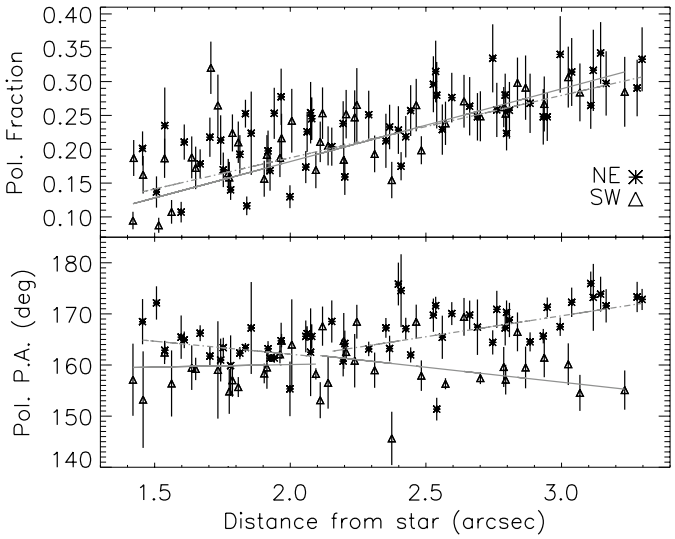

Figure 5.4 One dimensional version of the binned polarization vectors displayed in Figure 5.1. In the top panel, the data show a clear increase in fractional polarization with distance from the star. Linear fits to the data are overplotted in grey with a solid line for the southwest side and a dot-dashed line for the northeast side. In the bottom panel, the rotation of the electric field orientation in the swept back outer disk is seen in the deviation from the nominal midplane polarization position angle outside $\sim 2.1''$. Linear fits for data in and outside this radial distance are overplotted.

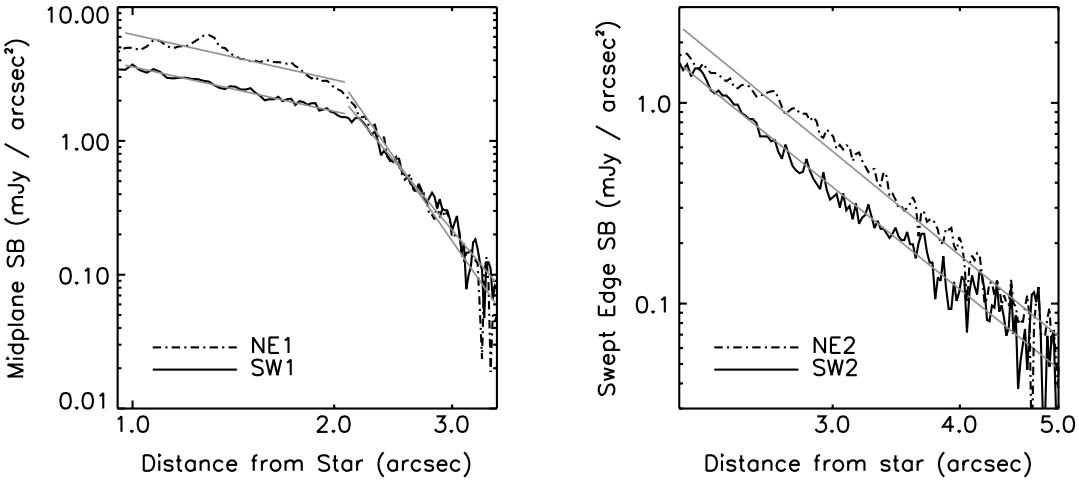

Figure 5.5 Surface brightness profiles through the disk midplane (left) and the outer edge of the swept back component (right). The cuts are one pixel wide, and the components listed in the legends are labeled in Figure 5.2. The directions for the cuts are taken from the position angles derived in §3.1.2 and 3.1.3. The power law fits described in the text are overplotted in grey. The data show a pronounced brightness asymmetry between the northeast and southwest disk lobes.

One-dimensional surface brightness profiles

One-dimensional surface brightness profiles through the disk midplane (components NE1 and SW1 in Figure 5.2; PA = 70.7 deg) and along the swept component outer edge (components NE2 and SW2 in Figure 5.2; PA = 82.8 deg, 65.1 deg) are shown in Figure 5.5. The midplane surface brightness follows a broken power law. The fitted power law indices between 0.9″ and 2.1″ are -1.1 ± 0.1 for both midplane disk lobes. Between 2.1″ and 3.5″, power law fits give indices of -7.2 ± 0.3 for component NE1 and -6.0 ± 0.2 for component SW1. Breaks in the scattered-light surface brightness of debris disks are often taken as the location of the parent body population for the scattering grains (e.g., Strubbe & Chiang 2006). However, as the midplane break approximately coincides with the position at which the outer edge of the swept component intersects the disk, this standard interpretation may not hold for this case.

The surface brightness profile for the outer edge of the swept component is well represented by a single power-law (Figure 5.5). The fitted power law index is -4.1 ± 0.1 for both NE2 and SW2. The listed errors for the power law fits in this section are formal fitting errors and should be treated as lower limits to the true uncertainties.

5.3.2 ACS+NICMOS

Disk Scattered Light Colors

We computed the color of the disk by rebinning the ACS Stokes I image to the same pixel resolution as the NICMOS image ($0.0759''$). We then convolved the binned ACS image with a coronagraphically unocculted field star (the approximate NICMOS PSF) and performed the corresponding operation on the NICMOS image. Finally, we divided each image by the stellar flux density of HD 61005 at the appropriate band-center effective wavelength before dividing the NICMOS image by the ACS image.

Figure 5.6 illustrates that the HD 61005 debris disk appears predominantly blue with no significant systematic color gradient. The mean intensity ratio inferred from Figure 5.6 is 0.32 ± 0.10 (corresponding to a color index of [F606W]$-$[F110W] $= -1.2 \pm 0.3$), where the error is dominated by uncertainties in the PSF subtraction. Although comparing images of different resolution can result in systematic color errors (e.g., Golimowski et al. 2006), our convolution steps appear to have a small effect; the mean color neglecting convolution is within 1σ of that found including convolution.

The blue color inferred from Figure 5.6 (ratio < 1) is rare, as the handful of debris disks with color measurements to date show mainly red colors (Meyer et al. 2007, and references therein). There are several notable exceptions, however. The HD 32297 and HD 15115 debris disks, for example, have been suggested to show blue optical to near-infrared scattered light colors (Kalas 2005; Kalas et al. 2007), though the result for HD 32297 is currently under debate (Debes et al. 2009). Interestingly, both disks have morphological features consistent with ISM interaction. HD 32297 shows a bowed disk structure, similar to HD 61005, though on a much larger scale ($\sim$ 1000 AU; Kalas et al. 2005). HD 15115 is highly asymmetric, perhaps as the result of ISM erosion (Debes et al. 2009).

The M dwarf debris disk, AU Mic, which has a similar polarization structure to HD 61005 (§3.1.2), also shows blue optical to near-infrared colors, with a color gradient towards bluer colors at larger radial distances, indicating changes in the grain size distribution (Strubbe & Chiang 2006; Fitzgerald et al. 2007a). The global [F606W]$-$[F110W] color of the HD 61005 disk is comparable to the [F606W]$-J$ AU Mic disk color at projected radii within ~ 40 AU, the approximate location of the parent body ring in this system (Fitzgerald et al. 2007a).

Like AU Mic, the blue color of the HD 61005 disk is likely due to the disk grain size distribution. Scattered light images afford a relatively narrow window on the grain size population because the brightness at a given location in the disk is largely determined by the product of the grain size distribution and the grain scattering cross section. In the presence of a steep size spectrum characteristic of a collisional cascade, this product is strongly peaked near $x \equiv \frac{2\pi a}{\lambda} \sim 1$. For example, for the Dohnanyi spectrum with $dn/da \propto a^{-7/2}$ (Dohnanyi 1969), this peak occurs at $x \simeq 2 - 6$, depending on the optical properties of the grain material. In Figure 5.7, a Mie calculation shows the peak for water ice and astronomical silicates at $0.6\,\mu$m and $1.1\,\mu$m as a function of grain size. The plots illustrate that the HD 61005 NICMOS images trace grains with radii of order $0.2 - 2\,\mu$m, while the ACS images

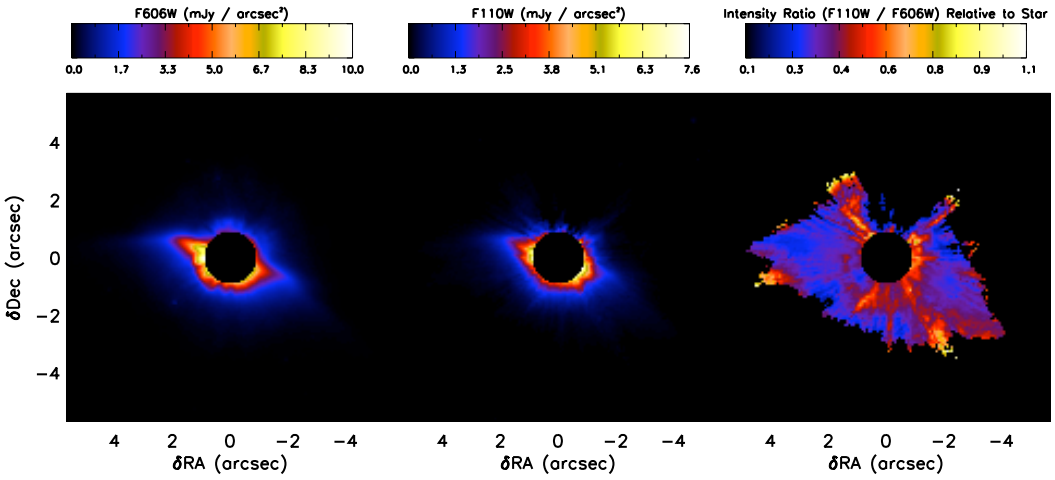

Figure 5.6 ACS and NICMOS images processed to compute the grain color. The left panel displays the ACS image binned to the NICMOS pixel resolution and convolved with the NICMOS off-spot PSF. The middle panel displays the NICMOS image convolved with the ACS PSF. The right panel shows a masked ratio image of the left and middle images divided by the stellar flux density ratio; values less than unity represent grains that preferentially scatter blue light, whereas values greater than unity represent grains that preferentially scatter red light. In the ratio image, we have applied a mask to all pixels with values less than 2.5 times the background level in either original image. The ratio image indicates that the disk appears predominantly blue with no appreciable color gradient.

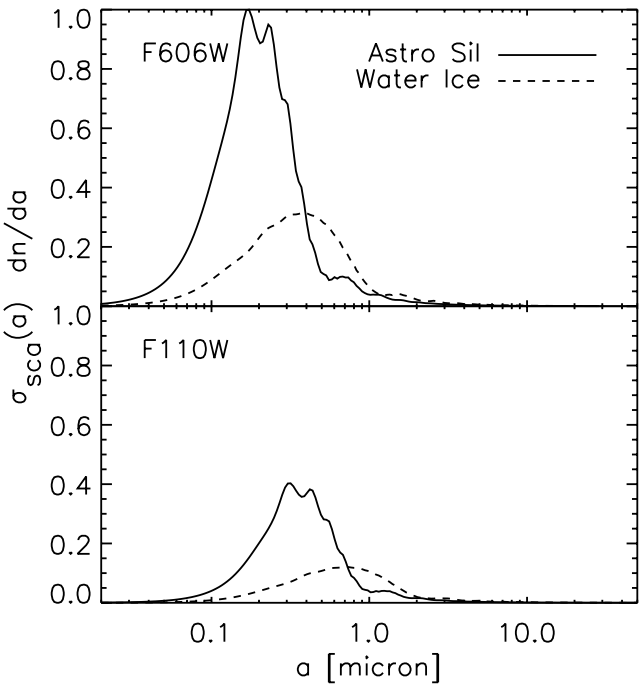

Figure 5.7 Product of the scattering cross section and a Dohnanyi size spectrum as a function of logarithmic grains radius for spherical particles. At a given wavelength, this product largely determines the surface brightness at a particular location in the disk. Assuming a steep size spectrum (e.g., Dohnanyi), a large peak is observed near $x \sim 1$. Thus a given scattered light image traces a relatively narrow window of the grain size population. The HD 61005 disk is globally brighter at optical wavelengths than near-infrared wavelengths, likely reflecting the larger number of grains at increasingly small sizes. The above results are monochromatic: $\lambda_{\rm F606W} = 0.6$ μm and $\lambda_{\rm F110W} = 1.1$ μm.

trace systematically smaller grains with radii of order $0.1 - 1\,\mu$m. Thus the observation that HD 61005 is globally brighter at optical wavelengths than near-infrared wavelengths suggests the disk contains a larger number of grains at increasingly small sizes, consistent with our expectation of a steep size spectrum.

The inference that the F606W ACS images trace predominantly sub-micron sized grains is also consistent with the imaging polarimetry results (§3.1). The large polarization fraction and electric field orientation perpendicular to the edge-on midplane are in qualitative agreement with the expected signature of scattering by small spherical particles with $x \lesssim 1$ (Kruegel 2003). For larger spherical grains, the electric field orientation can rotate by 90° at certain scattering angles, resulting in an orientation parallel to the edge-on midplane. Furthermore, any line of sight comprising emission from a range of scattering angles will tend to

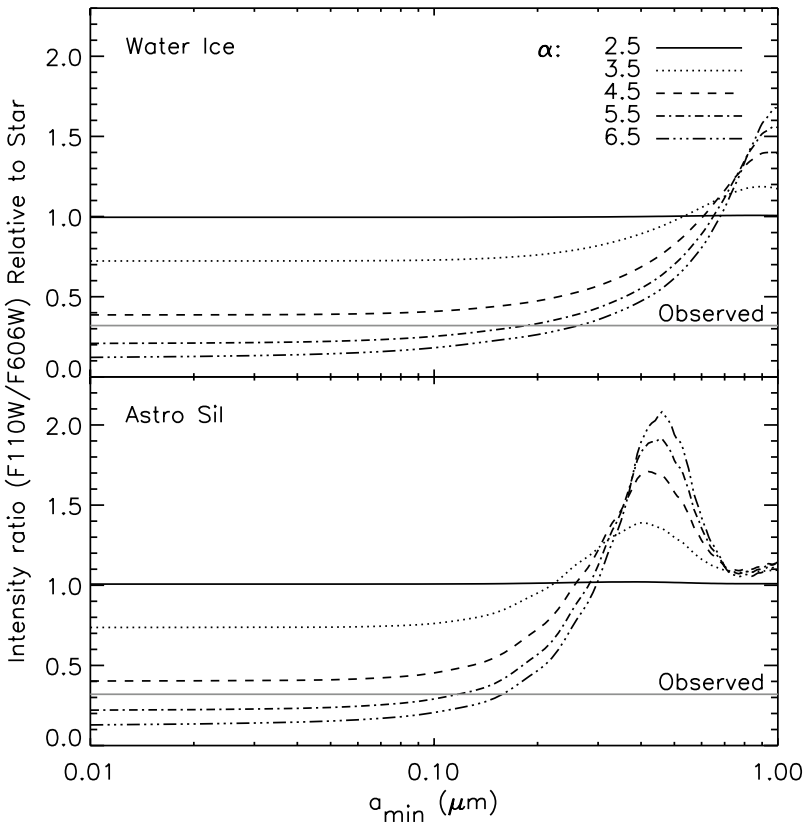

Figure 5.8 Implied disk colors for ice and silicate grains for grain size distributions of the form: $dn/da \propto a^{-\alpha}$, where $a_{\rm min} < a < 1$ mm. The data place an upper limit on the minimum grain size ($a_{\rm min} \lesssim 0.3$ μm) and suggest a global size distribution steeper than the canonical Dohnanyi size spectrum ($\alpha = 3.5$).

show weak linear polarization (Graham et al. 2007). Neither of these features is consistent with the HD 61005 polarization results.

By integrating the curves in Figure 5.7 and comparing the results to the measured color, we can constrain the size distribution. The results of this procedure are shown in Figure 5.8, which shows the implied color for ice and silicate grains for grain size distributions of the form: $dn/da \propto a^{-\alpha}$, where $a_{\rm min} < a < 1$ mm. A range of minimum grain sizes are considered, as radiation pressure could potentially remove a fraction of small grains from the system (Appendix A). The data place an upper limit on the minimum grain size: $a_{\rm min} \lesssim 0.3$ μm. Figure 5.8 also suggests the global size distribution is steeper than the Dohnanyi spectrum: $\alpha \sim 4.5 - 5.5$. This slope is consistent with results from collisional equilibrium modeling of other debris disk systems (e.g., Strubbe & Chiang 2006). However, the applicability of these models to the unique HD 61005 system is presently uncertain.

Astrometric test for low-mass companions

The ACS and NICMOS images contain four field stars in common to both data sets, roughly offset from HD 61005 in RA and Dec by [-2.4″, 9.4″], [-8.6″, 0.0″], [-12.8″, 3.5″], and [-14.0″, 2.4″]. As the ACS and first-epoch NICMOS images were obtained 1.1 years apart, we can measure the field star proper motions to investigate whether any of these stars are likely companions to HD 61005. The annular proper motion of HD 61005 is $\mu_\alpha = -56.09$ mas yr^{-1} in right ascension and $\mu_\delta = 74.53$ mas yr^{-1} in declination (Perryman et al. 1997). Thus comoving companions are expected to show a 102.61 mas displacement between the two epochs of observation.

To derive the NICMOS stellar positions, we first calculated stellar centroid positions on the image frames uncorrected for geometric distortion using the apphot *center* task, as described in Cox et al. (1997). We then applied a distortion correction to the raw positions using the correction coefficients appropriate for Cycle 15 data, given in the NICMOS data handbook (version 7.0). The reported rms astrometric uncertainty from applying previously derived distortion corrections to early commissioning data is 13.6 mas (Cox et al. 1997). Data obtained more recently yield similar results (e.g., Schneider et al. 2006).

The geometric distortion for the ACS data requires a low spatial frequency correction for the optical telescope assembly (OTA) and ACS optics, and two high frequency corrections for the given wide band filter and polarizing filter (Anderson & King 2004; Kozhurina-Platais & Biretta 2004). Following Kozhurina-Platais & Biretta (2004), we first used the effective PSF library and fitting technique of Anderson & King (2000) to derive raw positions for the field stars from the flat-fielded images ($*\_flt.fits$) observed through the POL0V filter. We next applied the solution derived by Anderson & King (2004) to obtain stellar positions corrected for the low frequency OTA distortion and the high frequency F606W filter distortion. Finally, we applied a further correction for the distortion introduced by the POL0V filter, using the solution derived by Kozhurina-Platais & Biretta (2004). The reported rms precision derived from applying this method to commissioning data is 1 mas (Kozhurina-Platais & Biretta 2004).

To test for possible companionship, we performed relative astrometry by adopting one star's position as a fixed reference point and calculating the relative proper motion for the remaining three stars. We repeated this procedure three times, using each field star as the reference. No systematic motion for any of the field stars is observed; all relative proper motions are less than twice the approximate expected rms positional accuracy ($\sigma =$ 13.6 mas). We note that although the distortion solutions employed only strictly apply to noncoronagraphic, direct imaging data, the small measured astrometric offsets suggest the additional field distortions imposed by the coronagraphic optics are negligible in this case. Given that the annual proper motion of HD 61005 is significantly greater than the measured astrometric motions of all field stars, we conclude that unless all four sources are companions, the four field stars are background objects.

5.4 Interpretation

The results presented in H07 and the previous section strongly suggest that HD 61005 is a near edge-on debris disk, undergoing significant erosion by the ambient interstellar medium. In this section, we explore whether interaction between the disk and local interstellar gas can plausibly explain the observed swept, asymmetric morphology.

5.4.1 Interaction with a Cold, Dense Cloud

Ram pressure stripping of bound grains

In their discovery paper, H07 suggested that interaction with a cold ($T \sim 20$ K), dense ($n \sim 100$ cm^{-3}) cloud could potentially explain the HD 61005 morphology. In such a cloud, ram pressure on disk grains from interstellar gas could unbind grains from the system, analogous to the process that strips gas from cluster galaxies (Gunn & Gott 1972; van Gorkom 2004).

For ram pressure stripping to operate, the drag force on a grain must be comparable to or greater than the gravitational force binding the grain to the star. For a grain of radius $a_{\rm grain}$ and density $\rho_{\rm grain}$ orbiting at distance r from a star of mass $M_{\rm star}$[1], the interstellar cloud density n and relative cloud-disk velocity v must obey:

$$\left(\frac{n}{200\,{\rm cm}^{-3}}\right)\left(\frac{v}{30\,{\rm km\,s}^{-1}}\right)^2 \gtrsim \left(\frac{M_{\rm star}}{0.95\,M_\odot}\right)\left(\frac{a_{\rm grain}}{0.1\,\mu{\rm m}}\right)\left(\frac{\rho_{\rm grain}}{2\,{\rm g\,cm}^{-3}}\right)\left(\frac{70\,{\rm AU}}{r}\right)^2. \quad (5.1)$$

This required density is characteristic of cold, dense gas, the existence of which is constrained in §4.1.3. In such a high-density cloud, H07 argued that Bondi-Hoyle-Lyttleton (BHL) accretion could also potentially play a role, leading to an accumulation of interstellar grains that contribute non-negligibly to the observed infrared excess emission and scattered light morphology.

Ram pressure deflection of unbound grains

Recently, Debes et al. (2009) suggested that ram pressure deflection of unbound grains could plausibly shape several previously resolved debris disks, including HD 61005. Their model does not specify the origin of the unbound population. However, such a substantial population of unbound grains are unlikely to be produced in a steady state situation, as collisional equilibrium models predict that the scattered light surface brightness due to bound grains dominates over that from grains unbound by radiation pressure (Krivov et al. 2006;

[1]Throughout this paper, we adopt $M_{\rm star} = 0.95 M_\odot$, based on the pre-main-sequence evolutionary tracks of D'Antona & Mazzitelli (1997) and Baraffe et al. (1998) and the FEPS age estimate reported by H07 (E. Mamejek, private communication).

Strubbe & Chiang 2006). Furthermore, for the case of HD 61005, radiation pressure from the low luminosity star may be insufficient to unbind grains of any size (Appendix A).

Let us nonetheless suppose that a substantial unbound grain population exists. The ambient ISM density needed to deflect such grains by the distances implied by our observations is similar to that required to strip bound grains (§5.4.1). Both scenarios require densities characteristic of cold, dense clouds. For $\beta = 1$ grains launched from parent bodies on circular orbits at 70 AU, the required interstellar cloud density and relative velocity obey[2]:

$$\left(\frac{n}{100\,\mathrm{cm}^{-3}}\right)\left(\frac{v}{20\,\mathrm{km\,s}^{-1}}\right)^2 \gtrsim \left(\frac{M_{\mathrm{star}}}{0.95\,M_\odot}\right)\left(\frac{a_{\mathrm{grain}}}{0.1\,\mu\mathrm{m}}\right)\left(\frac{\rho_{\mathrm{grain}}}{2\,\mathrm{g\,cm}^{-3}}\right)\left(\frac{70\,\mathrm{AU}}{r}\right)\left(\frac{y/x}{0.2}\right)\left(\frac{110\,\mathrm{AU}}{x}\right). \quad (5.2)$$

Here x and y, respectively, are the relative distances traveled by the grain parallel and perpendicular to the disk midplane at a given time after the grain is born. We adopt $x \sim 110$ AU and $y \sim 20$ AU, the approximate positions of the outermost binned polarization vectors in Figure 5.1.

Limits on cold, dense interstellar gas

The explanations of §5.4.1 and §5.4.1 are hampered by two factors. First, in both circumstances, escaping grains leave the system on orbital timescales ($10^2 - 10^3$ yr). These timescales are shorter than the timescale over which the disk is expected to be collisionally replenished with sub-micron sized grains ($\gtrsim 10^4$ yr; see Appendix B). Thus both scenarios require that we are observing HD 61005 during a short-lived period in its history.

Second, cold neutral medium (CNM) clouds within the Local Bubble are extremely rare, occupying a volumetric filling factor of $\ll 1\%$ (Welsh et al. 1994). To date, only one cloud with properties typical of CNM clouds ($n \sim 50$ cm^{-3}, $T \sim 20$ K, $V = 4.9 \times 1.4 \times 0.07$ pc^3) is known within the Local Bubble ($d < 45$ pc, towards 3C 225; Heiles et al. 2003; Meyer et al. 2006; Meyer 2007). Furthermore, in contrast to optical stellar spectra towards this known cloud, our optical spectrum of HD 61005 does not show evidence of an analogous CNM cloud. This finding is illustrated in Figure 5.9, which shows spectra of HD 61005 and two comparison late-type G stars (HD 33822, HD 13836) in the Na I D lines (D_2: 5889.95 Å, D_1: 5895.92 Å). HD 61005 is a relatively young star with a detected rotational velocity ($V \sin i = 9$ km s^{-1}; Holmberg et al. 2008). Thus for direct comparison purposes, we have convolved the spectra of both HD 33822 and HD 13836 with a Gaussian of this width. In Figure 5.9, we have also effectively removed the stellar Doppler shift of the comparison star

[2]Note that equations 5.1 and 5.2 assume the cross section grains present to interstellar gas equals the geometric cross section; calculations performed using ballistic cluster-cluster aggregates and ballistic particle-cluster aggregates suggest this assumption is good to within an order of magnitude (Minato et al. 2006).

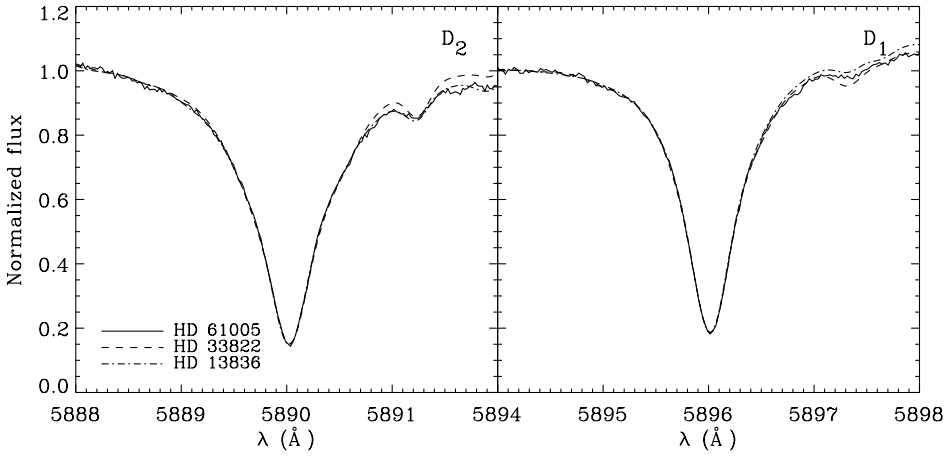

Figure 5.9 Optical spectrum of HD 61005 and two comparison late-type G star spectra in the Na I D lines. The Na I lines in HD 61005 are very similar to the comparison star lines. No narrow absorption component expected for an intervening dense cold interstellar cloud is observed, placing limits on the potential effectiveness of ram pressure stripping of bound grains and deflection of unbound grains in the HD 61005 system.

spectra by cross-correlating each spectrum with the HD 61005 spectrum and shifting it by the appropriate amount.

Figure 5.9 shows that the HD 61005 spectrum is very similar to the late-G comparison star spectra in the Na I lines. No narrow absorption component, characteristic of the known CNM Local Bubble cloud towards 3C 225, is observed (see Figure 1 in Meyer 2007). The corresponding 2σ upper limit to the Na I gas column is $\log(N_{\rm NaI}/{\rm cm}^{-2}) \lesssim 10.6$, based on the continuum signal-to-noise ratio (S/N $\sim$ 100), the instrumental resolution (R $\sim$ 60,000), a linewidth characteristic of the nearby cold cloud towards 3C 225 ($b = 0.54$ km s^{-1}), and assuming the linear regime of the curve of growth. This upper limit translates into a total hydrogen column of $\log(N_{\rm HI+H_2}/{\rm cm}^{-2}) \lesssim 19.0$, employing the sodium-hydrogen conversion relation derived by Ferlet et al. (1985). The scatter in this relation is such that a third of measured hydrogen columns deviate from their predicted columns by factors of a few (Wakker & Mathis 2000). Taking this into account, our predicted hydrogen upper limit is still well below the columns expected for CNM clouds ($10^{20} - 10^{21}$ cm^{-2}; McKee & Ostriker 1977) and also below the mean column density of Na I detected towards 3C 225: $\langle \log(N_{\rm NaI}/{\rm cm}^{-2}) \rangle = 11.7$ (Meyer et al. 2006).

There are a few examples of tiny ($\lesssim$ 1000 AU) low column density ($\log(N_{\rm HI+H_2}/{\rm cm}^{-2}) \lesssim 19.0$) cold clouds in the literature (e.g., Heiles 1997, Stanimirovic & Heiles 2005). These clouds constitute $\lesssim 2-4\%$ of the total neutral hydrogen column along the lines of sight in which they are detected. The precise frequency of these clouds is not well constrained by

large-scale surveys, as their low columns are similar to survey detection thresholds ($\sim 10^{18}$ cm^{-2}; Heiles & Troland 2005). However, an upper limit to their frequency can be obtained by noting that $\gtrsim 5$ such clouds along a typical line of sight would lead to their systematic detection in large-scale surveys (C. Heiles, private communication). Thus within the Local Bubble (d $\lesssim$ 100 pc), these tiny, dense clouds occupy $\lesssim 0.025\%$ of the distance along a typical line of sight. At present, only two dozen debris disks have been spatially resolved. Therefore it seems unlikely that we have already imaged a debris disk residing in one of these clouds. Interaction with a cold, dense cloud is thus an unsatisfactory explanation for the swept morphology observed in HD 61005.

5.4.2 Interaction with a Warm, Low-Density Cloud

Given that disk interaction with a cold, dense cloud appears unlikely, we explore in this section whether interaction with a warm, low-density cloud can potentially explain the observed morphology.

Ram pressure stripping of disk gas and entrainment of disk grains

Warm ($T \sim 7000$ K) interstellar clouds dominate the mass of the local interstellar medium (e.g., Frisch 2004) and occupy a local volume filling factor of $\sim$5.5%$-$19% (Redfield & Linsky 2008). Our optical spectrum does not constrain the presence of such a cloud towards HD 61005, as typical columns towards these clouds are $N_{\rm HI} \sim 10^{17}$ cm^{-2} (Redfield 2006).

The low densities of warm local clouds are insufficient to supply a ram pressure force comparable to the gravitational force and thereby directly unbind grains from the system. For typical parameters of warm local interstellar clouds ($n_{\rm HI} = 0.2$ cm^{-3}, $v_{\rm rel} = 25$ km s^{-1}; Redfield 2006) and 0.1 μm disk grains, the ram pressure stripping radius is $\sim 10^3$ AU (Equation 1), much larger than the radius of the observed bow structure ($\sim 2'' = 69$ AU).

However, in principle, ram pressure stripping could still play a role if the HD 61005 disk contains gas that is undergoing ram pressure stripping by the ISM. In this scenario—in contradistinction to the direct ram pressure stripping scenario outlined in §5.4.1—disk grains are swept away by the interstellar flow only because they are entrained in outflowing disk gas. Gas-gas interactions correctly explain the HI morphologies of galaxies travelling through an intracluster medium (van Gorkom 2004); the truncated, swept-back HI disks of galaxies strongly resemble HD 61005 (e.g., see Figures 1.7 and 1.8 of van Gorkom 2004). We show below, however, that this interpretation for HD 61005 is incorrect because the requirement on the density of disk gas is incompatible with the requirement that grains be entrained.

To unbind disk gas, the ISM ram pressure must exceed the gravitational force per unit disk area:

$$n\mu v^2 \gtrsim GM_{\rm star}\sigma/r^2 \tag{5.3}$$

where $\mu \approx 2 \times 10^{-24}$ g is the mean molecular weight of the ISM and σ is the surface mass density of disk gas. For parameters appropriate to a warm cloud (Redfield 2006), all disk

gas having a surface density

$$\sigma \lesssim 4 \times 10^{-8} \left(\frac{r}{100\,\mathrm{AU}}\right)^2 \left(\frac{0.95\,M_\odot}{M_{\mathrm{star}}}\right) \left(\frac{n}{0.2\,\mathrm{cm}^{-3}}\right) \left(\frac{v}{25\,\mathrm{km\,s}^{-1}}\right)^2 \mathrm{g\,cm}^{-2} \tag{5.4}$$

is swept away by the ISM. The circumstellar gas content of HD 61005 is unknown.

For unbound disk gas to entrain disk grains, the momentum stopping time of a grain in gas cannot be much longer than the outflow timescale, $1/\Omega$, over which marginally unbound gas departs the system, where Ω is the Kepler orbital frequency. From Weidenschilling (1977), the momentum stopping time of a grain in rarefied gas is given by the Epstein (free molecular drag) law as

$$t_{\mathrm{stop}} \sim \frac{1}{\Omega}\frac{a_{\mathrm{grain}}\rho_{\mathrm{grain}}}{\sigma} \sim \frac{500}{\Omega} \left(\frac{a_{\mathrm{grain}}}{0.1\,\mu\mathrm{m}}\right) \left(\frac{\rho_{\mathrm{grain}}}{2\,\mathrm{g\,cm}^{-3}}\right) \left(\frac{4 \times 10^{-8}\,\mathrm{g\,cm}^{-2}}{\sigma}\right) \tag{5.5}$$

which is too long compared to the outflow time. Thus we discount the possibility that the observed disk morphology arises from ram pressure stripping of disk gas.

Secular perturbations to grain orbits induced by ram pressure

The direct ram pressure stripping scenario described in §5.4.1 requires that the ISM ram pressure force on disk grains be comparable to the stellar gravitational force. As shown in §5.4.2, this condition is not met in low-density warm clouds, for which $F_{\mathrm{ram}}/F_{\mathrm{grav}} \sim 10^{-3}$ (at ~ 70 AU; see Equation 1). However, even in the case when the force exerted by interstellar gas is much less than the gravitational force, neutral gas can introduce secular perturbations to bound grain orbits that could significantly change the morphology of the disk over timescales of $\sim 10^3 - 10^4$ yr, assuming sub-micron sized grains dominate the scattered-light distribution. This perturbation timescale is less than the crossing time of local warm clouds: $t_{\mathrm{cross}} \sim (L_{\mathrm{cloud}}\,/\,5\,\mathrm{pc})/(v_{\mathrm{rel}}\,/\,25\,\mathrm{km\,s}^{-1}) \sim 10^5$ yr (Redfield 2006). Thus this mechanism can plausibly explain the disturbed HD 61005 morphology. Interestingly, this scenario has been proposed as the primary removal mechanism for dust in our own solar system at 20−100 AU (Scherer 2000), though at present, little empirical evidence is available to test this theory.

As described in Scherer (2000), the underlying physical process responsible for neutral gas drag is similar to that responsible for solar wind drag. In both cases, momentum transfer from incident protons or gas particles to the grain surface results in secular perturbations to the grain's initial orbit. However, the monodirectional character of the interstellar gas drag force leads to changes in particle orbits that are very different from those induced by the solar wind. While the solar wind and Poynting-Robertson drag both act to reduce grain

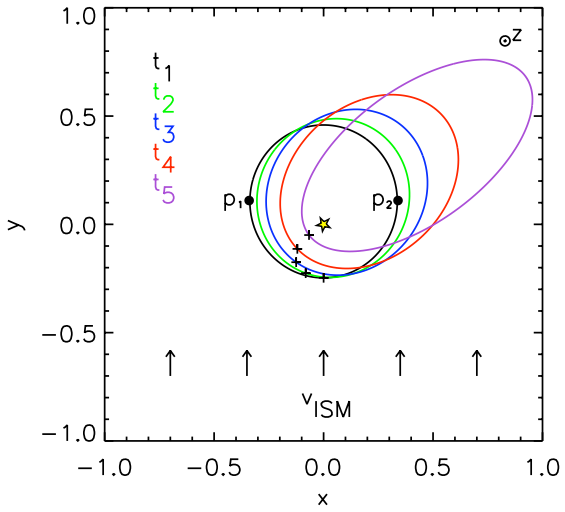

Figure 5.10 Orbital evolution of a test particle in the $x-y$ plane under the effect of neutral gas drag. Five time periods separated by a fixed number of orbits are shown. The grain begins with its star-pericenter (Runge-Lenz) vector anti-aligned with the incoming interstellar flow, directed along the positive $y-$axis, and its angular momentum vector aligned with the $z-$axis (out of the page). The ISM flow decelerates the grain on one leg (e.g., point p_1) and accelerates it on the other (e.g., point p_2), causing the Runge-Lenz vector to rotate. The grain's periastron at each successive time is shown by a cross to illustrate this effect.

eccentricities and semi-major axes, interstellar gas drag tends to increase them, eventually unbinding the grains from the system.

In the absence of other perturbing forces, the analytic work of Scherer (2000) shows that the gas drag force acts to rotate a given particle's orbital plane into a plane coplanar to the flow vector, and its star-pericenter (Runge-Lenz) vector into a direction perpendicular to the flow vector. These effects are illustrated in Figures 5.10 and 5.11, which show the orbital evolution of two dust grains with different initial orbital elements. The grain in Figure 5.10 starts on a low-eccentricity ($e = 0.3$) orbit in the $x-y$ plane with its Runge-Lenz vector anti-aligned with the incoming interstellar flow and its angular momentum vector aligned with the $z-$axis (out of the page). This orientation causes the grain to be decelerated on one leg (e.g., point p_1) and accelerated on the other (e.g., point p_2), causing the Runge-Lenz vector to rotate. The grain's periastron at each successive time is denoted by a cross to highlight this effect. The rotation continues until the Runge-Lenz vector becomes perpendicular to the incoming flow. Thus, counterintuitively, neutral gas drag leads to a build up of grains perpendicular to the relative flow direction.

The tendency of neutral gas drag to rotate a given grain's orbital plane into a direction coplanar with the incoming flow is illustrated in Figure 5.11, which shows the evolution of a low-eccentricity ($e = 0.1$) grain initially inclined 80° with respect to the ISM flow. The

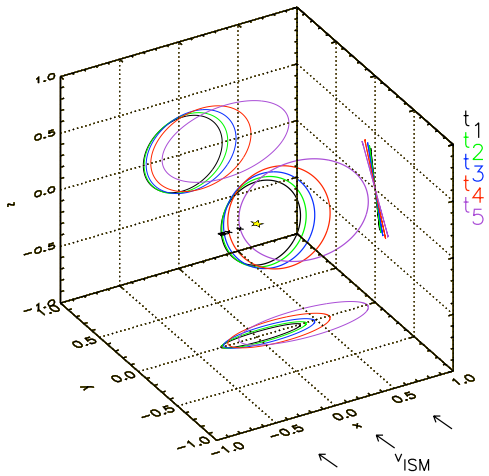

Figure 5.11 Orbital evolution due to neutral gas drag of a test particle initially inclined by 80° with respect to the incoming flow. Five time periods separated by a fixed number of orbits are shown. The grain's initial Runge-Lenz vector is chosen to be at its equilibrium orientation. The ISM flow exerts a net torque on the orbiting grain, causing the angular momentum vector to rotate into a direction perpendicular to the ISM flow.

grain's initial Runge-Lenz vector is chosen to be at its equilibrium orientation (perpendicular to the flow) to isolate the effect of the orbital plane rotation. The ISM flow exerts a net torque on the orbiting grain, causing the angular momentum vector to rotate into a direction perpendicular to the incoming flow. This effect is easiest to discern from the two-dimensional projection of the $y - z$ plane in Figure 5.11.

The above discussion suggests that rigorously modeling the neutral gas drag effect requires knowledge of the initial grain orbital elements and the interstellar gas flow. However, for the case of HD 61005, neither of these prerequisites is known. HD 61005 has a well-determined space motion; the Hipparcos-measured proper motion corresponds to a plane-of-sky velocity of $v_\alpha = 9.2 \pm 0.3$ km s^{-1}, $v_\delta = 12.2 \pm 0.4$ km s^{-1} at the distance of HD 61005. The radial velocity is $v_r = 22.3 \pm 0.2$ km s^{-1} (Nordström et al. 2004). However, the velocity of the putative cloud responsible for the swept morphology is unknown. Velocities of local warm clouds can be comparable to the observed space motion of HD 61005 (Frisch et al. 2002). Thus the red arrow in Figure 3 of H07 denoting the direction of the star's tangential motion is not a reliable indicator of the cloud-star relative velocity.

Unfortunately, HD 61005 is difficult to assign to any known interstellar clouds, owing to its heliocentric distance (34.5 pc) and galactic coordinates ($l = 246.4°, b = -5.6°$). Redfield & Linsky (2008) recently used radial velocity measurements of 157 lines of sight to identify 15 warm clouds in the local interstellar medium. However, the identified clouds are thought to reside largely within 15 pc of the Sun, whereas the distance to HD 61005 is 34.5 pc.

Furthermore, the line of sight to HD 61005 is not assigned to any of these clouds. The star's galactic coordinates could plausibly associate it with either the G cloud or the Blue cloud (e.g., see Figure 19 in Redfield & Linsky 2008), though HD 61005 is more likely associated with a more distant, currently unidentified cloud, rendering the cloud-star relative velocity for this system highly uncertain.

The initial orbital elements prior to the presumed cloud interaction are similarly unknown. The radial architectures of debris disks in scattered light show significant diversity and currently appear largely independent of other observables, such as age or spectral type (Kalas et al. 2006). Furthermore, as discussed in §5.3.1, the one-dimensional surface brightness profiles of HD 61005 do not allow us to place strong constraints on the location of the parent body population, and thus the grain eccentricities and inclinations. We do note, however, that the sub-micron particle sizes implied by the polarization and color measurements do not *a priori* contradict the bound orbits requirement of the gas drag perturbation theory, as radiation pressure from the star is likely insufficient to unbind grains of any size (Appendix A).

Given the large uncertainties in the disk and ambient ISM properties of the HD 61005 system, we are unable to empirically test whether gas drag is responsible for the asymmetric, swept morphology. Therefore to explore whether this mechanism can plausibly explain the observed structure, we adopt the numerical techniques described in Scherer (2000) to construct a modest grid of models with reasonable assumptions for the disk grains and ISM. Details of the model construction and restrictions are described in Appendix B. In summary, we subject a ring of 0.1 μm, low eccentricity ($e = 0.2$) grains with semimajor axes of 60 AU and random inclinations to a uniform density cloud typical of nearby warm interstellar clouds ($n_{\rm HI} = 0.2$ cm^{-3}) traveling at a typical cloud-star relative velocity of $v_{\rm rel} = 25$ km s^{-1} (Redfield 2006). We test a range of relative flow vectors and produce scattered light images from the resultant grain distributions after the system has achieved a steady state.

The resulting grid of models produced for a range of relative flow directions and disk inclinations is presented in Figures 5.12 − 5.14. Each frame is 9″ across, and the color scale is logarithmic. The adopted coordinate system is described in Appendix B. A comparison of Figure 5.1 to Figures 5.12 − 5.14 suggests that none of the IS gas drag models are a striking match to the data. On the other hand, a gross swept morphology, somewhat similar to HD 61005, is present in a few of the model panels. These best approximations correspond to disk inclinations of $i = \pm 80°$, consistent with the data (§3.1.2), and relative flow directions largely coplanar with the disk midplane, approximately in the plane of the sky (Figure 5.12, panels $\theta \sim 0°, 180°$). This relative flow direction is counterintuitive, going against the flow direction suggested by preliminary inspection of the scattered-light images, perhaps providing a further strike the against IS gas drag interpretation. On the other hand, if these preliminary models are a first approximation of the data, then this distinctive relative velocity may be verified by future observations (§5.1).

For ease of viewing, we show in Figure 5.15 the ACS and NICMOS data together with a neutral gas drag model that roughly approximates the observed morphology, corresponding to the top row, third panel of Figure 5.12. A summary of the morphological shortcomings

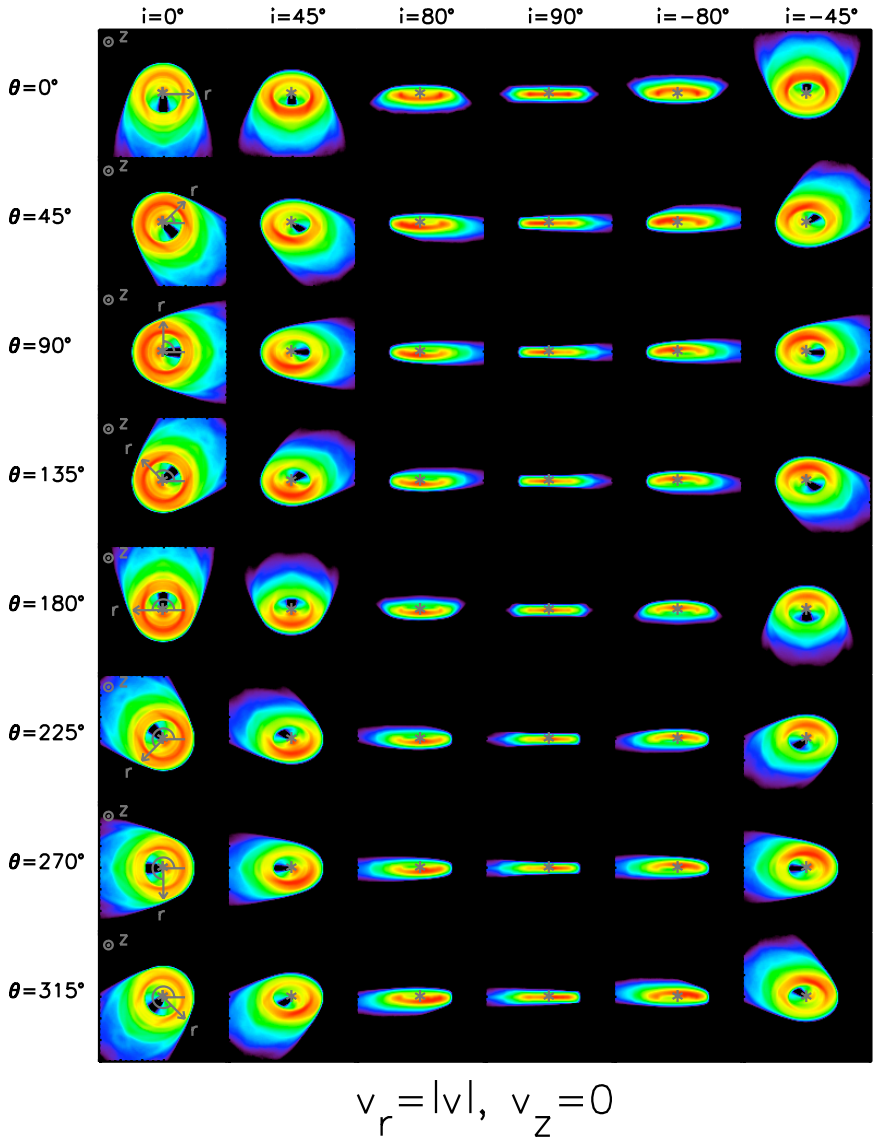

Figure 5.12 Steady state model images for hypothetical debris disk systems undergoing neutral gas perturbations. In all models, the relative flow is coplanar with the disk midplane. The adopted cylindrical coordinate system is shown with respect to the face-on disks in the left column. The vector $\boldsymbol{r}$ points in the direction of the relative ISM flow; the azimuthal orientation of $\boldsymbol{r}$ is defined by θ. The disk inclinations are indicated at top. Each box is $9'' \times 9''$ (assuming a distance to the system of 34.5 pc); the color scale is logarithmic. The models show that brightness asymmetries, bow structures, and swept morphologies can all be produced by disk encounters with warm interstellar clouds, which occupy a sizable fraction of the local ISM.

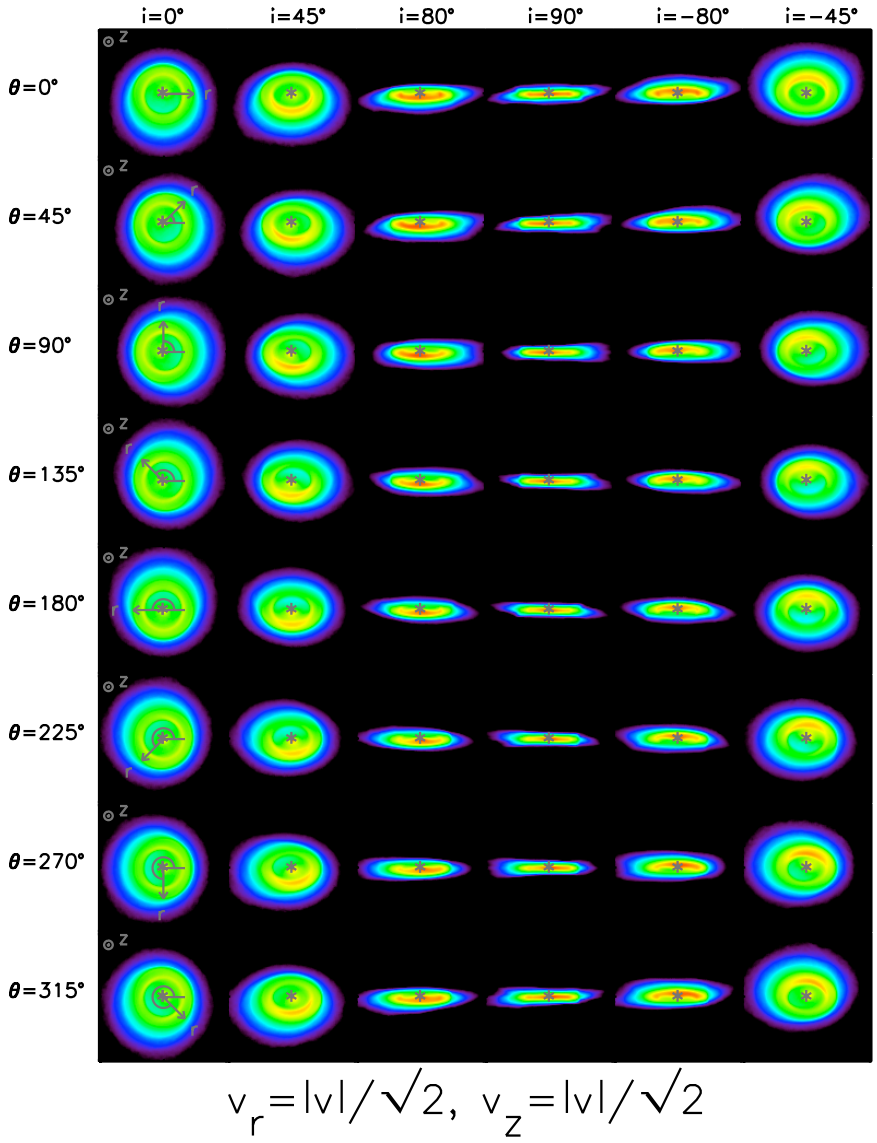

Figure 5.13 Same as Figure 5.12, only with components of the relative flow both coplanar with the disk midplane and perpendicular to it. The radial and perpendicular flow components are equal in magnitude.

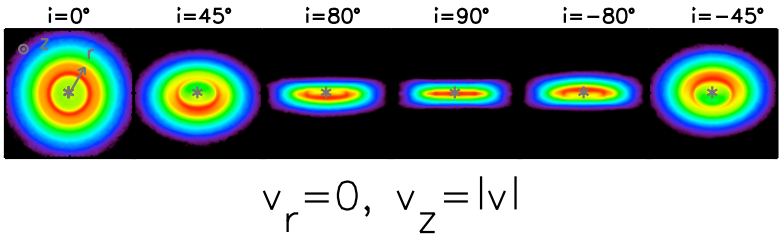

Figure 5.14 Same as Figures 5.12 and 5.13, only with the relative flow vector oriented purely perpendicular to the disk midplane. The dust distribution in these models is largely axisymmetric, as described in the text. The brightness asymmetries evident at intermediate inclinations ($i = 45°, 80°, -80°, -45°$) are the result of scattering asymmetry; for positive inclinations, the lower half of the disk in the image is closer to the observer than the upper half.

of this strongest IS gas drag model can be summarized as follows:

1. The swept back components NE2 and SW2 are much more extended relative to the main disk in the data than in the model.

2. The edges of the swept back structure are more pronounced in the data than in the model.

3. The sharp radial spurs observed beyond the inflection point along components NE1 and SW1 are not present in the model.

4. The model figure does not show the significant brightness asymmetry between the northeast and southwest disk lobes that is seen in the data.

These differences could indicate that the physics incorporated into the current IS gas drag models is overly simplistic (§5.1), or that interstellar gas drag is not responsible for the observed morphology (e.g., §5.3).

As discussed in §3.1, the ACS polarization results can be understood qualitatively through geometric considerations alone. Thus the most promising IS gas drag models naturally reproduce the observed polarization structure.

5.5 Discussion

5.5.1 Interstellar Gas and the HD 61005 Morphology

The previous section explored whether disk/gas interaction can plausibly explain the unusual HD 61005 morphology. Of the four scenarios considered, three are implausible,

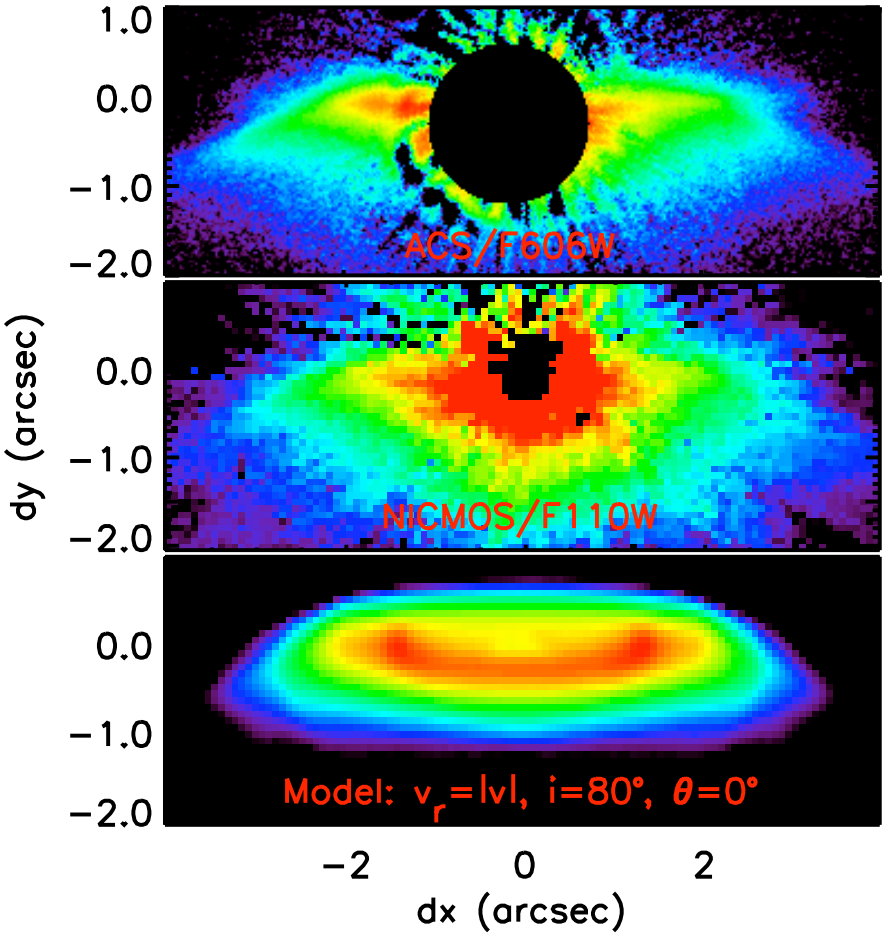

Figure 5.15 Comparison between the ACS Stokes I image (top), the NICMOS 1.1 μm image (middle), and a promising neutral gas model (bottom), taken from Figure 5.12 (top row, third column). This comparison shows that the simple model presented here is only a very rough representation of the data. Still, the gross swept, asymmetric morphology is clearly present in the model image.

given the limits on the ambient interstellar gas density imposed by our optical spectrum. The fourth scenario, secular perturbations from low density gas, is an attractive alternative, as this mechanism can significantly distort grain orbits well within a cloud crossing time. Furthermore, the densities required by this scenario are typical of local interstellar clouds, which occupy up to $\sim 20\%$ of the local ISM.

Nevertheless, our preliminary modeling of this effect (Figures 5.12 − 5.14) can only produce disk morphologies in very rough agreement with the observations, suggesting that either additional physics needs to be incorporated into the current models, or that an altogether distinct physical mechanism is at work. Indeed, the current models are simplistic, and their applicability is limited by several key assumptions:

1. *Astrosphere Sizes:* As discussed by Scherer (2000), the toy models presented in Figure 5.12 − 5.14 require that the disturbed grains be inside the astrospheric termination shock, such that the interstellar gas density and velocity can be approximated as constant. For the case of HD 61005, the termination shock distance is unknown. Furthermore, as HD 61005 is farther away than any star for which a direct astrospheric detection has been made (Wood 2004), the astrosphere size may be difficult to constrain observationally. In general, termination shock distances vary greatly, depending on the ambient ISM and stellar wind conditions (e.g., densities, temperatures, velocities, stellar activity). For the case of the Sun only, the hydrodynamic models of Müller et al. (2006) show that the termination shock distance could easily vary between ~ 10 AU and 500 AU. Observational astrosphere measurements of solar-type stars are consistent with these predictions[3] (Mann et al. 2006, and references therein).

2. *Initial Conditions:* As noted in §4.2.2 and Appendix B, our adopted initial orbital elements for the HD 61005 disk grains prior to the interstellar cloud interaction are highly uncertain, given a lack of information for the grain properties and underlying planetesimal population that collisionally replenishes the observed dust disk. Future long-wavelength observations sensitive to larger grains may be able to place tighter constraints on the distribution of sub-micron grains prior to the interstellar cloud interaction, as the distribution of large grains would likely reflect that of the parent bodies for the sub-micron population. Furthermore, larger grains would not be significantly affected by interstellar gas drag on the same timescale as the sub-micron size grains traced in these observations. The numerical techniques employed here and in Scherer (2000) can be easily revised to accommodate an arbitrary initial disk architecture, provided the orbits are not highly eccentric, such that averaging over one orbit and applying Gauss' method is invalid.

3. *Internal Disk Collisions:* In Appendix B, we estimate to order-of-magnitude that the collision time for submicron grains at $\sim$70 AU is $\sim$5000 yr. This collision time is

[3]On a broader scale, no astrosphere detections have been made for stars earlier than G-type. As a result, the typical effect of astrospheres on IS gas drag in debris disks surrounding A-type stars is difficult to reliably assess.

somewhat longer than the timescale over which our model relaxes to a steady state — essentially the time for gas drag to unbind a grain — given in Appendix B as ∼3000 yr. That the times are comparable supports the assumption of our models that each grain removed by gas drag is collisionally replenished. At the same time, the comparison of timescales underscores a shortcoming of our model — that removal of grains by collisions is ignored. In reality, submicron grains should be removed from the system not only by gas drag, but also by collisions, in roughly equal proportions. We defer to future work a comprehensive study that includes removal by collisions via a collisional cascade.

4. *Planetary Configurations:* Finally, as illustrated by Scherer (2000) (e.g., his Figure 2), the incorporation of planetary orbits can appreciably change the perturbed orbital elements from the case in which only IS gas drag is considered. This caveat is especially important for massive grains, or grains in close proximity to planetary orbits. As a result, the models presented here should be treated with some caution if applied to typical planetary system scales ($\lesssim$ 50 AU; e.g., Kenyon & Bromley 2004). This cautionary point may be particularly important for the case of HD 61005, as the origin of the brightness asymmetry between the northeast and southwest disk lobes (§3.1.1) is unknown. The agreement between the northeast and southwest deflected component position angles (§3.1.3 and Figures 5.1 − 5.2) suggests this asymmetry may originate from a physical mechanism entirely distinct from ISM interaction. If the asymmetry is due to a massive perturber, the disk morphologies produced in Figures 5.12 − 5.14 are likely to be inapplicable. Resolved long wavelength observations sensitive to massive grains are needed to further explore this possibility.

In addition to the above uncertainties, a remaining ambiguity important for future IS gas drag modeling is the velocity of the putative cloud responsible for the HD 61005 morphology. H07 noted that the star's tangential space motion is perpendicular to the disk midplane, in agreement with the relative flow vector suggested by initial inspection of the observed images. However, while assigning the relative flow direction to the star's tangential velocity is appealing, the three scenarios explored in §4 which assume this flow direction were found to be untenable. Furthermore, velocities of local warm clouds can be comparable to the observed space motion of HD 61005 (§4.2.2). As a result, the star's tangential motion is not a reliable indicator of the cloud-star relative velocity.

Future spectroscopic observations may be able to detect the cloud directly (e.g., HST/GO Program 11674; H. Maness, PI), thereby providing key constraints on the ambient ISM density and velocity. Such observations will greatly inform future modeling, as the preliminary interstellar gas drag models presented here suggest a counterintuitive relative motion parallel to the disk midplane, rather than perpendicular to it. Though HD 61005 is difficult to assign to any known interstellar clouds (§4.2.2), its galactic coordinates could plausibly associate it with either the G cloud or the Blue cloud. The space velocities of both of these clouds suggest a relative motion dominated by the radial velocity component. Therefore if

HD 61005 is associated with either of these clouds, the relative motion is inconsistent with all models posited in §4.

5.5.2 General Applicability of Interstellar Gas Drag

The normalcy of the interstellar densities, velocities, and cloud sizes required by the secular perturbation model in §4.2.2 suggests that IS gas drag can be important beyond HD 61005 in shaping debris disk morphologies. Taking the simple models of §4.2.2 and Appendix B at face value, several of the general morphological features produced in Figures 5.12 − 5.14 are consistent with observed disk structures. For example, the extreme brightness asymmetry in HD 15115 (Kalas et al. 2007) may potentially result from interstellar gas drag, though a range of alternative explanations could explain this system as well (e.g., see list in §1). The bow structures seen in some of the face-on models in Figure 5.12 are also reminiscent of the mid-infrared morphology observed around the A star, δ Velorum, which was recently modeled as a purely interstellar dust phenomenon (Gáspár et al. 2008). Finally, the middle panels in Figure 5.13 show that warps, similar to that seen in β Pic (e.g., Mouillet et al. 1997), can in principle be produced for a relatively wide range of flow directions.

However, while IS gas drag can in principle produce commonly observed disk features, the rate at which gas drag is expected to affect the observations remains unclear. Beyond the uncertainties in the model physics described in §5.1, the characteristics of warm, low density clouds are currently uncertain, as detailed knowledge of them is limited to clouds residing predominantly within 15 pc of the Sun (Redfield & Linsky 2008). As a result, our understanding of typical cloud sizes, shapes, and total volumetric filling factor remains rudimentary. A key finding in this area, however, is that a significant fraction of nearby warm clouds appear to exhibit filamentary morphologies, which would limit the average interaction time between a given disk and cloud, likely reducing the rate at which IS gas perturbations produce an observable effect. This concern is particularly important for the case of disks surrounding early-type stars, as grains traced in scattered light tend to be larger in disks surrounding A-type stars than in their later type counterparts, owing to the larger radiation pressure blowout size. As such, the scattered-light morphologies for A-star disks require correspondingly longer cloud-disk interaction times to be noticeably affected. The timescale for a given grain to become unbound under IS gas drag increases approximately as the square root of the grain size (Scherer 2000).

5.5.3 Interstellar Grains and the HD 61005 Morphology

Finally, we note that all models posited in §4 consider only the role of interstellar gas, ignoring the potential effects of interstellar grains. Artymowicz & Clampin (1997) investigated IS sandblasting of debris disks surrounding A stars and found that sandblasting has a negligible effect on the observed structure, as radiation pressure blows out most incoming interstellar grains before they are allowed to intersect the disk. However, under this framework, only grains with $\beta \geq 1$ are ejected. Thus Figure 5.16 shows that radiation pressure

does not protect the HD 61005 disk, as it does in A-stars.

Nevertheless, even if radiation pressure does not protect the disk against sandblasting, the stellar wind might, as only large interstellar grains with sizes greater than a few $\times 0.1\mu$m are allowed to enter astrospheres freely without deflection (Linde & Gombosi 2000). Thus it is likely that interstellar sandblasting can only plausibly compete with interstellar gas drag if the astrosphere is smaller than or comparable to the observed debris disk size (Mann et al. 2006). The size of the HD 61005 astrosphere is unconstrained by present observations. In general, observations and models of astrospheres surrounding solar-type stars show sizes in the range $\sim 10 - 10^3$ AU, depending on the ambient ISM and stellar wind conditions (see discussion in §5.1). Thus with a characteristic disk size of $\lesssim 70$ AU, it is not clear whether typical interstellar grains can intersect the HD 61005 disk.

Detailed modeling of sandblasting is outside the scope of this paper. However, future theoretical work should investigate the effects of sandblasting on debris disks surrounding solar-type stars. Calculations of the ISM density required for sandblasting to eject an observable flux of grains, the disk morphologies produced in this case, and the timescale for which sandblasting can be sustained would significantly aid in differentiating between this explanation and the gas drag models presented here.

5.6 Summary

The morphology and polarization structure of HD 61005 in the HST/ACS data (Figures 5.1 – 5.3) strongly suggest that HD 61005 is a debris disk undergoing significant erosion by the ambient interstellar medium. The physical mechanism responsible for this erosion remains uncertain. Previous work has suggested that HD 61005 may be interacting with an unusually dense cloud. However, our high-resolution optical spectrum argues against this idea, instead suggesting an ambient ISM density typical of local interstellar clouds. Thus the evolutionary state of HD 61005 may represent a commonplace, intermittent stage of debris disk evolution driven by interaction with typical, low-density gas.

With this motivation, we considered the effects of secular perturbations to grain orbits induced by ram pressure in warm, tenuous clouds. This mechanism can significantly distort grain orbits within a typical cloud crossing time and generate structures that very roughly reproduce the HD 61005 images. Future work that incorporates additional, more detailed physics may improve the agreement between the observations and interstellar gas drag models. The theoretical effects of interstellar sandblasting for solar-type stars should also be investigated in greater detail.

Regardless of the interpretation for HD 61005, we expect interstellar gas drag is important at some level in shaping the structure and evolution of planetary debris disks. The frequency with which this effect is important strongly depends on the typical sizes, shapes, velocities, and filling factors of warm interstellar clouds, which have poorly constrained global properties at present. Nevertheless, some morphological features common to nearby resolved debris disks (e.g., brightness asymmetries, warps, and bow structures) can in principle be

produced in this way. A larger sample of spatially resolved debris disks at a wide range of wavelengths and more detailed theoretical work will help eliminate some of these remaining ambiguities.

5.A Appendix: Radiation Pressure and Blow-out

To provide a preliminary assessment of the unbound grain contribution, we compute the radiation pressure force according to Kruegel (2003)[4]:

$$F_{\rm RP} = \int \frac{\pi a^2}{c}(1 - {\rm g}_\nu \omega_\nu) Q_\nu^{\rm ext} F_\nu \, d\nu. \tag{5.6}$$

Here, g_ν is the grain scattering asymmetry, ω_ν is the albedo, and Q_ν^{ext} is extinction cross section in units of the geometric cross section. H07 and Carpenter et al. (2008) showed that the stellar spectral energy distribution of HD 61005 is well-matched by a main-sequence $T_{\rm eff} =$ 5456 K Kurucz model atmosphere. We therefore use their best-fit spectrum in evaluating Eq. (5.6) to interpolate between the data and to extrapolate for the small fraction of missing flux longward of 24 μm and shortward of 0.3 μm.

Figure 5.16 shows the ratio of the radiation pressure to gravitational force, $\beta = F_{\rm RP}/F_{\rm G}$, for spherical particles with scattering properties computed using Mie theory. Results are shown for water ice ($\rho = 1$ g cm^{-3}; Warren 1984) and Draine's astrophysical silicate ($\rho = 3.5$ g cm^{-3}; Draine & Lee 1984). Mie theory radiation pressure calculations for silicate grains have been verified to within factors of a few using results from microwave analog laboratory data, computational Discrete Dipole Approximation (DDA) and T-matrix calculations, and solar system collection experiments (Wehry et al. 2004, Landgraf et al. 1999, and references therein). Solar system calculations performed on non-spherical, ballistic particle-cluster aggregates and ballistic cluster-cluster aggregates also yield similar results to spherical-grain Mie theory calculations (e.g., Fig. 7 Mann et al. 2006, and references therein). For the various porosities shown in Figure 5.16, we used the Maxwell-Garnett rule to compute the approximate dielectric constant for a dilute medium. As applied to debris disk systems, this method has been found to agree well with DDA calculations for aggregate porosities of $P \lesssim 90\%$ (Köhler & Mann 2004).

The calculation in Figure 5.16 does not include the effect of stellar wind pressure, as the stellar wind parameters for HD 61005 are unknown, and the X-ray flux of HD 61005 ($F_X = 4 \times 10^6$; Wichmann et al. 2003) exceeds the maximum value for which the $F_X - \dot{M}_*$ relation of Wood et al. (2005) is reliable. Nevertheless, evaluating Equation 7 from Strubbe & Chiang (2006) in the geometric optics limit, stellar wind pressure is predicted to be over an order of magnitude less significant than radiation pressure, even for mass loss rates approaching $\dot{M}_* \sim 100\,\dot{M}_\odot$, approximately the highest mass loss rate yet observed. Thus the

[4]This expression is equivalent to that given by Köhler & Mann (2004):
$F_{\rm RP} = \int \frac{\pi a^2}{c}[Q_\nu^{\rm abs} + (1 - {\rm g}_\nu) Q_\nu^{\rm sca}] F_\nu \, d\nu$.

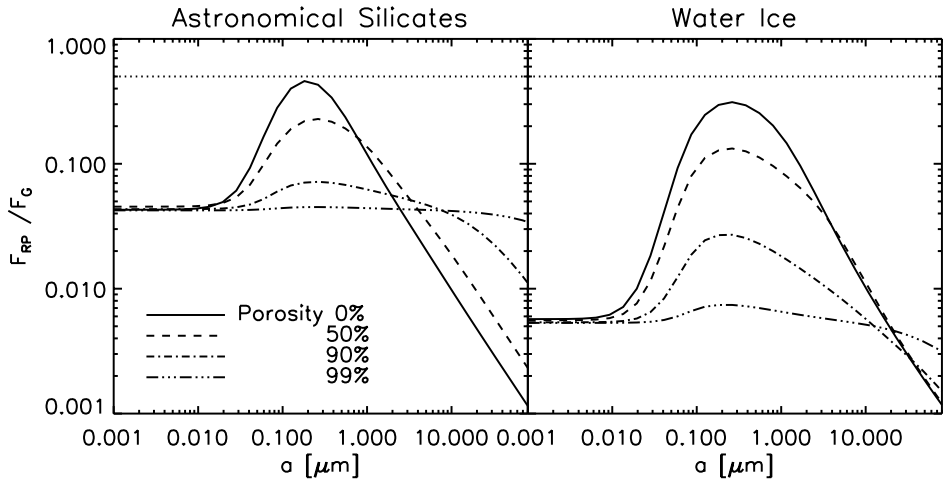

Figure 5.16 Ratio of the radiation pressure force to gravity (β) for astrophysical silicate grains (left) and water ice (right) for the HD 61005 system. The horizontal dotted line indicates the ratio above which grains launched by parent bodies on circular orbits become unbound. Thus silicate and ice grains in a conventional debris disk surrounding a solar type star are likely to remain bound to the star. On the other hand, the weak radiation field ($\beta < 1$) implies that radiation pressure alone does not impede interstellar grains from entering the system. Thus if the astrosphere surrounding HD 61005 is smaller than the disk, interstellar sandblasting could potentially erode the HD 61005 disk grains.

radiation pressure force of Figure 5.16 is expected to be representative of the total outward pressure force, independent of the stellar mass loss rate.

If a grain is liberated from a parent body that is on a circular orbit, radiation pressure increases its eccentricity such that $e = \beta/(1-\beta)$; for $\beta \geq 1/2$, the grain is launched onto an unbound orbit. Debris disk grains tend to be highly porous with vacuum volume filling fractions of $\sim 90\%$ (e.g., Li & Greenberg 1998, Graham et al. 2007). Thus Figure 5.16 shows that silicate and ice grains in a conventional debris disk surrounding a late-G star like HD 61005 are likely to remain bound to the star, unless the parent body population is highly eccentric.

5.B Appendix: Neutral Gas Drag Toy Models

The time for a 0.1 μm grain to become unbound by interstellar gas drag is $\sim 10^3 - 10^4$ years, depending on the ambient ISM density, velocity, and relative flow direction, and the initial orbital elements of the grain (more precise estimates are given later in this section). This timescale may be compared to the collision time for submicron grains. Low eccentricity ($e = 0.1 - 0.2$) grains are pumped to moderate eccentricities ($e = 0.3 - 0.4$) by interstellar gas drag within a typical orbital period of 500 yr. Thus, combining equations 7 and 9 from Chiang et al. (2009) for moderately eccentric grains, the approximate collisional lifetime of submicron sized grains is

$$t_{\rm col} \sim 5000\,{\rm yr}\,\frac{2\times10^{-3}}{L_{\rm IR}/L_*}\,\frac{H/R}{0.1}\sqrt{\frac{\Delta R/R}{0.2}}\left(\frac{0.95\,M_\odot}{M_*}\right)^{1/2}\left(\frac{R}{70\,{\rm AU}}\right)^{3/2}\left(\frac{1-0.4}{1-e}\right)^{3/2}. \quad (5.7)$$

Here, the fractional luminosity, $L_{\rm IR}/L_* = 2\times10^{-3}$, is taken from H07 and is identical to the result obtained from integrating the best fit SED in Roccatagliata et al. (2009). Their fit implies that grains smaller than $\sim 1\,\mu$m are responsible for the bulk of the infrared excess and that these grains reside at a minimum distance of 96 ± 23 AU from the central star. This minimum disk radius is consistent with the characteristic radius of 70 AU adopted in Equation 5.7.

Since the collision time appears comparable to the time for the ISM to remove grains, we assume for our numerical models that a steady state is established in which the collisional generation of submicron grains within the posited birth ring is balanced by their removal by interstellar gas drag. We neglect the depletion of grains by collisions—this amounts to an order-unity error (see also Section 5.1, item 3). Within this framework, we follow the evolution of 10^5 0.1 μm particles. This single grain size is chosen for simplicity and is meant to be representative, given the polarization and color results described in §3. Based on the observed morphology, we choose an initial semimajor axis for all grains of 60 AU. Assuming the observed grains are collisionally created by grains on circular orbits, Appendix A suggests the initial grain eccentricities can range from $e \sim 0$ to $e \sim 0.4$ for 0.1 μm grains, depending on the grain material and porosity. We adopt a representative value of $e = 0.2$ in our models,

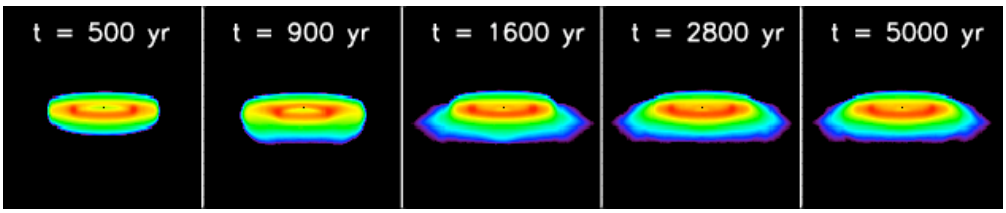

Figure 5.17 Five snapshots of an initially unperturbed, near edge-on disk subjected to interstellar gas drag from a warm, low-density cloud. The model assumes a steady state develops such that each time a grain is lost from the initially unperturbed ring, a new replacement grain is generated within the initial "birth ring." The relative flow direction in this example is coplanar with the disk midplane, and the equilibrated disk is equivalent to the third column in the first row of Figure 5.12. The observed morphology does not change after 3×10^3 years, setting the timescale for which the system is assumed to have achieved steady state.

appropriate for moderately porous silicate grains. This eccentricity is consistent with the fractional ring width adopted in Equation 5.7. We further choose random inclinations drawn from a uniform distribution extending from 0° to 10°, based on an assumed disk aspect ratio of $H/R \sim 0.1$, consistent with the system morphology in Figures 5.1 and 5.2 and with measurements of other highly inclined debris disks (Golimowski et al. 2006; Kalas 2005; Krist et al. 2005). Finally, we assume that the disk is initially circularly symmetric, such that the longitudes of ascending nodes, mean anomalies, and arguments of periastra are uniformly distributed between 0° and 360°.

Having chosen initial orbital elements, we next calculate the secular perturbations to the angular momentum and Runge-Lenz vectors from interstellar gas drag by averaging the Gaussian perturbation equations numerically over one orbit (Brouwer & Clemence 1961). We adopt an ISM density and encounter speed typical of warm interstellar clouds ($n_{\rm HI} = 0.2$ cm^{-3}, $v_{\rm rel} = 25$ km s^{-1}; Redfield 2006), though we note that the gas density is likely reduced by a factor a few inside the astrosphere relative to the nominal value outside (Bzowski et al. 2009). The direction of the flow vector relative to the disk has a significant effect on the resulting disk morphology, and we therefore test a range of flow directions.

To generate scattered-light images of the perturbed disk at some time after the initial encounter with the cloud, we calculate the classical elements from the resulting Runge-Lenz and angular momentum vectors and spread each grain over 100 points in its orbit in proportion to the time spent at each location. We estimate the equilibration timescale by monitoring the system morphology at successive times after the initial encounter with the cloud. Figure 5.17 shows an example of the disk morphology evolution for a highly inclined disk, 10° from edge-on. The relative flow direction in this example is coplanar with the disk midplane. The observed morphology does not change after 3×10^3 years, setting the timescale for which the system is assumed to have achieved steady state.

To create scattered light model images for comparison to HD 61005, we incline the

equilibrated disk by 80° and −80°. We also generate model images inclined by 0° (face-on), 45°, 90° (edge-on), and −45° to illustrate the more general consequences of neutral gas drag. In our notation, positive inclinations indicate that the lower half of the disk in the image is closer to the observer than the upper half. The pixel size in our images is 2.6 AU, corresponding to the projected size of a NICMOS pixel (0.0759″) at the distance of HD 61005 (34.5 pc). The scattered light images also assume a Henyey-Greenstein phase function with a scattering asymmetry typical of debris disks (g = 0.3; Meyer et al. 2007). If the grains in HD 61005 are similar to those in AU Mic, as suggested by the color and polarization results (§3), a larger scattering asymmetry may be more appropriate (e.g., g ∼ 0.7; Graham et al. 2007). However, the adopted scattering asymmetry has a relatively small effect on the qualitative morphology for highly inclined outer disks like HD 61005, as the majority of scattering angles present are near 90°.

The grid of models described above are shown in Figures 5.12, 5.13, and 5.14. The image display scale is logarithmic, and each model is ≈310 AU (= 9″ for HD 61005) to a side. The labels at top indicate the disk inclination, and the labels at left indicate the azimuthal direction of the radial component of the flow vector. The bottom labels indicate the magnitude of the flow vector parallel and perpendicular to the disk midplane. The adopted coordinate system is illustrated with respect to the face-on disks in the left column of each Figure.

When a significant fraction of the relative flow vector is parallel to the disk midplane, Figures 5.12 and 5.13 show that a variety of morphologies can be produced, including bow structures ($i = 0°$), brightness asymmetries ($i = 80°, 90°, -80°$), and warps ($i = 90°/\theta = 0°$). As shown analytically by Scherer (2000) and discussed in §4.2.2, the neutral gas drag force acts to rotate the grain pericenters into a direction perpendicular to the flow vector, resulting in a build up of particles in that direction. This effect is clearly observed in the face-on cases ($i = 0°$) in Figures 5.12 and 5.13.

For a highly inclined disk and a small range of radial flow directions ($\theta \sim 0°, 180°$), the models in Figures 5.12 and 5.13 show a swept morphology somewhat similar to HD 61005. This effect is produced both by the build up of particles perpendicular to the flow vector and the non-zero inclination of the disk. Counterintuitively, the disk models with $v_r = 0$ and $v_z = |v|$ (Figure 5.14) do not show this structure and instead produce a largely symmetric distribution about the disk midplane. As discussed in Scherer (2000), this is because the direction in which a given grain's pericenter rotates to become perpendicular to the flow depends on the initial pericenter direction. As a result, grains with an initial direction to pericenter above the nominal midplane will persist in having a direction to pericenter at or above the midplane as long as they are bound to the star.

Bibliography

Adelman, S. J., Pintado, O. I., Nieva, F., Rayle, K. E., & Sanders, S. E. 2002, A&A, 392, 1031
Alexander, T., & Sternberg, A. 1999, ApJ, 520, 137
Alexander, T. 2005, Phys. Rep., 419, 65
Alibert, Y., Mordasini,C., Benz,W., & Winisdoerffer,C. 2005, A&A, 434, 343–353
Allard, F., Hauschildt, P. H., & Schwenke, D. 2000, ApJ, 540, 1005
Allard, F., Hauschildt, P. H., Alexander, D. R., Tamanai, A., & Schweitzer, A. 2001, ApJ, 556, 357
Alonso, A., Arribas, S., & Martínez-Roger, C. 1999, A&AS, 139, 335
Anderson, J., & King, I. R. 2000, PASP, 112, 1360
Anderson, J. & King, I. 2004, Multi-filter PSFs and Distortion Corrections for the HRC: ACS 2004-15 (Baltimore: Space Telescope Science Institute)
Andre, P., Ward-Thompson, D., & Barsony, M. 2000, Protostars and Planets IV, 59
Aparicio, A., & Gallart, C. 2004, AJ, 128, 1465
Armitage, P. J. 2007, arXiv:astro-ph/0701485
Artymowicz, P., & Clampin, M. 1997, ApJ, 490, 863
Ballero, S. K., Matteucci, F., Origlia, L., & Rich, R. M. 2007, A&A, 467, 123
Baraffe, I., Chabrier, G., Allard, F., & Hauschildt, P. H. 1998, A&A, 337, 403
Basri, G., Mohanty, S., Allard, F., Hauschildt, P. H., Delfosse, X., Martín, E. L., Forveille, T., & Goldman, B. 2000, ApJ, 538, 363
Bean, J. L., Sneden, C., Hauschildt, P. H., Johns-Krull, C. M., & Benedict, G. F. 2006, ApJ, 652, 1604
Beaulieu, J.-P., et al. 2006, Nature, 439, 437
Béjar, V. J. S., et al. 2001, ApJ, 556, 830
Bell, R. A., & Gustafsson, B. 1989, MNRAS, 236, 653
Benedict, G. F., et al. 2001, AJ, 121, 1607
Bessell, M. S., & Brett, J. M. 1988, PASP, 100, 1134
Blackwell, D. E., & Lynas-Gray, A. E. 1994, A&A, 282, 899
Blackwell, D. E., & Lynas-Gray, A. E. 1998, A&AS, 129, 505
Blum, R. D., Sellgren, K., & Depoy, D. L. 1996a, ApJ, 470, 864
Blum, R. D., Sellgren, K., & Depoy, D. L. 1996b, AJ, 112, 1988
Blum, R. D., Ramírez, S. V., Sellgren, K., & Olsen, K. 2003, ApJ, 597, 323

Bond, I. A., et al. 2004, ApJ, 606, L155
Bonfils, X., Delfosse, X., Udry, S., Santos, N. C., Forveille, T., & Ségransan, D. 2005, A&A, 442, 635
Bonfils, X., et al. 2005, A&A, 443, L15
Bonnet, H., et al. 2003, Proc. SPIE, 4839, 329
Boss, A. P. 1997, Science, 276, 1836
Boss, A. P. 2006, ApJ, 644, L79
Brouwer, D., & Clemence, G. M. 1961, New York: Academic Press, 1961
Butler, R.P., Marcy, G.W., Williams, E., McCarthy, C., Dosanjh, P., & Vogt, S.S. 1996, PASP, 108, 500
Butler, R. P., Vogt, S. S., Marcy, G. W., Fischer, D. A., Wright, J. T., Henry, G. W., Laughlin, G., & Lissauer, J. J. 2004, ApJ, 617, 580
Butler, R. P., et al. 2006, ApJ, 646, 505
Buzzoni, A., Chavez, M., Malagnini, M. L., & Morossi, C. 2001, PASP, 113, 1365
Bzowski, M., Möbius, E., Tarnopolski, S., Izmodenov, V., & Gloeckler, G. 2009, Space Science Reviews, 143, 177
Cappellari, M., & Copin, Y. 2003, MNRAS, 342, 345
Carpenter, J. M. 2001, AJ, 121, 2851
Carpenter, J. M., et al. 2005, AJ, 129, 1049
Carpenter, J. M., et al. 2008, ApJS, 179, 423
Carpenter, J. M., et al. 2009, ApJS, 181, 197
Carr, J. S., Sellgren, K., & Balachandran, S. C. 2000, ApJ, 530, 307
Chiang, E., Kite, E., Kalas, P., Graham, J. R., & Clampin, M. 2009, ApJ, 693, 734
Chiang, E., & Youdin, A. N. 2010, Annual Review of Earth and Planetary Sciences, 38, 493
Corder, S., et al. 2009, ApJ, 690, L65
Cox, C., Ritchie, C., Bergeron, E., Mackenty, J., & Noll, K. 1997, NICMOS Distortion Correction—Instrument Science Report OSG-CAL-97-07 (Baltimore: Space Telescope Science Institute)
Cumming, A. 2004 MNRAS, 354, 1165
D'Antona, F. & Mazzitelli, I. 1994, ApJS, 90, 467
D'Antona, F., & Mazzitelli, I. 1997, Memorie della Societa Astronomica Italiana, 68, 807
Davidge, T. J., Simons, D. A., Rigaut, F., Doyon, R., & Crampton, D. 1997, AJ, 114, 2586
Debes, J. H., Weinberger, A. J., & Kuchner, M. J. 2009, ApJ, 702, 318
Delfosse, X., Forveille, T., Perrier, C., & Mayor, M. 1998, A&A, 331, 581
Delfosse, X., Forveille, T., Ségransan, D., Beuzit, J.-L., Udry, S., Perrier, C., & Mayor, M. 2000, A&A, 364, 217
Dent, W. R. F., et al. 2005, MNRAS, 359, 663
Diolaiti, E., Bendinelli, O., Bonaccini, D., Close, L., Currie, D., & Parmeggiani, G. 2000, A&AS, 147, 335
Dohnanyi, J. S. 1969, J. Geophys. Res., 74, 2531
Dolphin, A. 1997, New Astronomy, 2, 397
Dolphin, A. E. 2002, MNRAS, 332, 91

Draine, B. T., & Lee, H. M. 1984, ApJ, 285, 89
Dyck, H. M., Benson, J. A., van Belle, G. T., & Ridgway, S. T. 1996, AJ, 111, 1705
Eikenberry, S., et al. 2006, Proc. SPIE, 6269
Eisenhauer, F., et al. 2003a, The Messenger, 113, 17
Eisenhauer, F., et al. 2003b, Proc. SPIE, 4841, 1548
Eisenhauer, F., Schödel, R., Genzel, R., Ott, T., Tecza, M., Abuter, R., Eckart, A., & Alexander, T. 2003c, ApJ, 597, L121
Elmegreen, B. G., Klessen, R. S., & Wilson, C. D. 2008, ApJ, 681, 365
Endl, M., Cochran, W. D., Kürster, M., Paulson, D. B., Wittenmyer, R. A., MacQueen, P. J., & Tull, R. G. 2006, ApJ, 649, 436
Engelke, C. W. 1992, AJ, 104, 1248
Feast, M. W. 1996, MNRAS, 278, 11
Ferlet, R., Vidal-Madjar, A., & Gry, C. 1985, ApJ, 298, 838
Figer, D. F., McLean, I. S., & Morris, M. 1999, ApJ, 514, 202
Figer, D. F., et al. 2002, ApJ, 581, 258
Figer, D. F., Rich, R. M., Kim, S. S., Morris, M., & Serabyn, E. 2004, ApJ, 601, 319
Fischer, D. A., & Valenti, J. 2005, ApJ, 622, 1102
Fitzgerald, M. P., & Graham, J. R. 2006, ApJ, 637, 541
Fitzgerald, M. P., Kalas, P. G., Duchêne, G., Pinte, C., & Graham, J. R. 2007a, ApJ, 670, 536
Fitzgerald, M. P., et al. 2007b, ApJ, 670, 557
Fluks, M. A., Plez, B., The, P. S., de Winter, D., Westerlund, B. E., & Steenman, H. C. 1994, A&AS, 105, 311
Ford, E. B., Havlickova, M., & Rasio, F. A. 2001, Icarus, 150, 303
Ford, E.B. 2005, AJ, 129, 1706.
Ford, E. B. 2006, ApJ, 642, 505
Freitag, M., Amaro-Seoane, P., & Kalogera, V. 2006, ApJ, 649, 91
Frisch, P. C., Grodnicki, L., & Welty, D. E. 2002, ApJ, 574, 834
Frisch, P. C. 2004, Physics of the Outer Heliosphere, 719, 404
Frogel, J. A., Persson, S. E., Matthews, K., & Aaronson, M. 1978, ApJ, 220, 75
Gallart, C., Zoccali, M., & Aparicio, A. 2005, ARA&A, 43, 387
Gáspár, A., Su, K. Y. L., Rieke, G. H., Balog, Z., Kamp, I., Martínez-Galarza, J. R., & Stapelfeldt, K. 2008, ApJ, 672, 974
Genzel, R., et al. 2003, ApJ, 594, 812
Ghez, A. M., Salim, S., Hornstein, S. D., Tanner, A., Lu, J. R., Morris, M., Becklin, E. E., & Duchêne, G. 2005, ApJ, 620, 744
Gillon, M., et al. 2007, A&A, 472, L13
Gillon, M., et al. 2007, A&A, 471, L51
Girardi, L., Bressan, A., Bertelli, G., & Chiosi, C. 2000, A&AS, 141, 371
Goldreich, P., & Tremaine, S. 1980, ApJ, 241, 425
Goldreich, P., Lithwick, Y., & Sari, R. 2004, ARA&A, 42, 549
Goldreich, P., Lithwick, Y., & Sari, R. 2004, ApJ, 614, 497

Golimowski, D. A., et al. 2006, AJ, 131, 3109
Gould, A., et al. 2006, ApJ, 644, L37
Graham, J. R., Kalas, P. G., & Matthews, B. C. 2007, ApJ, 654, 595
Gray, D. F., & Brown, K. 2001, PASP, 113, 723
Gray, R. O., Napier, M. G., & Winkler, L. I. 2001, AJ, 121, 2148
Gray, R. O., Corbally, C. J., Garrison, R. F., McFadden, M. T., Bubar, E. J., McGahee, C. E., O'Donoghue, A. A., & Knox, E. R. 2006, AJ, 132, 161
Greaves, J. S., et al. 1998, ApJ, 5 06, L133
Gregory, P.C. 2005 ApJ 631, 1198.
Grigorieva, A., et al. 2007, A&A, 461, 573
Guesten, R., Genzel, R., Wright, M. C. H., Jaffe, D. T., Stutzki, J., & Harris, A. I. 1987, ApJ, 318, 124
Gunn, J. E., & Gott, J. R. I. 1972, ApJ, 176, 1
Hales, A., Wootten, A., & Butler, B. 2010, EAS Publications Series, 42, 143
Hartung, M., et al. 2003, Proc. SPIE, 4841, 425
Hauschildt, P. H., Allard, F., & Baron, E. 1999, ApJ, 512, 377
Heiles, C. 1997, ApJ, 481, 193
Heiles, C., & Troland, T. H. 2003, ApJ, 586, 1067
Henry, T. J. & McCarthy, D. W. 1993, AJ, 106, 773
Hines, D. C., et al. 2007, ApJ, 671, L165
Holland, W. S., et al. 1998, Nature, 392, 788
Holmberg, J., Nordstroem, B., & Andersen, J. 2008, VizieR Online Data Catalog, 5128, 0
Hopman, C., & Alexander, T. 2006, ApJ, 645, L133
Hoversten, E. A., & Glazebrook, K. 2008, ApJ, 675, 163
Hubickyj, O., Bodenheimer, P., & Lissauer, J. J. 2004, Revista Mexicana de Astronomia y Astrofisica Conference Series, 22, 83
Ida, S., & Lin, D. N. C. 2005, ApJ, 626, 1045
Jackson, J. M., Geis, N., Genzel, R., Harris, A. I., Madden, S., Poglitsch, A., Stacey, G. J., & Townes, C. H. 1993, ApJ, 402, 173
Jones, H. R. A., Longmore, A. J., Jameson, R. F., & Mountain, C. M. 1994, MNRAS, 267, 413
Jones, H. R. A., Longmore, A. J., Allard, F., & Hauschildt, P. H. 1996, MNRAS, 280, 77
Kalas, P., Graham, J. R., Beckwith, S. V. W., Jewitt, D. C., & Lloyd, J. P. 2002, ApJ, 567, 999
Kalas, P. 2005, ApJ, 635, L169
Kalas, P., Graham, J. R., Clampin, M. C., & Fitzgerald, M. P. 2006, ApJ, 637, L57
Kalas, P., Fitzgerald, M. P., & Graham, J. R. 2007, ApJ, 661, L85
Kalas, P., et al. 2008, Science, 322, 1345
Kent, S. M. 1992, ApJ, 387, 181
Kenyon, S. J., & Bromley, B. C. 2004, AJ, 128, 1916
Kirkpatrick, J. D., Kelly, D. M., Rieke, G. H., Liebert, J., Allard, F., & Wehrse, R. 1993, ApJ, 402, 643

Kleinmann, S. G., & Hall, D. N. B. 1986, ApJS, 62, 501
Koerner, D. W., et al. 2001, ApJ, 560, L181
Köhler, M., & Mann, I. 2004, Journal of Quantitative Spectroscopy & Radiative Transfer, 89, 453
Kormendy, J., & Kennicutt, R. C., Jr. 2004, ARA&A, 42, 603
Kozhurina-Platais, V. & Biretta, J. 2004, ACS/HRC Polarimetry Calibration III: Astrometry of the Polarized Filters: ACS 2004-11 (Baltimore: Space Telescope Science Institute)
Krabbe, A., Genzel, R., Drapatz, S., & Rotaciuc, V. 1991, ApJ, 382, L19
Krabbe, A., et al. 1995, ApJ, 447, L95
Krist, J. E., et al. 2005, AJ, 129, 1008
Krivov, A. V., Löhne, T., & Sremčević, M. 2006, A&A, 455, 509
Krivov, A. V. et al. 2007, A&A, 462, 199
Kroupa, P. 2002, Science, 295, 82
Kruegel, E. 2003, The physics of interstellar dust, by Endrik Kruegel. IoP Series in astronomy and astrophysics, ISBN 0750308613. Bristol, UK: The Institute of Physics, 2003
Lada, C. J. 1999, NATO ASIC Proc. 540: The Origin of Stars and Planetary Systems, 143
Lada, C. J., Muench, A. A., Rathborne, J., Alves, J. F., & Lombardi, M. 2008, ApJ, 672, 410
Laughlin, G., Bodenheimer, P., & Adams, F. C. 2004, ApJ, 612, L73
Launhardt, R., Zylka, R., & Mezger, P. G. 2002, A&A, 384, 112
Leggett, S. K. 1992, ApJS, 82, 351
Leggett, S. K., Allard, F., Berriman, G., Dahn, C. C., & Hauschildt, P. H. 1996, ApJS, 104, 117
Leggett, S. K., Allard, F., Dahn, C., Hauschildt, P. H., Kerr, T. H., & Rayner, J. 2000, ApJ, 535, 965
Leggett, S. K., Allard, F., Geballe, T. R., Hauschildt, P. H., & Schweitzer, A. 2001, ApJ, 548, 908
Leggett, S. K., Hauschildt, P. H., Allard, F., Geballe, T. R., & Baron, E. 2002, MNRAS, 332, 78
Levesque, E. M., Massey, P., Olsen, K. A. G., Plez, B., Josselin, E., Maeder, A., & Meynet, G. 2005, ApJ, 628, 973
Levison, H. F., Morbidelli, A., Gomes, R., & Backman, D. 2007, Protostars and Planets V, 669
Li, A., & Greenberg, J. M. 1998, A&A, 331, 291
Lin, D. N. C., & Ida, S. 1997, ApJ, 477, 781
Linde, T. J., & Gombosi, T. I. 2000, J. Geophys. Res., 105, 10411
Lindqvist, M., Habing, H. J., & Winnberg, A. 1992, A&A, 259, 118
Malagnini, M. L., & Morossi, C. 1990, A&AS, 85, 1015
Malagnini, M. L., & Morossi, C. 1997, A&A, 326, 736
Malhotra, R. 1995, AJ, 110, 420
Mann, I., Köhler, M., Kimura, H., Cechowski, A., & Minato, T. 2006, A&A Rev., 13, 159
Marcy, G., Butler, R. P., Fischer, D., Vogt, S., Wright, J. T., Tinney, C. G., & Jones,

H. R. A. 2005, Progress of Theoretical Physics Supplement, 158, 24
Marois, C., Macintosh, B., Barman, T., Zuckerman, B., Song, I., Patience, J., Lafrenière, D., & Doyon, R. 2008, Science, 322, 1348
Martins, F., Genzel, R., Hillier, D. J., Eisenhauer, F., Paumard, T., Gillessen, S., Ott, T., & Trippe, S. 2007, A&A, 468, 233
Masana, E., Jordi, C., & Ribas, I. 2006, A&A, 450, 735
McCaughrean, M. J., Close, L. M., Scholz, R.-D., Lenzen, R., Biller, B., Brandner, W., Hartung, M., & Lodieu, N. 2004, A&A, 413, 1029
McKee, C. F., & Ostriker, J. P. 1977, ApJ, 218, 148
McKee, C. F., & Ostriker, E. C. 2007, ARA&A, 45, 565
Meurer, G. R., et al. 2009, ApJ, 695, 765
Meyer, D. M., Lauroesch, J. T., Heiles, C., Peek, J. E. G., & Engelhorn, K. 2006, ApJ, 650, L67
Meyer, D. M. 2007, SINS - Small Ionized and Neutral Structures in the Diffuse Interstellar Medium, 365, 97
Meyer, M. R., Backman, D. E., Weinberger, A. J., & Wyatt, M. C. 2007, Protostars and Planets V, 573
Minato, T., Köhler, M., Kimura, H., Mann, I., & Yamamoto, T. 2006, A&A, 452, 701
Moerchen, M. M., et al. 2007, ApJ, 666, L109
Moór, A., et al. 2006, ApJ, 644, 525
Morris, M., & Serabyn, E. 1996, ARA&A, 34, 645
Moro-Martin, A., et al. 2008, in The Solar System Beyond Neptune, ed. A. Barucci (Tucson, AZ: Univ. Arizona Press), 465
Mouillet, D., Larwood, J. D., Papaloizou, J. C. B., & Lagrange, A. M. 1997, MNRAS, 292, 896
Müller, H.-R., Frisch, P. C., Florinski, V., & Zank, G. P. 2006, ApJ, 647, 1491
Narayanan, V. K., Gould, A., & Depoy, D. L. 1996, ApJ, 472, 183
Nayakshin, S., & Sunyaev, R. 2005, MNRAS, 364, L23
Nordström, B., et al. 2004, A&A, 418, 989
Oliveira, J. M. 2008, Handbook of Star Forming Regions, Volume II, 599
Paumard, T., et al. 2006, ApJ, 643, 1011
Paust, N. E. Q., et al. 2009, AJ, 137, 246
Pavlovsky, C. 2006, ACS Data Handbook, Version 5.0 (Baltimore: Space Telescope Science Institute)
Perrin, G., Coude Du Foresto, V., Ridgway, S. T., Mariotti, J.-M., Traub, W. A., Carleton, N. P., & Lacasse, M. G. 1998, A&A, 331, 619
Perryman, M. A. C., et al. 1997, A&A, 323, L49
Persson, S. E., Murphy, D. C., Krzeminski, W., Roth, M., & Rieke, M. J. 1998, AJ, 116, 2475
Philipp, S., Zylka, R., Mezger, P. G., Duschl, W. J., Herbst, T., & Tuffs, R. J. 1999, A&A, 348, 768
Pollack, J. B., Hubickyj, O., Bodenheimer, P., Lissauer, J. J., Podolak, M., & Greenzweig,

Y. 1996, Icarus, 124, 62
Press, W. H., Teukolsky, S. A., Vetterling, W. T., & Flannery, B. P. 1992, Cambridge: University Press, —c1992, 2nd ed.
Ramirez, S. V., Depoy, D. L., Frogel, J. A., Sellgren, K., & Blum, R. D. 1997, AJ, 113, 1411
Ramírez, S. V., Sellgren, K., Carr, J. S., Balachandran, S. C., Blum, R., Terndrup, D. M., & Steed, A. 2000, ApJ, 537, 205
Ramírez, I., & Meléndez, J. 2005, ApJ, 626, 446
Raymond, S. N., Quinn, T., & Lunine, J. I. 2005, ApJ, 632, 670
Reche, R., et al. 2008, A&A, 480, 551
Redfield, S. 2006, New Horizons in Astronomy: Frank N. Bash Symposium, 352, 79
Redfield, S. 2007, ApJ, 656, L97
Redfield, S., & Linsky, J. L. 2008, ApJ, 673, 283
Reid, M. J. 1993, ARA&A, 31, 345
Reid, N. & Hawley, S. L. 2000, New light on dark stars : red dwarfs, low mass stars, brown dwarfs / Neill Reid and Suzanne L. Hawley. New York : Springer, 2000. (Springer-Praxis series in astronomy and astrophysics)
Rieke, M. J. 1987, Nearly Normal Galaxies. From the Planck Time to the Present, 90
Rieke, M. J. 1999, ASP Conf. Ser. 186: The Central Parsecs of the Galaxy, 186, 32
Rivera, E. J., et al. 2005, ApJ, 634, 625
Roccatagliata, V., Henning, T., Wolf, S., Rodmann, J., Corder, S., Carpenter, J. M., Meyer, M. R., & Dowell, D. 2009, A&A, 497, 409
Rousset, G., et al. 2003, Proc. SPIE, 4839, 140
Sadler, E. M., Rich, R. M., & Terndrup, D. M. 1996, AJ, 112, 171
Scherer, K. 2000, J. Geophys. Res., 105, 10329
Schneider, G., et al. 2005, ApJ, 629, L117
Schneider, G., et al. 2006, ApJ, 650, 414
Schödel, R., et al. 2007, A&A, 469, 125
Schreiber, J., Thatte, N., Eisenhauer, F., Tecza, M., Abuter, R., & Horrobin, M. 2004, ASP Conf. Ser. 314: Astronomical Data Analysis Software and Systems (ADASS) XIII, 314, 380
Scott, S. E., et al. 2002, MNRAS, 331, 817
Sellgren, K., Hall, D. N. B., Kleinmann, S. G., & Scoville, N. Z. 1987, ApJ, 317, 881
Serabyn, E., Keene, J., Lis, D. C., & Phillips, T. G. 1994, ApJ, 424, L95
Sheehy, C. D., McCrady, N., & Graham, J. R. 2006, ApJ, 647, 1517
Shu, F. H., Adams, F. C., & Lizano, S. 1987, ARA&A, 25, 23
Siess, L., Dufour, E., & Forestini, M. 2000, A&A, 358, 593
Sjouwerman, L. O., Habing, H. J., Lindqvist, M., van Langevelde, H. J., & Winnberg, A. 1999, ASP Conf. Ser. 186: The Central Parsecs of the Galaxy, 186, 379
Smalley, B. 1993, MNRAS, 265, 1035
Sokolov, N. A. 1998, A&AS, 130, 215
Stanimirović, S., & Heiles, C. 2005, ApJ, 631, 371
Steer, D. G., et al. 1984, A&A, 137, 159

Stolte, A., Brandner, W., Grebel, E. K., Lenzen, R., & Lagrange, A.-M. 2005, ApJ, 628, L113
Strubbe, L. E., & Chiang, E. I. 2006, ApJ, 648, 652
Taylor, B. J. 2003, A&A, 398, 721
Theodossiou, E., & Danezis, E. 1991, Ap&SS, 183, 91
Thommes, E. W., Duncan, M. J., & Levison, H. F. 2002, AJ, 123, 2862
Udalski, A., et al. 2005, ApJ, 628, L109
Vacca, W. D., Sheehy, C. D., & Graham, J. R. 2007, ApJ, 662, 272
Valenti, J. A., Piskunov, N., & Johns-Krull, C. M. 1998, ApJ, 498, 851
van Dam, M. A., Le Mignant, D., & Maccintosh, B. A. 2004, Appl Opt., 43, 5458
van Gorkom, J. H. 2004, Clusters of Galaxies: Probes of Cosmological Structure and Galaxy Evolution, 305
van Loon, J. T., et al. 2003, MNRAS, 338, 857
Veeder, G. J. 1974, AJ, 79, 1056
Vogt, S. S. et al. 1994. Proc. Soc. Photo-Opt. Instr. Eng., 2198, 362
Wadhwa, M., Amelin, Y., Davis, A. M., Lugmair, G. W., Meyer, B., Gounelle, M., & Desch, S. J. 2007, Protostars and Planets V, 835
Wakker, B. P., & Mathis, J. S. 2000, ApJ, 544, L107
Wallace, L., & Hinkle, K. 1997, ApJS, 111, 445
Warren, S. G. 1984, Appl. Opt., 23, 1206
Weidenschilling, S. J. 1977, MNRAS, 180, 57
Welsh, B. Y., Craig, N., Vedder, P. W., & Vallerga, J. V. 1994, ApJ, 437, 638
Wichmann, R., Schmitt, J. H. M. M., & Hubrig, S. 2003, A&A, 399, 983
Wilkins, S. M., Hopkins, A. M., Trentham, N., & Tojeiro, R. 2008, MNRAS, 391, 363
Wilner, D. J., et al. 2002, ApJ, 569, L115
Wood, B. E. 2004, Living Reviews in Solar Physics, 1, 2
Wood, B. E., Müller, H.-R., Zank, G. P., Linsky, J. L., & Redfield, S. 2005, ApJ, 628, L143
Wood, P. R., Habing, H. J., & McGregor, P. J. 1998, A&A, 336, 925
Wyatt, M. C. 2006, ApJ, 639, 1153
Wyatt, M. C. 2008, ARA&A, 46, 339
Zoccali, M., Cassisi, S., Frogel, J. A., Gould, A., Ortolani, S., Renzini, A., Rich, R. M., & Stephens, A. W. 2000, ApJ, 530, 418
Zoccali, M., et al. 2003, A&A, 399, 931
Zoccali, M., et al. 2006, A&A, 457, L1